MATERIAL PROPERTIES OF UREOLYTICALLY INDUCED CALCIUM CARBONATE ADHESIVES

by

Sobia Anjum

A dissertation submitted in partial fulfillment
of the requirements for the degree

of

Doctor of Philosophy

in

Engineering

MONTANA STATE UNIVERSITY
Bozeman, Montana

December 2023

DEDICATION

To my husband, who supported me through the ebbs and flows of this journey.

ACKNOWLEDGEMENTS

I am grateful for the divine fate that brought me to the Center for Biofilm Engineering at Montana State University. I am grateful for the community, and the opportunities for personal and professional growth in this place.

I finish this thesis with the support of many people, among whom the foremost is my committee. I thank my committee chair, Dr. Robin Gerlach, for guiding me through my PhD studies, supporting me in research, and bringing together a group of committee members who supported all pieces of research projects wholeheartedly. I thank the committee members Dr. Adie Phillips, Dr. Chelsea Heveran, and Dr. Jim Wilking for actively contributing to my learning and growth in research experiences.

I thank Dr. Cecily Ryan and Dr. Stephen Sofie for sharing their insights and lab resources for my research projects. I am incredibly grateful to my peers, without whose support this research and dissertation would not have been possible: Kendall Parks, Kaylin Clark, Abby Thane, Jesse Arroyo, Ethan Viles, Kylee Rux, Sara Zacher, Ghazal Vahidi, Amir Darabi, and Brady Bishop. Thank you, Sara Huth, Miriam Daniels, Donna Negaard, Emily Peters, Lauren Cerretti, and Deborah Chiolero, for being the administrative saviors.

I am grateful to my friends Kate and Steve for their tremendous and consistent support through all academic and personal challenges. Finally, I thank my sisters Samia and Tayyiba, and sisters at heart Aleema and Sidra, for believing in me before I believed in myself.

TABLE OF CONTENTS

TABLE OF CONTENTS CONTINUED

TABLE OF CONTENTS CONTINUED

TABLE OF CONTENTS CONTINUED

LIST OF TABLES

Table Page

LIST OF TABLES CONTINUED

Table Page

LIST OF TABLES CONTINUED

Table Page

LIST OF FIGURES

Figure Page

LIST OF FIGURES CONTINUED

Figure Page

LIST OF FIGURES CONTINUED

Figure Page

LIST OF FIGURES CONTINUED

Figure Page

LIST OF FIGURES CONTINUED

Figure Page

LIST OF FIGURES CONTINUED

Figure Page

LIST OF FIGURES CONTINUED

Figure Page

LIST OF FIGURES CONTINUED

Figure Page

LIST OF FIGURES CONTINUED

Figure Page

LIST OF FIGURES CONTINUED

Figure Page

LIST OF FIGURES CONTINUED

Figure Page

ABSTRACT

Polymers used in adhesive applications are often petrochemical-based and release volatile organic compounds (VOCs) during application. These VOCs can accumulate indoors to the detriment of human health. Biopolymers potentially offer a non-toxic and sustainable alternative to synthetic polymers but generally have limited physical stability and low mechanical performance. One of the methods of improving the stability and adhesive performance of biopolymers is the addition of a mineral phase to reinforce biopolymer adhesives.

In this work, biomineral-reinforced biopolymer adhesives were produced by ureolytically induced precipitation of calcium carbonate in the presence of guar gum and soy protein. The microbially and enzymatically induced ureolysis was carried out by the ureolytic bacterium, *Sporosarcina pasteurii*, or by jack bean urease. The resulting adhesives were referred to as ureolytically induced calcium carbonate precipitation (UICP)-reinforced adhesives and specifically microbially and enzymatically induced calcium carbonate (MICP and EICP)-reinforced adhesives.

The adhesive strength of these composite adhesives was optimized by varying calcium and cell (or enzyme) concentrations. The adhesive strength of biomineral reinforced guar gum and soy protein biopolymers was up to 2.5 and 6 times higher than the adhesive strength of the biopolymers alone, respectively. The durability of the MICP-reinforced adhesives was tested after varying immersions (24 h and 7 days), relative humidities (50 and 80% RH), and temperatures (-20, 100, and 300˚C). The durability of the MICP-reinforced adhesives, upon immersion, was significantly improved compared to biopolymer alone, and maintained their adhesive strength at moderate humidities and from below-freezing to room temperatures after 7-day exposures.

To determine the effect of biopolymers on the nanoscale material properties of biomineral aggregates, enzymatically induced calcium carbonate precipitation was induced in the presence of a standard protein, Bovine Serum Albumin (BSA). Nanoindentation and Atomic Force Microscopy show that the moduli of the mineral precipitates were significantly lowered in the presence of BSA. Atomic force microscopy also showed that BSA introduced structural variations and moduli gradation in biominerals.

These results demonstrate that the presence of a protein additive, specifically BSA, can alter the nanoscale structure and material properties of calcium carbonate precipitates. Using an organic additive to manipulate microscale material properties of biominerals offers possibilities for advanced control at the microscale and enhanced toughness at the macroscale for engineering applications such as in construction, binder, and adhesive applications.

CHAPTER ONE

INTRODUCTION

The success of modern industrial developments, specifically automobile, aerospace, electronics, and wood industries, depends on high-performance adhesives (Höfer et al., 2001; Packham, 2009). Most synthetic adhesives in the market use petrochemical and synthetic solvents with moderate to high volatile organic compounds (VOC) emissions (Frey et al., 2014; Hazrati et al., 2016; Tolls et al., 2016; Wolkoff, 1998; Zhu et al., 2013). Using petrochemical feedstock raises sustainability concerns, and an accumulation of VOCs indoors has detrimental human health impacts (Du et al., 2014; Li et al., 2021; Wickliffe et al., 2020). Rising consumer awareness, stringent regulations, petrochemical feedstock instability, and sustainability concerns have led to an acceleration in the search for safer and sustainable adhesives, *e.g.*, natural adhesives (Höfer et al., 2019; Packham, 2009). Natural adhesives consist of biobased monomers and polymers derived from plant, animal, fungal, and microbial sources (Heinrich, 2019). These biobased adhesives have the advantages of diverse functionalities, structure, and renewability (Dinte & Sylvester, 2018; Frihart, 2015). However, natural adhesives currently available have low bonding strength and high sensitivity to moisture (Dinte & Sylvester, 2018; Lamaming et al., 2021; Lutz et al., 2022; Patel et al., 2013).

Mechanical reinforcement of biopolymers by adding mineral phases has shown the potential to improve the adhesive strength and lower water sensitivity of some biopolymer adhesives, e.g., soy protein adhesives (Guangyan, 2016; Piekarska et al., 2017; Post et al., 2021; Sun et al., 2021). However, adding minerals and clays directly often results in poor dispersion and low interfacial strength (Azeredo & Waldron, 2016; Raydan et al., 2021). Crosslinking and

copolymerization have been used to improve the interfacial strength of polymer-mineral composites, but this approach introduces additional processing steps, use of organic solvents, and potentially hazardous crosslinkers (Helanto et al., 2021, 2022; Post et al., 2021). Recent research has focused on reducing the use of petroleum-based, toxic or hazardous crosslinkers and their replacement with bioinspired and biomimetic processes for the production of biopolymer-mineral composites (Cao et al., 2021; Cui et al., 2023; Höfer et al., 2019; Kang et al., 2016; Li et al., 2018; Pang et al., 2021). The proposed study explores one such biopolymer mineral adhesive, a composite formed by ureolytically induced calcium carbonate precipitation in the presence of guar gum and soy protein biopolymers.

The reaction carried out by the enzyme urease can be summarized as follows:

$$H_2N - CO - NH_2(urea) + 2H_2O + Ca^{2+} \rightarrow 2NH_4^+ + CaCO_3(s)$$

The ureolysis is carried out by the enzyme urease, which means that the biocomposite can be formed by a urease enzyme suspension (EICP) as well as by microbial cells containing ureases (MICP) (Phillips et al., 2013). In this study, both methods are employed, and collectively referred to as ureolytically induced calcium carbonate precipitation (UICP). UICP has previously been used for surface and subsurface applications to bind soil particles, seal fractures, remediate concrete surfaces, and remove heavy metals and radionuclides from wastewaters (Phillips et al., 2013; Zhu & Dittrich, 2016). However, the use of UICP to develop UICP-reinforced biopolymer for adhesive applications is unique in this work. The overarching hypothesis of this work was that using UICP can improve the physical and mechanical stability of biopolymers. Moreover, beacuse the UICP can be carried out at ambient temperatures, without organic solvents or crosslinkers, they have a high sustainability potential as compared to most current methods for making biopolymer-mineral composite adhesives.

The principal objective of this study was to determine the applicability of ureolytically induced calcium carbonate composites as natural adhesives. The key factors used to determine the suitability of the biomineral- reinforced biopolymers as adhesives were their adhesive strength, durability against environmental factors, and potential control parameters to manipulate the material properties of the composites.

Specific aim 1. Optimize the Adhesive Strength of Ureolytically Induced Calcium Carbonate Precipitation Reinforced Adhesives

The experimental design and outcomes of *specific aim 1* are presented in detail in *Chapter 3* of this dissertation. To determine the applicability of the UICP reinforced biopolymers as adhesives, it is important to determine the optimal formulation chemistry for adhesive applications. The *hypothesis of specific aim 1* was that the ureolytically induced calcium carbonate precipitation (UICP) can enhance the adhesive shear strength of biopolymers. The MICP- and EICP-reinforced adhesives were prepared using *S. pasteurii* and jack bean meal (JBM) to induce ureolysis in guar gum and soy protein. Guar gum and soy protein were used as representative polysaccharide and protein biopolymers. The calcium concentration was varied, to optimize the amount of calcium carbonate precipitation. The cell and enzyme concentrations were varied to optimize the ureolysis rates. The adhesive strength of the resulting composites was determined by adhesive shear strength testing. The *key outcomes of specific aim 1* were i) the adhesive strength of the MICP- and EICP-reinforced adhesives was significantly higher than the biopolymers alone ii) the adhesive strength of the composites was strongly influenced by the type of biopolymer and iii) at an optimal calcium concentration, the adhesive strength was similar to commercial water-based adhesives.

Specific aim 2. Determine the Durability of UICP-Reinforced Adhesives Against Varying Temperature and Humidity Exposures

The experimental design and outcomes of *specific aim 2* are presented in detail in *Chapter 4*. The development of biopolymer-mineral composites is a relatively new area of research. While the adhesive strength of several biopolymer mineral composites has been demonstrated (Chow et al., 2004; Helanto et al., 2021; Segura González et al., 2015) there is limited research available on the durability of these composites. Available research shows that the increase in adhesive strength and improvements in durability of the composites can be mutually exclusive (Chen et al., 2018; Kim et al., 2021; Li et al., 2018). The *hypothesis for the specific aim 2* was that the UICP-reinforced adhesives have higher durability than biopolymers. To test the water resistance of the composites, the adhesive strength of the MICP and EICP-reinforced adhesives and biopolymers was tested before and after immersion in DI water for 24 hours. The MICP-reinforced adhesives were also tested after 7-day exposures to immersion in DI water, varying temperatures and humidities. The *key outcomes of specific aim 2* were i) the water resistance of the MICP-reinforced adhesives was found to be significantly higher than for the biopolymer alone. The MICP-reinforced adhesives retained 75 to 81% of their adhesive strength after immersion, whereas the adhesively bonded joints made with biopolymers deteriorated during immersion before testing ii) The MICP-reinforced adhesives retained their adhesive strengths from below freezing to room temperatures, and at 50% RH after 7 days of exposures and iii) at higher humidities (80% RH) and temperatures ($\geq 100^{\circ}C$) the adhesive strength was potentially limited by the mineral and organic content of the adhesives.

Specific Aim 3. Determine the Influence of a Protein Additive on the Nanoscale Material Properties of Ureolytically Induced Calcium Carbonate Precipitates

The experimental design and outcomes of *specific aim 3* are presented in detail in *Chapter 5*. Most of the research in the development of UICP for engineered applications has effectively leveraged the potential control of the calcium carbonate precipitation by supersaturation (as demonstrated in *specific aim 1*). However, the use of organics to mediate the calcium carbonate precipitation and crystallization kinetics in UICP has been relatively limited. To further the improvements in the development and prospective use of UICPs for engineered applications, it is essential to determine the influence of organics not only on the morphology and polymorphism but also on the material properties of the mineral precipitates. The *hypothesis for specific aim 3* was that presence of organics can modify the nanoscale hardness and stiffness of biomineral precipitates. For this purpose, the UICP was carried out in the presence of a standard protein Bovine Serum Albumin (BSA). To determine the effect of protein on the nanomechanical properties of the mineral precipitates, enzymatically induced calcium carbonate precipitates were prepared in the presence of BSA (EICP-BSA) and compared to enzymatically induced precipitates in the absence of BSA. The *key outcomes of specific aim 3* were i) that the elastic moduli and hardness, measured by nanoindentation, of the mineral precipitates produced in the presence of BSA were significantly lower than of those produced in the absence of BSA ii) XRD analysis showed that both EICP and EICP-BSA precipitates consisted of calcite, which suggests that the difference in elastic moduli may be due to the presence of organics as opposed to differences in polymorphs and iii) atomic force microscopy (AFM) of the precipitates showed that the distinguishing feature of the EICP-BSA was their nanoscale heterogeneity within the

mineral precipitates. These results show that the protein can be used to modify the nanoscale structure and material properties of the UICP-reinforced adhesives.

The key findings of this work are (1) UICP can be used successfully to reinforce biopolymer natural adhesives to deliver commercially relevant adhesive strength (2) UICP reinforced adhesives can potentially be used for indoor applications due to their durability at ambient temperatures and humidities (3) nanoscale material properties of the ureolytically induced biominerals can be manipulated by the protein additive BSA. Collectively, these results show that there is a tremendous opportunity for the advancement of UICP-reinforced adhesives by optimizing both supersaturation and the matrix-mediated interactions using organic additives for adhesive and other engineered applications.

This research was made possible by the Department of Chemical and Biological Engineering and the Center for Biofilm Engineering at the Norm Asbjornson College of Engineering at Montana State University, a Ray and Erin Schultz Emerging Scholars Fellowship, and the United States Education Foundation Pakistan Fulbright Commission. Sobia Anjum was supported by the Thermal Biology Institute through funding from the MSU Office of the Vice President for Research and Economic Development for PhD graduate enhancement. This work was also partially supported by the National Science Foundation (CMMI 20368687 to CH and RG).

CHAPTER TWO

2.0 BACKGROUND

2.1 Biopolymer-Mineral Composites as Adhesives

Polymers produced in nature, also called biopolymers, have received particular attention in modern adhesives development owing to their renewable, non-toxic, and eco-friendly with remarkable diversity in their chemistry, thermomechanical properties, rheology, and chemical reactivity (Baranwal et al., 2022; Reddy et al., 2021). Their capacity to undergo various chemical modifications yields materials with tailored properties suitable for use as adhesives, gums, coatings, emulsions, and binders (Imam et al., 2013). One common modification to biopolymers to improve their performance and stability is the formation of biopolymer-mineral composites (Helanto et al., 2021; Xiong et al., 2018). Biopolymer composites contain a stiff component which may be particle- (mineral or metal) or fiber-based (natural or synthetic), acting as reinforcement within a polymer matrix (Sierra-Romero & Chen, 2018). The addition of fillers to a biopolymer matrix can not only improve its overall properties but, in some cases, provide added-value functionalities such as electrical conductivity (Thorvaldsen et al., 2015; Wang et al., 2011).

Two broad categories of biopolymer mineral composites are used for adhesive applications, including fiber-reinforced and particle-reinforced composites (Xiong et al., 2018). Fiber-reinforced composites are formed by combining biopolymers with fillers with long aspect ratios (e.g., carbon nanotubes, graphene, or natural fibers such as cellulose nanofiber). The

particle-reinforced biopolymers composites contain stiff particulate nanofiller with small aspect ratios.

Particle-based polymer and biopolymer adhesives commonly contain geomineral, metal or metal oxide nanoparticles, and biopolymeric nanoparticle fillers. The geominerals are geologically sourced and include mica, clay, kaolin, etc. (Leong et al., 2004), metal- and metal oxide-based nanoparticles include metals like Ag and Au or a metal oxide, e.g., Fe_3O_4 (Post et al., 2021; Segura González et al., 2015), and biopolymeric nanoparticles include protein, polysaccharide, and polypeptide-based particles (Vodyashkin et al., 2022). Biopolymer-geomineral composites are made by i) grafting a polymer onto a mineral by crosslinkers ii) polymerizing monomers in the presence of geominerals (Imam et al., 2013). Biopolymer-metal nanoparticles composites are also made by either i) electrostatic or covalent bonding of nanoparticle to a polymer or ii) precipitation of nanoparticles during the polymerization of hydrogels (Bovone et al., 2021; Kim et al., 2021; Li et al., 2018). Biopolymer-biopolymeric nanoparticle composites are made by the precipitation of a polymer (protein or polysaccharide) into another biopolymer to enhance the stiffness of the resultant composite. The natural diversity of polymeric systems inspires a broad range of functionalities being explored for biopolymer composites, and extensive reviews of emerging biopolymer composites with organic and inorganic modifications are available here (Amenorfe et al., 2022; Díez-Pascual, 2022; Sadasivuni et al., 2020). While abundant, the research in biopolymer mineral composites is new and requires extensive testing of composite properties and their performance in specific applications, e.g., as adhesives.

2.1.1 Biopolymer Mineral Composites: Challenges and Opportunities

While geominerals composites are some of the leading types of polymer mineral composites under research, there are many challenges associated with their development. These challenges include poor dispersion, low loading rates, and the poor compatibility of minerals with biopolymers (Chen et al., 2022). The geominerals also require pre-processing, such as shearing, to achieve small mineral size, exfoliation, and functionalization to improve their compatibility with the biopolymers (Guchait et al., 2022). Despite these pre-processing steps, minerals need to be attached to the biopolymers by crosslinkers to achieve high physical stability and mechanical performance as biopolymer-mineral composites (Bukartyk et al., 2022; Höfer et al., 2019). These steps add to the processing cost and complexity and, more importantly, introduce hazardous and toxic crosslinking reagents (Guchait et al., 2022; Oliveira et al., 2018; Steven Abbott, 2019). To improve the sustainability of the particle reinforced biobased adhesives, further research is aimed at the use of bioinspired crosslinking mechanisms (Ghahri et al., 2021). While the biomineralization process has inspired geomineral-based nanocomposites, and crosslinking strategies are being explored to improve their performance and sustainability of the composites, the inherent value of biomineralization and (bio)mineral-biopolymer interactions has not been genuinely harnessed in these synthesis methods.

2.2 Biomineralization for Bioinspired Biopolymer-Mineral Composites

Biomineralization refers to the processes by which organisms form minerals. Biomineralization in nature is characterized by the control exerted by organisms or by the influence of organics on biomineral formation (Weiner & Dove, 2003). Organic compound-mineral interactions affect biomineralization from the nucleation precursor to growth,

maturation, and even after the mineral aggregate has been formed and stabilized (Deng et al., 2022; Falini & Fermani, 2013; Weiner & Dove, 2003). Biomineralization is a feature of all phyla in living systems, making it difficult to categorize the structural features of biominerals and their mechanisms of formation collectively (Weiner & Dove, 2003). A common feature of biomineralization is the occurrence of organic mineral interactions during biomineralization. These interactions can result in hierarchical structures and synergistic material properties (e.g., material toughness) of biomaterials that can be several orders of magnitude higher than achievable by the single component materials (Deng et al., 2022; Labonte et al., 2017; Peng et al., 2022). The astounding diversity of composition, morphologies, properties, and functions in natural biomineralized materials such as bone, enamel, dentine, nacre, and sea urchins has inspired many biomaterials for tissue engineering and regenerative medicine over the recent years (Deng et al., 2022; Nudelman & Sommerdijk, 2012). On the other hand, biomineralization carried out by microbial activities in geochemical systems has inspired structural applications of the biominerals as sealants and binders for surface and subsurface geotechnical engineering applications (Phillips et al., 2013; T. Zhu & Dittrich, 2016). Other biomimetic synthesis pathways relevant from the adhesives' perspective are mussel and gecko adhesion biochemistries (Higham et al., 2019) as well as adhesion and biomineralization mechanisms in oysters (Metzler et al., 2016).

In this review, the biogeochemical pathways of biomineralization are discussed, and classical nucleation theory is used to explain the kinetic control parameters for precipitation in the presence of organics (Benning & Waychunas, 2008; De Yoreo, 2003; Evans, 2017). For adhesives applications, the relevant material properties of the polymer-mineral composites include particle size, stiffness, and interfacial adhesion (Piekarska et al., 2017; Post et al., 2021).

Therefore, the structure-function relationships of biomineralized materials are discussed here in terms of their stiffness, interfacial adhesion, and failure mechanisms. In the last section of the chapter, the discussion is focused on biomineralization for adhesive, binder, and sealant applications.

2.2.1 Biomineralization Induced by Microbial Activities

Bacterial biomineralization is widely prevalent in the natural environment, and more than 60 minerals have been identified so far (Görgen et al., 2021). Calcium carbonate is one of the most common minerals in natural environments and is produced by all phyla of living organisms either by highly controlled processes (Deng et al., 2022; Harris et al., 2017) or induced in their environments by microbial activity and its products (Zhu & Dittrich, 2016). Different calcium carbonate mineral phases formed by bacteria include calcite, aragonite, vaterite, amorphous calcium carbonates, and hydrated calcium carbonate such as monohydrocalcite (Yu & Jiang, 2018; Zhu & Dittrich, 2016).

Calcium carbonate precipitation by bacteria in nature is often induced by (1) the increase of the saturation index of the solution surrounding cells with this mineral phase and (2) the decrease of the nucleation energy barrier for precipitation by producing extracellular products that facilitate calcium carbonate precipitation (Decho, 2010).

In the most commonly used engineering applications, calcium carbonate precipitation is induced through ureolysis, which increases the pH and carbonate ion concentrations and, thus, the saturation index of calcium carbonate. *Sporosarcina pasteurii*, a common soil bacterium, has one of the highest rates of ureolysis and is, therefore, extensively used for surface and subsurface applications to bind soil particles, reduce subsurface permeability of water or gaseous phases,

and seal surface and subsurface fractures (Krajewska, 2018; Phillips et al., 2013). *Sporosarcina pasteurii* catalyzes ureolysis, the hydrolysis of urea, to produce ammonia and carbonic acid (Eq. 2.1). In an aqueous solution, ammonia functions as a Brønsted–Lowry base to yield ammonium and hydroxide ions (Eq. 2.2). As a result, the produced carbonic acid is converted into bicarbonate and carbonate (Eq. 2.3). In the presence of multi-valent cations, such as calcium ions, (calcium) carbonate precipitation can occur (Eq. 2.4).

Equation 2.1 $CO(NH_2)_2 + 2H_2O \rightarrow 2NH_3 + H_2CO_3$

Equation 2.2 $2NH_3 + 2H_2O \rightarrow 2NH_4^+ + 2OH^-$; (Rise in pH)

Equation 2.3 $H_2CO_3 + 2\ OH^- \leftrightarrow HCO_3^- + H_2O + OH^- \leftrightarrow CO_3^{2-} + 2H_2O$ (Equilibrium shifts towards carbonate)

Equation 2.4 $Ca^{2+} + CO_3^{2-} \rightarrow CaCO_3$

Thermodynamically, once the solubility product (Eq. 2.5) has been exceeded, the solution is considered supersaturated with respect to the reactants, and calcium carbonate can precipitate. Engineered applications of UICP have traditionally involved optimizing urea and calcium concentrations to control the extent of supersaturation (Krajewska, 2018). The rate of ureolysis and carbonate release can also vary depending on the type of organism (Hammes & Verstraete, 2002; Mitchell et al., 2019; Zhu & Dittrich, 2016).

Equation 2.5 $K_{sp} = [Ca^{2+}][CO_3^{2-}]$

The extracellular polymeric products of bacterial cells have been shown to assist the aggregation of minerals in some cases (Arias & Fernández, 2008; Azulay et al., 2018; Giuffre et al., 2013). Biologically controlled mineralization occurs when there is a specific genetic control of a certain aspect of mineral precipitation (e.g., nucleation or growth) (Benning & Waychunas, 2008). While some bacterial species, such as magneto tactic bacteria, have biologically

controlled intracellular precipitation, often this type of mineralization is associated with higher phyla, such as eukaryotes (Görgen et al., 2021). More recently, plant-based urease extracts have also been used to develop applications of UICP, which are suited to applications where the presence of viable microbial cells may be undesirable (Morasko, 2018).

2.2.2 Kinetics of Precipitation During Biomineralization

The classical nucleation theory conceptualizes the fate of individual ions from homogenous nucleation to monomer-by-monomer crystal growth and precipitation. Homogeneous nucleation is when a critical nucleus is formed in solution, and the system moves towards mineral growth instead of dissolution. The precipitation process arguably starts at nucleation, when a critical nucleus is formed. A critical nucleus is a metastable stage where the assembly of molecules (e.g., $CaCO_3$) is at a critical size when an infinitesimal change towards a smaller nucleus will lead to dissolution and towards a larger nucleus will lead to the growth of the nucleus. This critical nucleus size is the critical radius (r_c) needed for nucleation to proceed toward crystal growth. The kinetics of the formation of r_c can be evaluated by the free energy of the molecules, bulk solution, and a crystal nucleus. The free energy change per molecule (Δg) is given by the sum of bulk free energy (Δg_b) and surface free energy (Δg_s) of the nucleus.

Equation 2.6 $$\Delta g = \Delta g_b + \Delta g_s$$

Equation 2.7 $$\Delta g = -[(\frac{4}{3}\pi r^3)/\Omega]k_B T\, ln\sigma + 4\pi r^2 \alpha$$

Change in free energy during precipitation depends on the nucleus r size, Ω is the volume per molecule, σ is supersaturation, and α is the interfacial energy between the nucleus and the solution. K_B is the Boltzmann constant, and T is the absolute temperature. The supersaturation can be defined as:

Equation 2.8 $$\sigma \equiv ln(AP/K_{sp})$$

Where AP is the activity product of reactants, and K_{sp} is the equilibrium constant. According to equation 2.6, the free energy barrier that needs to be overcome to reach critical nucleus size r_c is approached when the sum of Δg_b and Δg_s reach a maximum at $d(\Delta g)/dr = 0$. the critical nucleus radius which is:

Equation 2.9 $$r_c = \frac{2\Omega\alpha}{kT\sigma}$$

This relationship highlights the fact that the r_c is dependent on both supersaturation and interfacial energy. The free energy barrier to nucleation can be lowered, and a smaller critical radius can be stabilized by increasing supersaturation and decreasing the interfacial free energy, such as in the presence of additives and impurities.

According to the classical nucleation theory (CNT), once the critical radius has been reached, the growth of the critical nucleus happens monomer by monomer into a crystal lattice. While that is true for pure systems (with homogeneous nucleation), mineral precipitation in nature occurs in the presence of many biotic and abiotic impurities and starts with heterogeneous nucleation. Research indicates mechanistic differences at nucleation and crystal growth stages, leading to extended classical nucleation theories (De Yoreo, 2003; Evans, 2017). During the process of mineral formation in nature, it has been found that (i) the nucleation occurs at lower concentrations than predicted by CNT pathways, and (ii) the growth of minerals does not follow a monomer-by-monomer pathway in all cases. For example, in the early stages of the formation of calcium carbonate in mollusks and sea urchins, spicules go from prenucleation clusters to transformation into highly crystalline mesoscale structures (Evans, 2017).

Thermodynamic and kinetic factors influence mineral precipitates and their polymorphs that emerge in a solution (De Yoreo, 2003; Evans, 2017). The interactions of organics with the crystal nucleus can influence the interfacial free energy. Favorable interfacial interactions can and stabilize smaller critical radii ,and vice versa. Similarly, an increase in local supersaturation in the presence of biopolymers can influence the probability of nucleation events and, therefore, the nucleation rate. These interfacial dynamics in the presence of organics offer potential parameters to control the kinetics of precipitation for biomimetic synthesis (De Yoreo, 2003; Rybicka-Jasińska et al., 2021).

Other interactions of organics include organics incorporation into minerals, and interactions at mineral surfaces include kinks and terraces (De Yoreo, 2003). These features can emerge as polycrystallinity and nano granularity in biominerals (Harris et al., 2017). The organics and matrix-mediated control parameters are often used to develop hierarchical structures and biomaterials for biomedical applications. Whereas supersaturation is a more commonly used control parameter during the biomineralization of calcium carbonate as a binder for unconsolidated media (e.g., for soil stabilization) and as sealants in fracture remediation of concrete, etc. (Lee & Park, 2018; Phillips et al., 2013; Wu et al., 2021; Zhu & Dittrich, 2016). Unifying the mechanisms of biomineralization and the use of organics as morphology control agents in induced and controlled biomineralization offers an unlimited toolbox for the design of bioinspired structural materials (Harris et al., 2017).

2.2.3 Organics as Morphology and Mechanical Control Agents in Biomineralization

The formation of mesoscale disordered structures during biomineralization is a universal phenomenon (Harris et al., 2017). Often the mesoscale disordered structures transform into ordered crystalline structures guided the cell metabolism and extracellular chemistries or remain as heterogeneous meso-crystalline structures throughout the life of an organism (North et al., 2017). The formation of mesoscale structures and later their transformation to crystalline structures introduces microstructural variations in these minerals (Deng & Li, 2021; Evans, 2017; Harris et al., 2017). These microstructural variations may play an essential role in the mechanical properties of the biocomposites at the meso- and microscale (Deng et al., 2022; Nudelman & Sommerdijk, 2012). It has been shown that the nano-granularity and disorders in biologically controlled biomineralized hierarchical structures aid their mechanical stability (Barthelat et al., 2016). An analysis of eukaryotic biominerals and in-vitro biomimetics of biogenic biomaterials shows that the stiffness of such biomaterials is generally lower than abiotic mineral structures (Bar-Cohen, 2012; Labonte et al., 2017; Strange & Oyen, 2011). Yet, the fracture toughness of biogenc biominerals is higher than their abiotic crystalline counterparts (Harris et al., 2017; Nepal et al., 2023). The fracture toughness of the biogenic mineral structures such as pearl oyster and mollusc shells has been proposed to be high due to crack deflection mechanisms at multiple length scales (Barthelat et al., 2016; Cranford et al., 2013).

A critical analysis of polycrystalline biominerals and their mechanisms of failure by Barthelat et al. (Barthelat et al., 2016) suggests that the relationships between stiffness, strength, and fracture toughness in biominerals can be valuable for the design of engineered adhesives. Barthelat hypothesized that the tradeoff between the strength (resistance to elastic deformation)

and toughness (resistance to inelastic deformation) offers a framework for design of modern engineering adhesives. The interface between the biopolymer and mineral needs to be strong enough to ensure stress transfer but weak enough to enable inelastic deformation around minerals to redistribute stresses around holes, notches, defects, and cracks to prevent crack propagation (Gao, 2007). While such weak interfaces in engineered materials may be brittle and prone to fracture, biomineralization can confer inelastic deformation capabilities (Barthelat et al., 2016). Similar relationships between nano-granularity, polycrystallinity, stiffness, strength, and fracture toughness of biominerals have been extensively researched and reviewed for structural applications of biomineralization (Cranford et al., 2013; Deng & Li, 2021; Nepal et al., 2023).

2.3 Adhesive Strength Testing of Biopolymer-Mineral Adhesives

During the initial steps in the development of engineering adhesives, adhesive strengths are generally tested in adhesively bonded joints by lap shear test. The simplicity and low costs associated with specimen manufacture, testing, and data analysis in lap shear tests have contributed to the widespread use of this method (Abramowitch & Easley, 2016). The lap shear test quantifies the adhesive shear strength of a composite for a specific surface and a specific adherend geometry (Banea & Da Silva, 2009). During lap shear tests, the stress concentrations are at the edges of the bonded region, and both shear and peel forces act on the adhesives (Çalık, 2016). It is known that the adhesive strength of a polymer-mineral composite depends on mineral particle size and stiffness, loading, and interfacial bonding in synthetic polymer mineral composites (Fu et al., 2008). Although biomineralized adhesives have not been tested previously in lap shear tests, the fundamentals of lap shear test mechanics for adhesives, in general, can be used to evaluate these composites. During the testing of biopolymer-mineral composites in lap

shear tests, there are two interfaces: composite-adherend interface and biopolymer-mineral interfaces (Fu et al., 2008). Both interfaces contribute to the adhesive strength of the composites during lap shear testing. The most significant factor affecting the adhesive shear strength remains the adhesive bonding of the composite to an adherend interface since the shear forces are concentrated near the adherend interface (Çalık, 2016). The higher the adhesive bonding, the lower the adhesive failure at the adherend interface and the adhesive fails cohesively (within the adhesive). Ideally, the cohesive failure is aimed to be 100% cohesive failure (no adhesive failure) (Abramowitch & Easley, 2016). For this purpose, physical, chemical, and mechanical pretreatments are often used to fully draw upon the strength of the composite without experiencing adhesive failure at the adherend interface (Marques et al., 2020). One of the most common methods to enhance adhesive bonding at the interface is roughening of the surfaces before adhesive application (Banea & Da Silva, 2009; Marques et al., 2020). The outcomes of the lap shear strength tests are reported as the load to failure with respect to the bonded area, and the mode of failure is reported.

Banea et al. reviewed the factors associated with the testing of adhesively bonded lap joints (Banea & Da Silva, 2009). In the lap shear method, the influence of the mechanical stiffness of the adherend and geometry of the lapjoints on the final adhesive shear strength measurement has been well established. The stiffness of adherends influences peel stress concentrations. Therefore, increasing the thickness and modulus of adherends can increase the apparent strength of the bonds. The geometry of the lapjoints, such as the length of adherends, also influences the stress concentrations in a lap joint and the adhesive strength of adhesives. Therefore, the comparisons between strengths are only relevant for similar substrates and geometries. For a comprehensive evaluation of an adhesive system, the adhesive, as well as the

parameters associated with the adhesive system, must be tested substantially across multiple adhesive testing methods. However, in the development phase, frequently only lap shear tests are used to determine and optimize the suitability of an adhesive.

2.4 Current Research in Biomineralization-Inspired Biopolymer-Mineral Composites

Click or tap here to enter text.Guessasma and co-authors investigated the elastic behavior of biopolymer composites with random stiff microstructures in biopolymer-biopolymeric nanoparticle composites and highlighted their potential as eco-friendly alternatives to oil-based polymers and polymer composites (Guessasma et al., 2010). The use of zein particles, a protein derived from corn, was specifically suggested as a viable option for preparing biodegradable plastics. The authors assessed the influence of interface rigidities, zein fraction, and interface quantity on the effective properties of the composite. The results revealed a nonlinear correlation between the effective modulus and the product of stiffness parameters. The normal stiffness had the most significant impact on the failure mechanisms in the composites. Additionally, the study demonstrated a logarithmic relationship between the effective properties and the stiffness parameters with an increase in the zein fraction. The study also underscored the importance of understanding interface properties in determining the effective properties of starch-zein composites. The intrinsic mechanical properties of starch and zein were found to be similar, but the phase distribution and interfacial bonding significantly influenced the composite's mechanical behavior. These findings contribute to an understanding of the behavior of biopolymeric nanoparticles in improving the stiffness of biopolymers, which can be used for similar composites in other applications, e.g., as adhesives.

Li *et al.* developed an oyster-inspired adhesive using amorphous calcium carbonate nanoparticles and polyacrylic acid (PAA) crosslinking chemistry (Li et al., 2018) . The study demonstrated that the incorporation of negatively charged nanoparticles enhanced the adhesion strength and stiffness of the amorphous calcium carbonate-polyacrylic acid hydrogel adhesive, leading to improved adhesive properties in both wet and dry conditions. The addition of negatively charged nanoparticles, such as Au, Fe_3O_4, Laponite, or Cu_2O, to the calcium carbonate-polyacrylic acid hydrogel significantly improved the adhesion strength. Even minimal amounts of these nanoparticles (0.003 or 0.1 wt. %) lead to increases of 30-70% in lap shear strength under both dry and wet conditions. Further analyses with Cu_2O nano-cubes showed a substantial enhancement of adhesive strength on aluminum substrates. This reinforcement was attributed to the formation of multiple crosslinks between polyacrylic acid chains on the added nanoparticles, producing more loops, tails, and strands. The physisorption of polyacrylic acid chains on the negatively charged nanoparticles occurs via intermediate Ca^{2+} ions, which are highly reversible. The addition of nanoparticles also affected the rheological behavior of the hydrogels. The nanoparticle-containing hydrogels exhibited higher values of storage modulus (G') and loss modulus (G"), indicating increased stiffness and viscosity compared to the pure amorphous calcium carbonate-polyacrylic acid hydrogel. The relaxation time (τ^*) of the nanoparticle-containing hydrogels became longer, reflecting higher activation energy for the breaking of crosslinks, indicating a denser network and stronger adsorption sites for the polymer in the presence of nanoparticles. Furthermore, the addition of nanoparticles results in a reduced swelling ratio and increased modulus of the dried hybrid film, indicating improved dry adhesion and increased stiffness of the adhesive. The key takeaway from this work was that the stiffness of the adhesive is crucial for its cohesion strength in the dry state, and the introduction of foreign

nanoparticles contributes to an enhancement in the cohesive strength of nanoparticle composite hydrogels.

Li *et al.* demonstrated that the addition of glutaraldehyde functionalized hydroxyapatite nanoparticles to the soy protein adhesive results in improved adhesive strength and water resistance of the composite adhesives (Li et al., 2022). The addition of glutaraldehyde-hydroxyapatite nanoparticles enhanced the wet shear strength of the soy protein adhesive. The biomineralization of hydroxyapatite nanoparticles established an inorganic mineralized framework within the soft protein matrix and improved the adhesion of the composites. The physical adsorption between the soy protein matrix and the reinforcing phase of glutaraldehyde-hydroxyapatite further enhanced the cohesive strength of the polymer, resulting in a stronger bonding effect. The optimized phenol-amine chemical system achieved through interactions between glutaraldehyde-hydroxyapatite and SP chains contributed to the maximum wet shear strength of the adhesive. The incorporation of glutaraldehyde-hydroxyapatite hybrids also enhanced the water resistance of the adhesive. The combination of a mineralized skeleton and organic phase improves both the cohesive strength and surface adhesion of the adhesive, leading to enhanced water resistance. The cohesive properties of the adhesive were hypothesized to be strengthened by sacrificial bonds and efficient energy dissipation during the fracture process. This synthesis approach, while complex, provides a versatile route for developing high-performance biopolymer materials for various applications, including adhesives, hydrogels, coatings, and films.

Cao *et al.* demonstrated that the incorporation of tannic acid and hydroxyapatite complexes in soybean meal-based adhesives improves adhesive strength, water resistance, and fracture resistance, making them suitable for various practical applications (Cao et al., 2021).

The addition of hydroxyapatite and tannic acid complex to soybean meal-based adhesives had several effects on their properties. Firstly, the adhesive strength was improved due to enhanced crosslinking density. The wet shear strength of the adhesive increased, resulting in better adhesion between surfaces. The incorporation of tannic acid and hydroxyapatite complexes enhances the toughness by promoting strong interactions with soybean meal and forming hydrogen bonds and coordination bonds within the adhesive. This results in a more flexible network that can dissipate energy and resist crack formation. The addition of tannic acid and hydroxyapatite complex increased the crosslinking density, thereby potentially inhibiting the diffusion of water molecules. As a result, the moisture absorption of the adhesive was reduced, indicating better water resistance. The residual ratio of the adhesive, which measures its resistance to water degradation, is also increased with the addition of the complex. The adhesive's fracture mechanism was influenced by the presence of tannic acid and hydroxyapatite complex. The adhesive without the complex showed weak adhesion strength and brittle characteristics, resulting in uneven coating and large grooved cracks on the surface. The addition of hydroxyapatite improved the fracture surface, reducing the size of cracks. However, the incorporation of tannic acid and the hydroxyapatite complex significantly enhanced the internal structure of the adhesive. The fracture surfaces become smoother with no cracks or holes, indicating a uniform and compact structure. The presence of tannic acid and hydroxyapatite complex also enhanced the interaction between the adhesive and the wood matrix. The phenolic groups on tannic acid formed multiple interactions with the wood matrix, including hydrogen bonds, hydrophobic interactions, and mechanical interlocking. The improved interactions at the nanoparticle and soy meal polymer interfaces contributed to the enhanced adhesive strength of the composites.

2.5 Summary

Currently, several methods are being investigated for the development of sustainable biopolymer-mineral composites for structural and adhesive applications. Many of these methods involve the use of nanofillers and nanoparticles in biopolymers instead of biomineralization reactions themselves. Both in-situ and ex-situ production of mineral precipitates by biologically controlled and biologically induced calcium carbonate mineralization methods remain unexplored in the adhesive composite's domain. The biologically induced mineral precipitation, specifically ureolytically induced calcium carbonate precipitation, carried out by bacteria is the most cost-effective method for the preparation of biominerals. Yet, there is little control on mineral precipitation during ureolysis, except by supersaturation conditions. This kinetic control in ureolytically induced mineral precipitation by supersaturation is highly underscored by the role of organics. For reliable and reproducible production of biopolymer mineral composites by biomineralization, other control parameters, such as the use of organics, need to be considered, evaluated, and optimized. The use of organics offers additional benefits in terms of nanoscale heterogeneity, which can improve the mechanical performance of biopolymer mineral composites by crack deflection and stress distribution mechanisms at the nanoscale. However, fundamental research needs to be performed to measure these microscale material properties of biominerals formed by biologically induced mineralization processes. The development of biopolymer-mineral composites for adhesive applications also includes their optimization using standard testing methods and an evaluation of their performance across different surfaces and geometries. In this work, we focus on the optimization of the adhesive strength of four different biomineral-biopolymer adhesives (formed by microbially and enzymatically induced calcium

carbonate precipitation in guar gum and soy protein biopolymers. The adhesive strength of these adhesives is optimized on glass and stainless-steel surfaces. We also test the durability of different biomineral-biopolymer adhesives against a range of environmental factors to determine a working range for the adhesive applications. The influence of a biomacromolecule, bovine serum albumin, on the micron to submicron scale material properties of the mineral precipitates are also tested to identify further control parameters for the development of biomineral-based adhesives. Overall, this work will support the advancement of ureolytically induced calcium carbonate composites for use in biobased composites and adhesives applications.

CHAPTER THREE

STRENGTHENING BIOPOLYMER ADHESIVES THROUGH UREOLYSIS-INDUCED CALCIUM CARBONATE PRECIPITATION

Contribution Of Authors and Co-Authors

Manuscript in Chapter 3

Author: Sobia Anjum

Contributions: Designed and conducted the experiments, analyzed data, and compiled the manuscript.

Co-Author: Kendall Parks

Contributions: Conducted experiments and reported data outcomes.

Co-Author: Kaylin Clark

Contributions: Conducted experiments and reported data outcomes.

Co-Author: Albert Parker

Contributions: Supported image analysis and statistical analyses of data.

Co-Author: Chelsea M. Heveran

Contributions: Supported image analysis, statistical analyses, writing, and manuscript review process.

Co-Author: Robin Gerlach

Contributions: Supported experiment design, data analysis, writing, and manuscript review process.

Manuscript Information

Sobia Anjum, Kendall Parks, Kaylin Clark, Albert Parker, Chelsea M. Heveran and Robin Gerlach

ACS Applied Polymer Materials

Status of Manuscript:

____Prepared for submission to a peer-reviewed journal

_X_Officially submitted to a peer-reviewed journal

____Accepted by a peer-reviewed journal

____Published in a peer-reviewed journal

Graphical Abstract

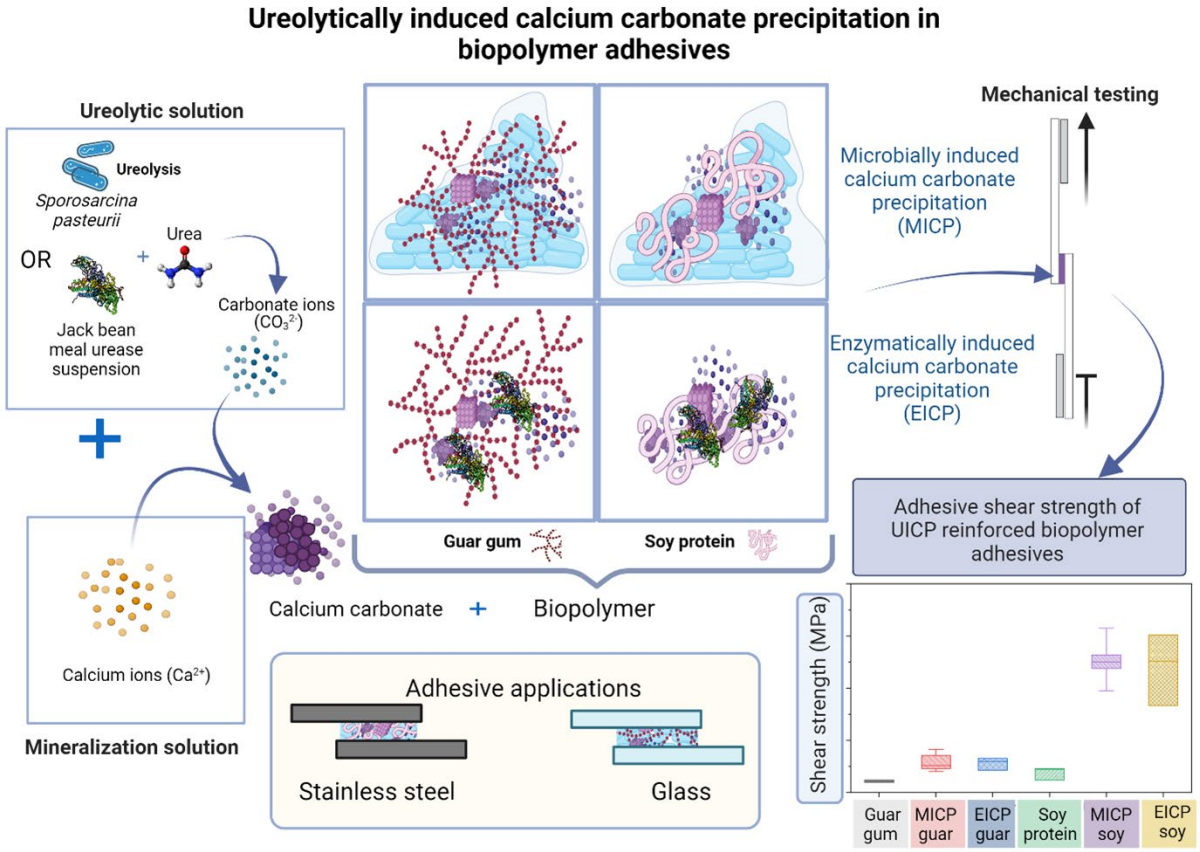

Figure 3.1: Ureolysis and formation of calcium carbonate in the presence of biopolymers to make ureolytically induced calcium carbonate composite adhesives. The graphical abstract is conceptual and is not meant to describe the detailed structure of any interactions in the adhesives at scale.

3.1 Abstract

As the global population grows and urbanization progresses, the demand for adhesives is ever-increasing. Environmental and health concerns linked to fossil-based adhesive materials prompt the exploration of sustainable alternatives. Biobased adhesives may improve sustainability while effectively bonding various substrates, but their adhesive strength has been limited. Mineral fillers may improve the strength of these types of biopolymer adhesives but

require the use of crosslinkers that lower process sustainability. This work demonstrates the effect of biomineralization-induced calcium carbonate on the adhesive strength of biopolymers. Biomineral fillers produced by either microbially or enzymatically induced calcium carbonate precipitation (MICP and EICP, respectively) were precipitated within guar gum and soy protein biopolymers. Both MICP- and EICP-reinforced calcium carbonate increased the adhesive shear strength of the biopolymer adhesives. The adhesive strength of the biomineral-reinforced adhesives was further improved by varying the concentrations of bacteria, urease enzyme, and calcium. This study demonstrates the feasibility of using calcium carbonate-based biominerals to improve the properties of biopolymer adhesives, which increases their potential viability as more sustainable adhesives.

Keywords: Biocomposites, biomineralization, ureolysis, biopolymer materials, biopolymer-mineral composites, organic-mineral, natural adhesives, water-based adhesives.

3.2 Introduction

The United States is one of the major producers and consumers of adhesives and sealants (*Adhesive and Sealant Demand Worldwide 2019*). Most of the 7.8 million pounds of adhesives and sealants used in the United States each year are derived from petrochemical feedstocks (*U.S. Adhesives and Sealants Market Size Report, 2022-2030*). Construction adhesives containing petrochemical and synthetic solvents release volatile organic compounds (VOCs) at varying rates, leading to an indoor accumulation of VOCs and rising human health concerns such as sick building syndrome (EPA & Environments Division, 1991). Studies conducted in South Korea (Shuai et al., 2018), China (Du et al., 2014), Iran (Hazrati et al., 2016), Canada (Zhu et al., 2013), Europe, and the US (Adgate et al., 2004; Frey et al., 2014; Hun et al., 200; Li et al., 2021;

Wickliffe et al., 2020) show that a large variety of VOCs indoors can have varying cancer and non-cancer related detrimental human health effects. These rising environmental concerns and awareness of the detrimental health effects of VOCs have resulted in increasingly stringent regulations and a demand for biobased adhesives with little to no VOC emission (Cui et al., 2023; Li et al., 2023).

Biobased adhesives often fit the safety and sustainability criteria for green construction (*Green Buildings at EPA*.) due to their renewability, low VOC, and low greenhouse gas emissions during production and use (Heinrich, 2019). Biobased adhesives include plant-based biopolymers such as polysaccharides, proteins, oils, and tannins (Heinrich, 2019). Among polysaccharides, natural gum adhesives have been of high interest in the food and packaging industry due to their low toxicity, ready availability, and film-forming properties (Parija et al., 2001). Prominent protein-based adhesives include soy-based adhesives, which have been developed for wood applications due to the ready availability, low cost, and low toxicity of soy flours and soy proteins (Frihart, 2015). However, unmodified biopolymer-based adhesives, both polysaccharides and proteins, have low adhesive shear strength as compared to commercial petrochemical adhesives (Frihart, 2015; Heinrich, 2019; Lamaming et al., 2021).

The low strength of the biobased adhesives can be improved by covalent modifications of the protein (Hettiarachchy et al., 1995; Podlena et al., 2021; Wang et al., 2019) and carbohydrate molecules (Tripathi et al., 2019), mineral and fiber additives (Jensen et al., 2015; Podlena et al., 2021; Xu et al., 2020), or a combination of these approaches (Heinrich, 2019; Post et al., 2021). Several studies have shown that mineral-based modifications of biopolymers, such as the addition of calcium carbonate (Liu et al., 2010), montmorillonite (Qi et al., 2016), functionalized clays (Qi et al., 2016), and nanocrystalline cellulose (Podlena et al., 2021), can improve the

adhesive shear strength and durability of soy-based adhesives. However, the biopolymer mineral composites made by abiotic and geological mineral fillers have weak interfacial interactions, poor dispersion, and high rigidity (Li et al., 2021). Increasing the strength of these types of mineral-reinforced adhesives requires improving interfacial bonding between the mineral and polymer phases, but these modifications have downsides of increasing the cost of applications, process complexity, and using chemicals of environmental concern (Cui et al., 2023; Höfer et al., 2019; Packham, 2009). Therefore, it is desirable to develop synthesis methods that allow the strength benefits of mineral-reinforced adhesives while reducing negative impacts on sustainability.

Biomineralization induced by ureolysis has been used for a wide variety of applications, such as soil stabilization, concrete remediation, well leakage remediation, and the creation of subsurface barriers (Phillips et al., 2013; Wu et al., 2021), but has not yet been utilized to generate biomineral fillers to strengthen adhesives. In ureolytically induced calcium carbonate precipitation (UICP), urea is hydrolyzed by urease to ammonium and carbonate. The UICP reaction can be summarized as follows (Phillips et al., 2013).

$$H_2N - CO - NH_2\ (urea)\ +\ 2H_2O\ +\ Ca^{2+}\ urease \rightarrow\ 2NH_4^+\ +\ CaCO_3(s)$$

Urea hydrolysis releases carbonate ions, which precipitate out as calcium carbonate in the presence of sufficient calcium ions. The ureolysis rate and the concentration of calcium ions can serve as control parameters for the precipitation of calcium carbonate (Knorre & Krumbein, 2000). Ureolysis can be carried out at ambient temperatures by ureolytic bacteria (Phillips et al., 2013), ureolytic fungi (Wylick et al., 2021), and solutions or suspensions of the enzyme urease derived from microbial or vegetable sources (Feder et al., 2021). In prior work with calcium carbonate produced by UICP, microbial cells, and organic components act as an adhesive that

binds and/or seals the surrounding soil or concrete matrix (Hoffmann et al., 2021). These results suggest that UICP could be utilized to generate biomineral fillers within a polymer matrix and that this *in situ* precipitation could result in a strong adhesive. However, this idea has not yet been tested.

The goal of this study was to determine the influence of *in situ* precipitation of biomineral fillers, by microbially induced calcium carbonate precipitation (MICP) or enzymatically induced calcium carbonate precipitation (EICP), on the adhesive shear strength of biopolymer adhesives. In this investigation, the impacts of MICP and EICP on adhesive strength were studied for two types of biopolymers: guar gum and soy protein. Furthermore, additional optimization with respect to cell density and biomineralization solution chemistry was performed to increase the strength of the adhesives. These results demonstrate considerable strengthening (up to 6 times stronger) of adhesives through UICP-induced biomineral fillers on common surfaces (*i.e.*, glass and stainless steel).

3.3 Materials and Methods

Jack bean powder and BD Difco^{TM} Nutrient broth were purchased from Sigma Aldrich and Fisher Scientific, respectively. Guar gum and soy protein were purchased from Sigma Aldrich and MP Biomedicals (Fisher Scientific), respectively. All solutions were prepared in deionized water with an electrical resistivity of $\geq$ 18.2 MΩ.

3.2.1. Microbially Induced Calcium Carbonate Precipitation (MICP)

Microbially induced calcium carbonate precipitates were prepared by mixing a culture of the bacterium *Sporosarcina pasteurii* with a mineralization solution. Bacterial cultures were prepared by inoculating 100 ml of filter-sterilized growth medium (0.33M urea, 0.18M NH_4Cl,

3g/l Nutrient broth) with 1ml of a thawed *S. pasteurii* (ATCC11859) stock culture, which was incubated overnight at 30 ˚C and 150 rpm. One milliliter of the overnight culture was transferred into 100 ml of fresh growth medium and incubated again overnight at 30 ˚C at 150 rpm. This bacterial culture was harvested at 20-22 hours after achieving an optical density of 0.4 ±0.05 (mean ±SD) measured at 600nm (OD_{600}). The bacterial cultures at OD 1.0 were prepared by centrifuging the overnight culture at 5000 rpm for 5 minutes. The cell pellet was harvested and resuspended in a sterile growth medium to reach an OD of 1.0 ±0.05. The optical densities were measured in a flat bottom 96-well plate (Polystyrene, Greiner Bio-One) using a Synergy HT Spectrophotometer (Biotek) at 200µl of liquid, the path length was estimated to be 5mm. Absorbance values for the sterile growth medium were subtracted from sample readings to remove the OD contribution of the growth medium and the plate itself. The mineralization solution had the same composition as the growth medium but contained different concentrations of additional urea and calcium chloride (0.33M, 0.66M, or 1M in equimolar ratios). The bacterial cultures and mineralization solutions were mixed in a 1:1 ratio to achieve calcium concentrations of 0.165M, 0.33M, and 0.5M.

Guar gum (GG) or soy protein (SP) were added to the formulations at 0.7% (w/v) and 10% (w/v), respectively, to produce MICP-GG and MICP-SP adhesives, respectively.

3.2.2. Enzymatically Induced Calcium Carbonate Precipitation (EICP)

Jack bean meal (JBM) solution was prepared by suspending 5 g/l, 10 g/l, 20 g/l, and 30 g/l of fine powdered JBM in deionized water for 4 hours. Before use, the resulting suspensions were filtered through 0.22 µm pore size bottle top filters (Nalgene Rapid-Flow Filters, Thermo Scientific). Mineralization solutions were prepared with urea and calcium chloride at 0.33M,

0.66M, and 1M concentrations. JBM and mineralization solutions were mixed in a 1:1 ratio to achieve 0.165M, 0.33M, and 0.5M calcium concentrations. GG and SP were added at 0.7% (w/v) and 10% (w/v) to make EICP-GG and EICP-SP adhesives, respectively.

3.2.3. Lapjoint Assembly and Adhesive Shear Strength Testing

Stainless-steel (316L) and borosilicate glass adherends (25mm x 75mm) were cleaned with deionized water and 70% ethanol. 25mm x 25mm square spacers were attached to each adherend (*cf.* Figure 3.2). The adhesive solution was vortexed for 5s, and 100µl of the composite was applied to a 12.5mm x 25mm edge of one adherend placed flat on a bench top. The other adherend (*i.e.*, a second slide) was placed on top to make a 12.5mm x 25mm overlap area (Figure 3.2, ASTM method D1002-10). No additional external pressure was applied. The sample was allowed to cure for 48 hours at 23 ˚C ±2 ˚C.

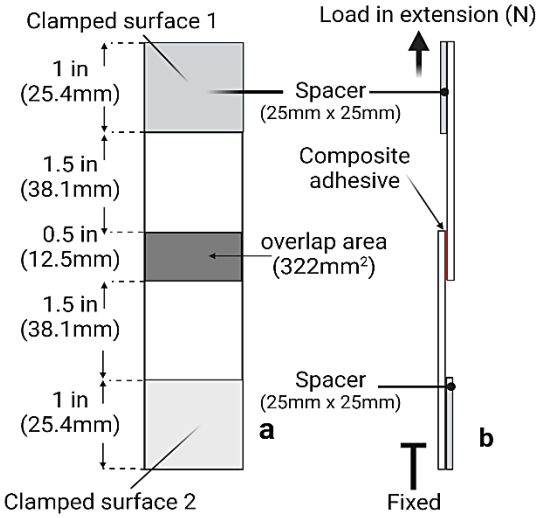

Figure 3.2: Lapjoint dimensions and testing configuration. (a) Lapjoints were prepared by applying adhesive to the marked overlap area, cured, and then tested by (b) lap shear in tensile extension mode.

After curing, the samples were tested at an extension rate of 0.01mm/sec in tensile extension ramp-to-fail mode using an Instron 3340 Series Universal Testing System. The maximum load (N) at the point of bond failure divided by the overlap area (322 mm^2) was used to calculate the adhesive shear strength of the sample in megapascals (N/mm^2).

3.2.4 Surface Roughness and Surface Wettability

Surface roughness (S_a) of glass and stainless-steel surfaces was estimated using a Filmetrics Profilm 3D optical profilometer at 50X magnification on triplicate (300µm x 300µm) regions. The surface wettability of adherends was estimated by measuring the contact angle of deionized water on the glass and stainless-steel using a video contact angle system (VCA2500XE, AST).

3.2.5 Surface Coverage and Mode of Failure Analysis

Image analysis was used to assess the mode of failure of the adhesives. Lapjoint overlap regions were imaged post-fracture using a mobile device (iPhone 12). The images were auto-thresholded in ImageJ using the Otsu method (Otsu, 1979). The surface coverage was calculated as the sum of the adhesive remaining on both sides (arbitrarily assigned a and b) of the fractured lapjoint. The failure mode of the bonded regions was calculated based on three predicted modes of failure: adhesive, cohesive, and mixed (adhesive and cohesive). If the adhesive remained on both sides of the lapjoint post-fracture, cohesive failure was assumed to have occurred within the adhesive. The remaining regions were assumed to have adhesive or near-surface adhesive failure. The percentage of cohesive (CF) and adhesive failures (AF) was determined using Eq. 3.1 & 3.2.

$$CF = |100 - (surface\ coverage\ adherend\ a + b)| \quad \text{Eq.3.1}$$

$$AF = (100 - CF) \quad \text{Eq.3.2}$$

3.2.6 Statistical Analysis

Three-way ANOVA was used to assess whether adhesive shear strength depended on biopolymer type (soy protein or guar gum), calcium concentration, bacterial OD, or their interactions. Three way-ANOVAs also tested whether adhesives strength and percentage of adhesive failure for MICP-SP adhesives depended on surface type, calcium concentration, bacterial OD, or their interactions. Two-way ANOVA tested whether adhesive shear strength depended on biopolymer type, enzyme concentration, or their interaction for EICP-reinforced adhesives. Critical alpha was set as 0.05 a priori. Residuals were checked for normality and equal variance for all models. Post-hoc testing was performed for significant interactions using a Tukey correction to adjust critical alpha for family-wise error.

3.4 Results and Discussion

3.3.1 Adhesive Performance of Biopolymers is Improved by Ureolytically Induced Calcium Carbonate Precipitation

This work demonstrates that the adhesive shear strength of biopolymer adhesives is improved through the *in situ* precipitation of biomineral, whether from microbially induced calcium carbonate precipitation (MICP) or enzymatically induced calcium carbonate precipitation (EICP). MICP increased the adhesive shear strength of biopolymers by 2.5 (guar gum) to 5.7 (soy protein) times when measured for glass surfaces (Figure 3.2, Table 3.S1). On stainless steel, the strength gain with biomineralization was even higher (6 times for soy protein, Figure 3.5, Table 3.S1). The increase in adhesive strength achieved with EICP were similar to MICP (Figure 3.3 & 3.4, *cf.* Tables 3.S1 & 3.S2). These improvements in adhesive shear strength with the inclusion of biomineral fillers align with results from other studies (Liu et al., 2010; Qi

et al., 2016; Sun et al., 2021), except that the biomineralization method requires no additional modifications of the biomineral-biopolymer interface to achieve these strength improvements.

A key finding is that microbial and enzymatic sources of the ureolytically induced mineral fillers in biopolymers achieved similar increases in adhesive shear strength of biopolymer adhesives. These strengths, as high as 1-2 MPa for the EICP or MICP-reinforced soy protein, are suitable for several light-duty adhesive applications (e.g., bonding floor and wall coverings, panels, fibers, particle boards, etc.). Since their strengths are similar, choosing EICP or MICP for biomineralization of biopolymer adhesives may depend on competing practical considerations. EICP can be performed relatively easily and quickly (minutes to a few hours) using powdered jack bean meal urease or another source of urease, while MICP requires live microbial cultures, which require longer preparation times (24 hours or more). On the other hand, jack bean meal powder with high urease activity has a higher cost than the raw materials needed for microbial growth and requires the use of agricultural land for non-food purposes. In a time-cost trade-off, MICP would be more suitable for large construction projects or commercial applications, while EICP might be preferable for smaller custom applications or when time is the primary concern.

While the choice of biomineralization method (MICP vs. EICP) did not substantially affect adhesive strength, the type of biopolymer matrix was an important determinant of strength. Soy protein as a biopolymer matrix resulted in higher adhesive strength than guar gum, even without biomineral reinforcement (0.22 MPa for SP vs. 0.11 MPa for GG on glass). After biomineralization, the soy protein biopolymers improved in adhesive strength up to 1.26 MPa for MICP and 1.24 MPa for EICP, respectively. In contrast, the guar gum biopolymer adhesive strength increased only up to 0.28 MPa for MICP and 0.28 MPa for EICP, respectively. These

differences in adhesive performance by biopolymer type may be associated with their inherently different polymer chemistry (protein vs. polysaccharide) and structural variations in the resultant biopolymer-biomineral adhesives, as shown by scanning electron microscopy (Figure 3.S1 & 3.S2).

3.3.2 Calcium Concentrations Control the Adhesive Shear Strength of MICP-Reinforced Biopolymer Adhesives.

Because the kinetics of MICP are well-known to depend on cell density (OD_{600}) and the concentration of the biomineralization solution (i.e., calcium concentration) (Lauchnor et al., 2015; Murugan et al., 2021; Knorre & Krumbein, 2000), these parameters were varied to optimize the adhesive shear strength of MICP-reinforced biopolymer adhesives. There was a significant interaction between the effect of biopolymer type and calcium concentration on the adhesive strength of MICP-reinforced adhesives ($p < 0.001$, Table 3.S3). The effect of cell concentration (range tested OD 0.4-1.0) on the adhesive shear strength of MICP-reinforced adhesives was not significant ($p = 0.33$). The optimal calcium concentration differed for the two types of biopolymer adhesives (range 0.165-0.5M). For guar gum, the adhesive strength was optimal at 0.165M calcium concentration, whereas for soy protein, the adhesive strength was optimal at 0.33M calcium (Figure 3.3). Notably, the glass slides failed before the adhesive during shear strength testing for several MICP soy protein adhesives (0.33M and 0.5M calcium concentrations, at OD 0.4 and 1.0). This substrate failure shows that the adhesive bond was stronger than measurable with the glass substrates. Therefore, our results may underestimate the adhesive shear strength of some of the stronger MICP soy protein adhesive preparations.

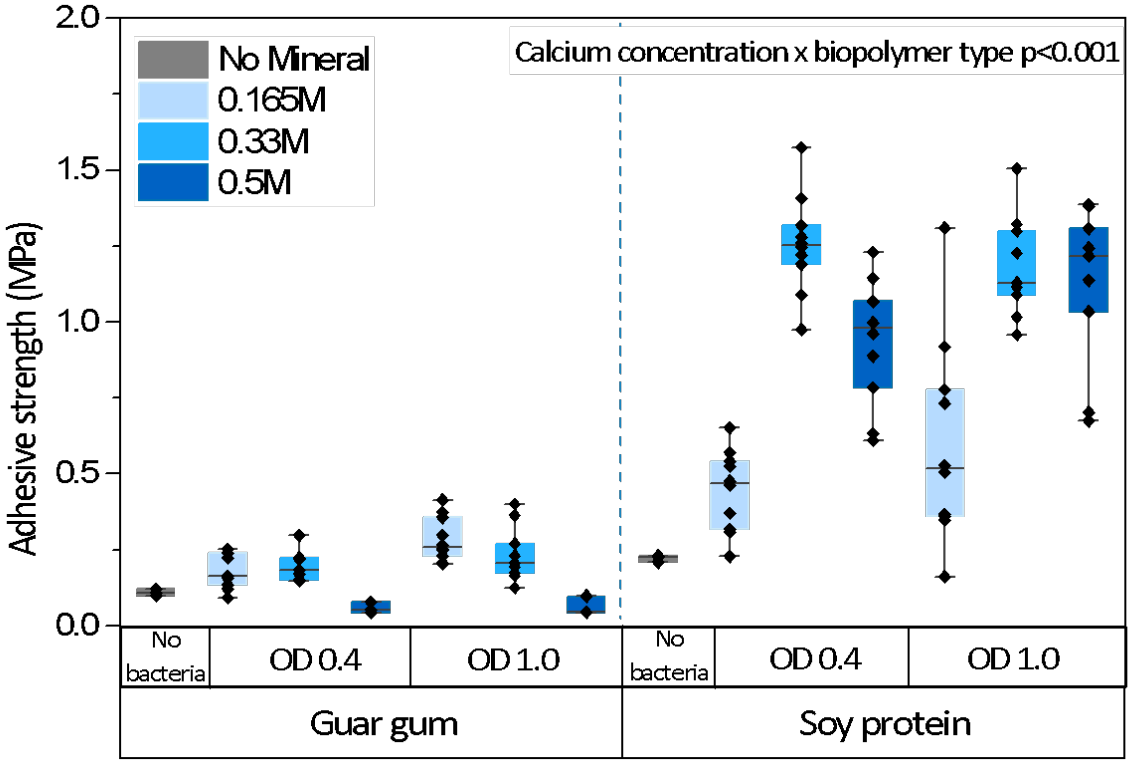

Figure 3.3**:** Adhesive shear strength of guar gum- and soy protein-based microbially induced calcium carbonate adhesives on glass lapjoints. The calcium concentrations and bacterial cell density (OD) were varied for each biopolymer (guar gum and soy protein) to optimize the adhesive shear strengths of MICP-reinforced adhesives. Control samples do not contain bacteria and only either soy protein or guar gum in DI water. The upper and lower bounds of the boxplot represent the 25th and 75th percentiles, and the whiskers indicate minimum and maximum values. The median is indicated by a horizontal straight line.

The effect of calcium concentration on the adhesive shear strength of the MICP-reinforced adhesives can be interpreted in terms of ureolysis (rate and extent), calcium carbonate precipitation rates, and calcium carbonate content. Ureolysis by *S. pasteurii* is described by first-order kinetics with respect to urease (Lauchnor et al., 2015), and the rate of calcium carbonate precipitation is proportional to the rate of ureolysis (Mitchell et al., 2019). As the calcium concentration increases, mineral (calcium carbonate) content within the adhesive increases as well. For MICP in soy protein matrices, the adhesive shear strength increased as calcium

concentrations increased from 0.165M to 0.33M. High mineral content has been shown to improve the adhesive (Liu et al., 2010) and tensile strength (Fu et al., 2008; Post et al., 2021) of several polymer mineral composites. However, consistent with our observations with MICP and both types of biopolymer matrices, the adhesive and tensile strengths of polymer-mineral composites have been described to decrease beyond an optimal mineral content (Piekarska et al., 2017; Post et al., 2021; W. Xu et al., 2019). The strength of biomineralized biopolymer adhesives is likely to depend on mineral volume fraction, mineral dispersion, and mineral-microbe-biopolymer interactions. Investigating which of these candidate mechanisms individually or together confer the strengthening benefit of the biomineral filler was beyond the scope of the present investigation but would benefit from future inquiry.

3.3.3 Enzyme Concentrations and Biopolymer Type can be used to Optimize the Adhesive Shear Strength of EICP-Reinforced Biopolymer Adhesives

The shear strength of EICP-reinforced biopolymer adhesives depended on the biopolymer type (guar gum *vs.* soy protein) and jack bean urease concentration. These experiments were conducted at a calcium concentration of 0.165 M because preliminary analyses indicated that this concentration resulted in the highest adhesive strength for EICP-reinforced guar gum biopolymers (Figure 3.S3, Table 3.S4). Therefore, the adhesive shear strengths of EICP-reinforced adhesives were optimized with respect to urease concentrations at a constant calcium concentration of 0.165M (Figure 3.4).

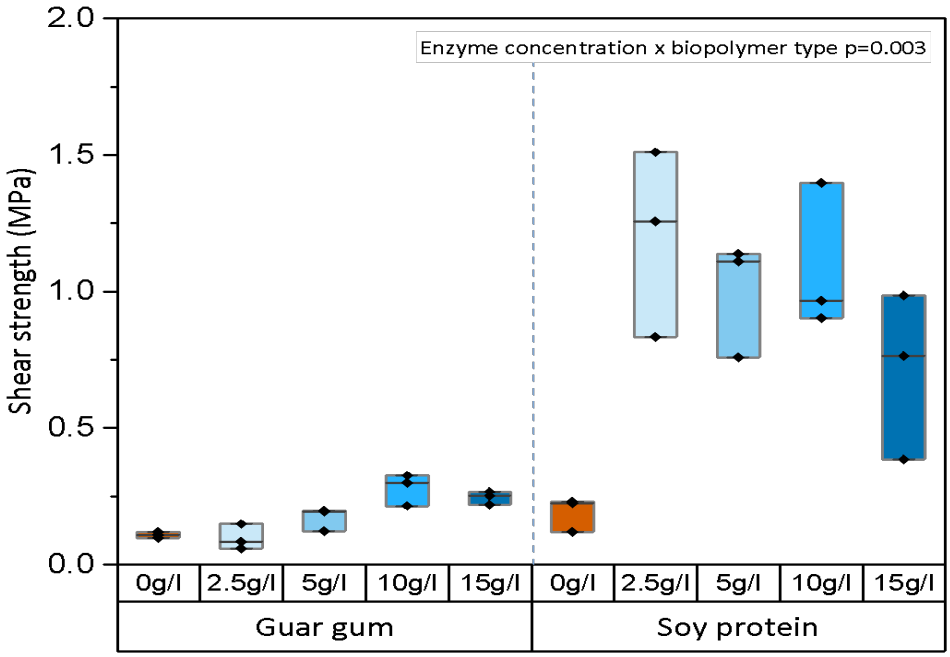

Figure 3.4: Adhesive shear strengths of EICP-reinforced biopolymer adhesives on glass lapjoints. For each biopolymer, urease enzyme concentrations were varied from 0-15 g/l at 0.165M calcium concentrations. Control samples contain soy protein or guar gum in DI water. The upper and lower bounds of the boxplot represent the 25th and 75th percentiles, and the whiskers indicate minimum and maximum values. The median is indicated by a horizontal straight line.

There was a significant interaction between the effect of urease concentration and biopolymer type on the adhesive shear strength ($p < 0.001$, Table 3.S5). Increasing the urease concentration from 2.5 to 10 g/l significantly increased the adhesive shear strength of EICP guar gum adhesives (+65%, $p < 0.001$) but did not significantly affect the adhesive shear strength of EICP soy protein adhesives (-16%, $p = 0.71$). A further increase in urease concentration from 10g/l to 15g/l significantly decreased the adhesive shear strength of EICP soy protein adhesives ($p < 0.001$). These data show that biomineral fillers introduced by both EICP and MICP can achieve meaningful improvements in the adhesive strength of biopolymers by optimizing the precipitation conditions. While both, EICP and MICP-reinforced adhesives, exhibited similar

strength, further analyses related to the influence of surface type and failure characteristics were only performed for MICP-reinforced adhesives.

3.3.4 The Type of Surface Influences the Adhesive Shear Strength of MICP-Biopolymer Adhesives

The strength of MICP-reinforced adhesives was further compared on two surfaces, glass and stainless steel. For MICP soy protein adhesives, there was a three-way interaction between calcium concentration, cell density, and surface type on adhesive shear strength for MICP-reinforced adhesives ($p=0.04$, Table 3.S6). At the lowest studied calcium concentration (0.165M), the adhesive shear strength of MICP-reinforced adhesives was greater on stainless steel than on glass (Figure 3.5). At 0.33M, the strength of the adhesives was similar for stainless steel and glass. At the highest studied calcium concentration (0.5M), the adhesive strength was similar on glass and stainless steel for an OD of 0.4 but was much lower on stainless steel than glass for an OD of 1 (-33%, $p=0.002$). Across these comparisons, a mid-range calcium value (0.33M) was seen to promote adhesive strength best. However, as discussed in 3.3.2, the tendency of the glass to break for some of the replicates (0.33M and 0.5M) before the adhesive failed may underestimate the adhesive shear strength of MICP-reinforced soy protein adhesives and limit the comparison of true adhesive strength of the adhesives by surface type here.

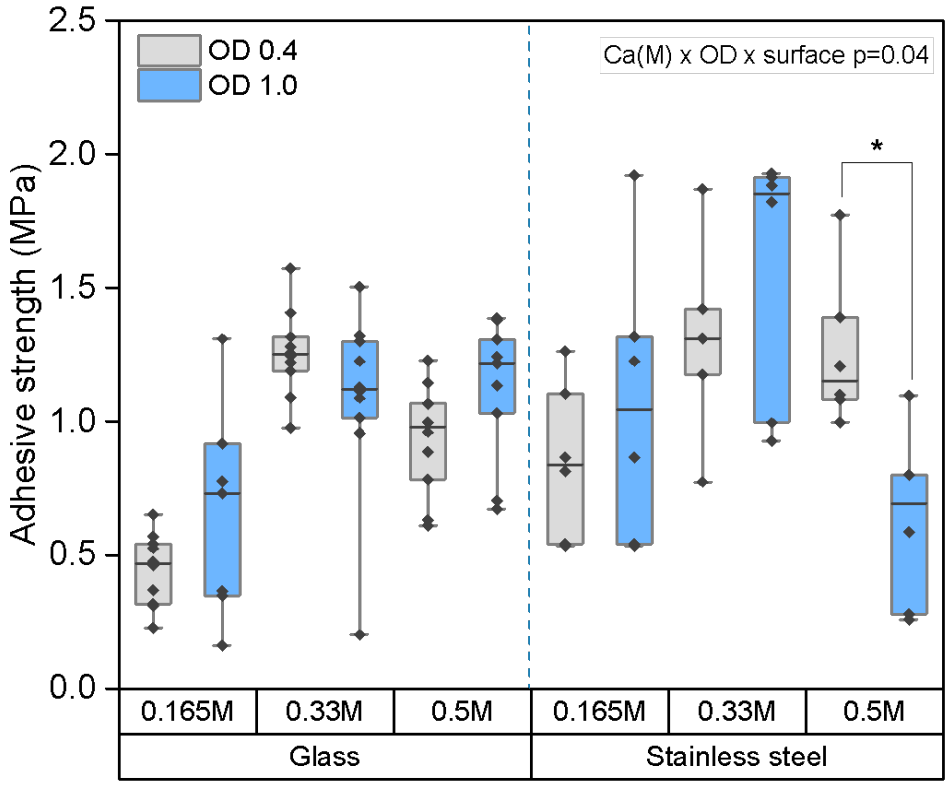

Figure 3.5: The adhesive shear strength of MICP-reinforced soy protein adhesives on stainless-steel and glass substrates at varying urea and calcium concentrations and bacterial cell densities (OD). The upper and lower bounds of the boxplot represent the 25th and 75th percentiles, and the whiskers indicate minimum and maximum values. The median is indicated by a horizontal straight line.

While the MICP-reinforced guar gum adhesives had low adhesive strength on glass surfaces, they had no measurable adhesive strength on stainless steel. These lap joints fell apart while loading into the test frame. These results reinforce the importance of identifying a suitable combination of biopolymer and surface type for specific adhesive applications, as reported earlier in the literature (Budhe et al., 2017; Marques et al., 2020).

3.3.5 Failure Characteristics of MICP-Reinforced Adhesives Dependent on the Surface Type

To add insight into how MICP reinforcement improves adhesive properties, surface coverage and mode of failure were compared across different surfaces and calcium concentrations. After lapjoint failure, the percentage of surface area covered by adhesive on both adherends was summed. In this analysis, 100% total summative surface coverage indicates complete adhesive failure, while 200% indicates complete cohesive failure (Figure 3.6, A & B, Table 3.S8). Less than 100% coverage indicates that some adhesive was lost during testing, such as through spalling or flaking, or that the lapjoint surfaces were not completely covered during application and curing. For most of the tested lapjoints, the summative surface coverage was between 100 and 200%, indicating that a mixed failure (both adhesive and cohesive) occurred. The extent of adhesive and cohesive failure in the mixed failure were estimated by equations 3.1 & 3.2 and shown in Figure 3.6C & D. For glass lapjoints, failure mode analysis was only performed when adhesive failure occurred, as opposed to the failure of the glass substrate itself.

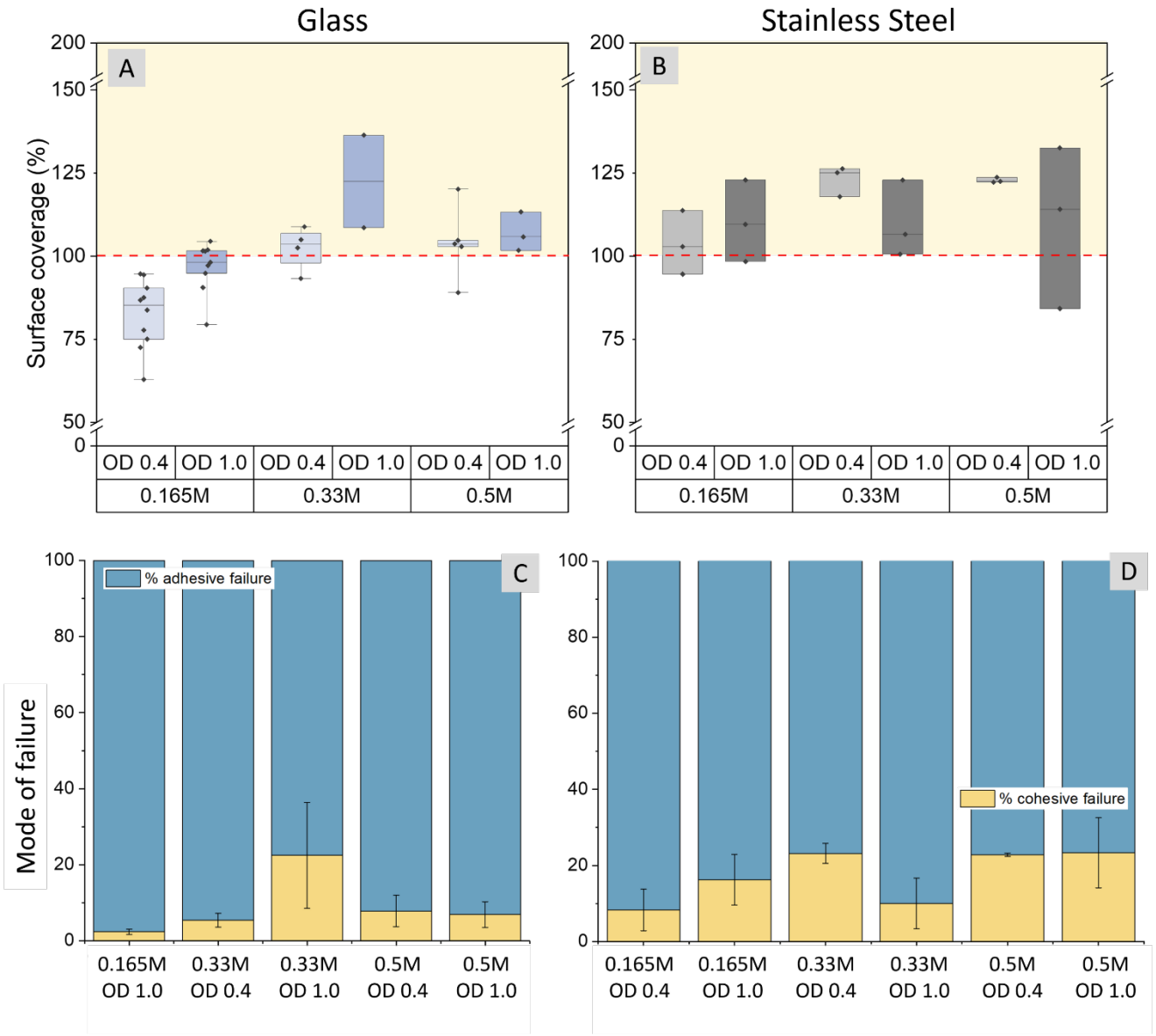

Figure 3.6: Surface coverage and failure mode analysis for MICP-reinforced soy protein adhesive lapjoints. (A, B) Percent surface coverage was measured after the failure of (A) glass lapjoints & (B) stainless-steel lapjoints, as detailed in Figure 3.S4. The values on the y-axis indicate the total surface coverage summed for both sides of the lapjoints. Thus, 100% surface coverage indicates complete adhesive failure while 200% indicates complete cohesive failure; values less than 100% indicate that some material is lost during testing. The upper and lower bounds of the boxplot represent the 25th and 75th percentiles, and the whiskers indicate minimum and maximum values. A horizontal straight line indicates the median. (C, D) The fraction of adhesive and cohesive failure in samples with mixed failure is shown for samples with summed surface coverage between 100 and 200% (yellow shaded regions in A & B). Adhesive failure is indicated in blue, and cohesive failure is tan. Stacked bars indicate the sample means, and whiskers indicate 1 standard error of the mean.

The MICP-reinforced adhesives mostly failed adhesively (Figure 3.6, C & D) with an average of 92.5 ± 8.9% and 82.4 ± 9.3% adhesive failure after testing on glass and stainless-steel surfaces, respectively ($p=0.002$, Table 3.S7). The lower percentage of adhesive failure in the stainless steel lapjoints may indicate a stronger adhesion at the adhesive-adherend interface.

Our data demonstrate that not only adhesive strength but also failure mode depends on the biomineralization precipitation conditions and surface type (Figure 3.6, A & B). On stainless steel, increasing calcium concentrations from 0.165M to 0.5M did not consistently improve strength across all cell densities (Figure 3.5) but improved the cohesive characteristics of the biopolymer-mineral adhesives, *i.e.,* an increase in calcium concentrations from 0.165M to 0.5M decreased adhesive failure from 88 to 77% (Figure 3.6D). On the glass, this same increase in calcium concentration improved strength but did not change the cohesive failure characteristics. Theoretically, the maximum strength of an adhesive can be realized when failure is 100% cohesive, and there is little to no adhesive failure (Ebnesajjad, 2010; Singh et al., 2022). Our results, however, do not demonstrate this correlation between higher adhesive strength and higher cohesive failure of the MICP adhesives on glass or stainless steel (Figure 3.S5).

The increased tendency of adhesives to fail cohesively on stainless-steel lapjoints, as opposed to glass, can be attributed to the higher surface roughness and hydrophobicity of stainless-steel surfaces. Surface profilometry showed that the surface roughness of stainless steel (S_a=0.45 ± 0.0008µm) was an order of magnitude greater than for glass (S_a=0.046 ± 0.0023µm, Figure 3.S6). The surface wettability analysis showed that stainless-steel surfaces had a higher hydrophobicity than glass (Figure 3.S6). The occurrence of stronger adhesive interfacial bonding (generally associated with lower adhesive failure) and higher surface roughness in stainless steel surfaces aligns with the literature indicating that higher surface roughness promotes adhesive

bonding (Frihart, 2015). Studies have also shown that higher surface roughness and greater hydrophobicity can each improve microbial adhesion (Song et al., 2015; George et al., 2003; Ho~evar et al., 2014), biopolymer-surface interactions (Fukuzaki et al., 1995; Wang et al., 2007), and calcium carbonate deposition (Wang et al., 2013). A combination of the surface roughness and wettability and surface-microbe-biopolymer interactions may be responsible for improved adhesion of the MICP adhesives on stainless steel as compared to glass surfaces. Further investigation of mechanisms of mineral-biopolymer-surface interactions would be valuable to understanding their contributions to the adhesive strengths of biomineral-reinforced adhesives.

3.3.6 Sustainability of UICP-Reinforced Biopolymer Adhesives and Prospects

Our results demonstrate that reinforcing biopolymer adhesives using MICP or EICP, both forms of ureolysis-induced calcium carbonate precipitation (UICP), improves their strength towards values useful for everyday applications. These UICP-reinforced adhesives have the potential for improved sustainability in terms of the renewability of reactants and the low environmental and human health effects of their by-products. A principal reason for this improved sustainability is that no organic solvents are used during the production of these adhesives and, therefore, they avoid VOC emissions. Importantly, ureolysis generates ammonium ions, which in environments with pH > 9 or temperatures > 300˚C can convert to ammonia, a volatile inorganic compound with a noxious smell and known health effects. Ammonium ions themselves do not cause these issues. In the manner that these UICP-reinforced adhesives are synthesized, the pH is maintained below 8, and almost all ammonium stays in solution. Further, ammonium forms ammonium chloride in the chemical environment of these adhesives, as confirmed by X-ray diffraction analysis (Figure 3.S2). Together, these data suggest

that the risk of ammonia release and impact for this application is small at ambient temperatures. At higher temperatures (> 300˚C), the concern with ammonia can re-emerge due to thermal decomposition of ammonium chloride into ammonia and HCl gas, requiring ventilation measures in place. Further assessments of the fate of ammonium ions can provide additional validation of the environmental applicability of the UICP-reinforced biopolymer adhesives.

3.5 Conclusions

This work demonstrates that reinforcement of common biopolymers through ureolysis-induced calcium carbonate precipitation can produce adhesives with sufficient strength for indoor applications. Both microbial and enzymatic sources of the urease enzyme successfully strengthened the adhesives without the need for additional processing. Aside from biomineralization, the most critical factor determining the strength of the biomineral reinforced biopolymer adhesives was the type of biopolymer utilized. Specifically, at the concentrations used, soy protein outperformed guar gum as the biopolymer additive of these adhesives. These types of adhesives have the potential for increased sustainability because of the renewability of reactants, zero VOC emissions, and low environmental and human health concerns of its by-products. These findings motivate further investigations of mechanisms of biomineral-organic-surface interactions and their potential contributions to the durability of such biomineral-biopolymer adhesives.

3.6 Acknowledgments

This research was made possible by the Department of Chemical and Biological Engineering and the Center for Biofilm Engineering at the Norm Asbjornson College of Engineering at Montana State University, a Ray and Erin Schultz Emerging Scholars Fellowship, and the United States Education Foundation Pakistan Fulbright Commission. Sobia Anjum was supported by the Thermal Biology Institute through funding from the MSU Office of the Vice President for Research and Economic Development for PhD graduate enhancement. This work was also partially supported by the National Science Foundation (CMMI 20368687 to CH and RG and 1736255 to RG). This work represents the authors' views and opinions, and not necessarily those of the sponsors.

3.7 Supplemental Information

Figure 3.S1 FESEM images show the topographical differences between the MICP-reinforced adhesives by the biopolymer type. Figure 3.S2 shows the distribution of calcium in MICP-reinforced soy protein adhesive. Figure 3.S3 shows the preliminary boxplot data for the optimization of EICP-reinforced adhesives. Figure 3.S4 shows the method for estimating surface coverage and mode of failure in lapjoints. Figure 3.S5 shows the correlation between adhesive strength and cohesive failure on glass and stainless steel surfaces. Figure 3.S6 shows the surface roughness and wettability measurements for stainless steel and glass surfaces.

Tables 3.S1-3.S8 present the adhesive shear strength and surface coverage data used for MICP and EICP-reinforced biopolymer adhesives and their respective statistical analysis results.

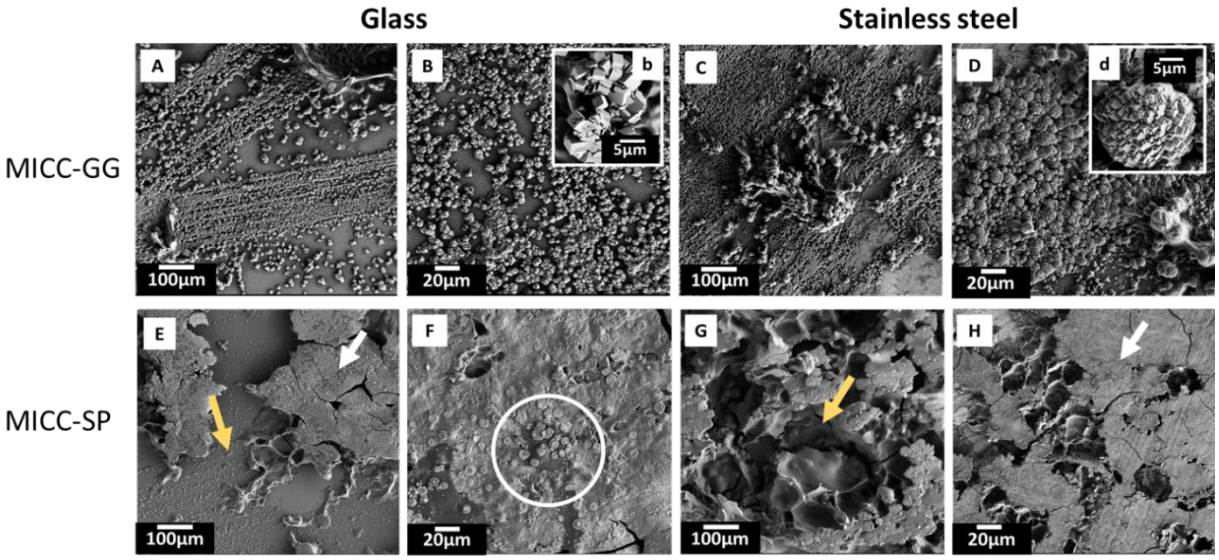

Figure 3.S1: Field Emission Scanning Electron Microscope (FESEM) imaging of MICP-reinforced guar gum and MICP-reinforced soy protein post-fracture. Discrete spherical aggregates in MICP guar gum on (A, B) glass and (C, D) stainless steel. Inset images b & d show that the aggregates are polycrystalline with sharp edges and smooth crystal faces, indicative of polycrystalline calcite. Biopolymer-mineral aggregates in MICP-soy protein on (E, F) glass and (G, H) stainless steel surfaces (EDX in Figure 3.S2). (E) A yellow arrow indicates the glass surface in the background, and a flat region indicated by the white arrow shows potential sites of adhesive failure (delamination) of MICP soy protein on glass surfaces. (F) The MICP soy protein adhesives have circular (potentially mineral) precipitates embedded in the (soy protein) matrix (encircled white). The sites of (G) fracture within the adhesive and (H) delamination on stainless steel are indicated with yellow and white arrows, respectively.

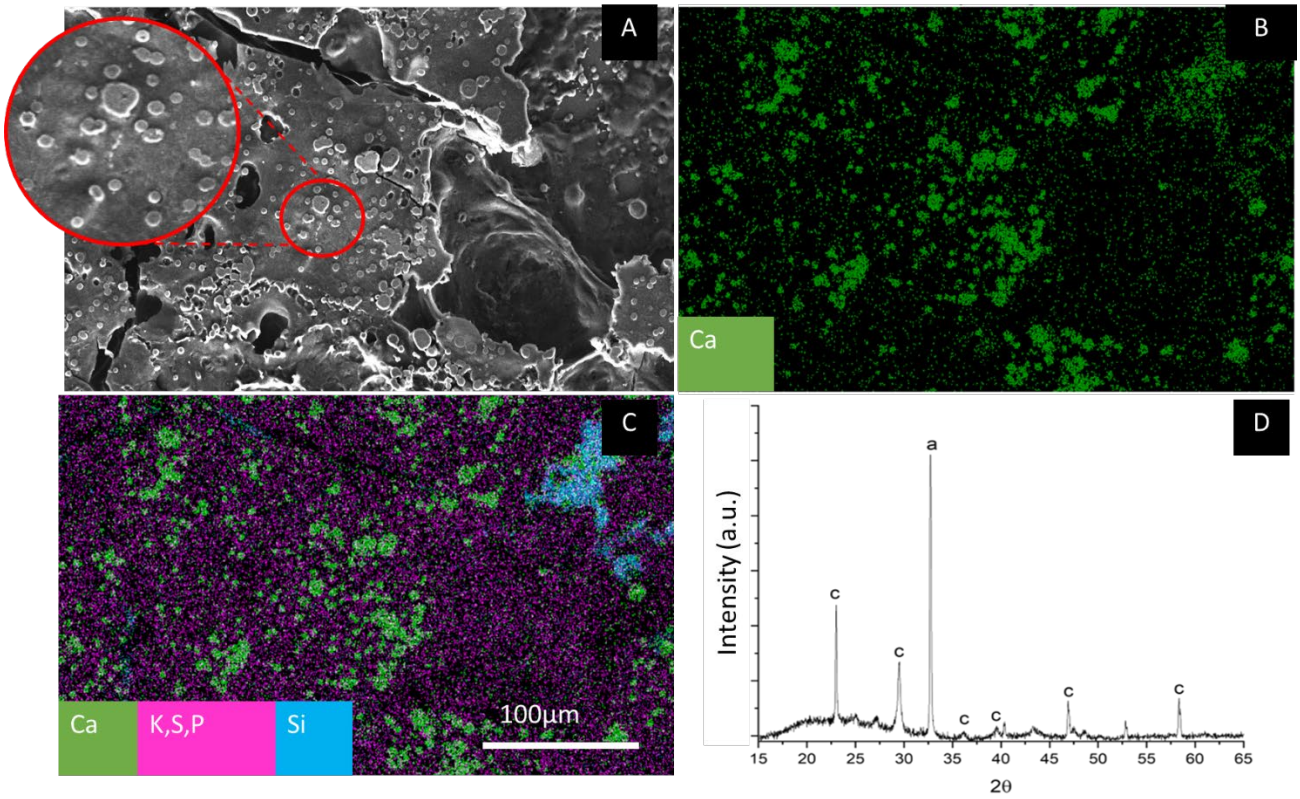

Figure 3.S2: Field Emission Scanning Electron Microscopy Backscattered Electron (FESEM-BSE) imaging and Energy Dispersive Spectroscopy (EDS) elemental mapping of MICP soy protein. (A) The FESEM-BSE image of a MICP soy protein adhesive shows distinct, relatively circular aggregates (encircled red) within the mineral-biopolymer adhesive. FESEM-EDS shows that these are calcium-rich regions. (C) The presence of K, S, and P indicates the presence of an organic (biopolymer) matrix. (D) The presence of calcium carbonate precipitates in the adhesives was confirmed using XRD, indicating a predominance of calcite polymorph (indicated by peaks labeled ‘c’). The peak labeled ‘a’ indicates the presence of precipitated ammonium chloride in the adhesive.

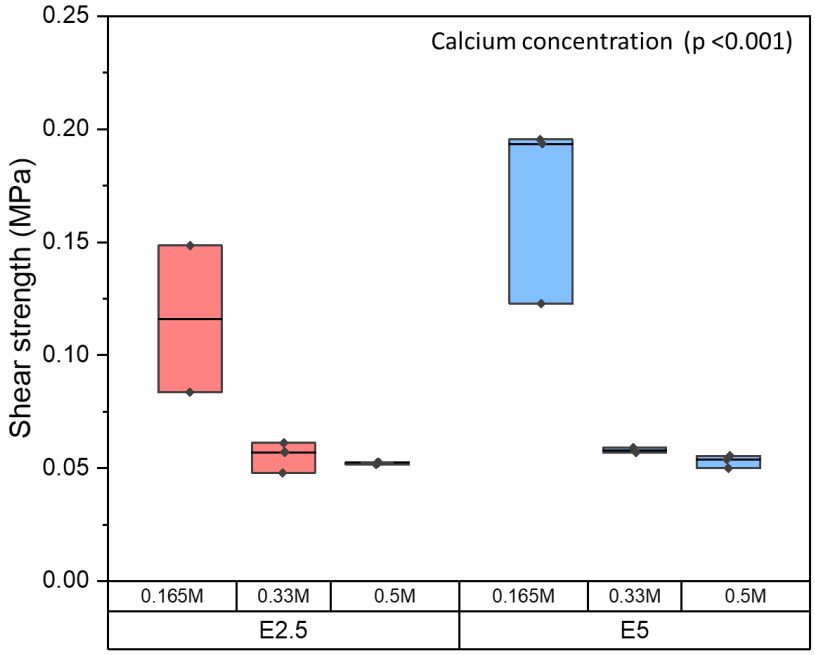

Figure 3.S3: Shear strength of EICP guar gum at varying urea and calcium concentrations (M), and enzyme (E) concentrations 2.5 (red) and 5g/l (blue). The upper and lower bounds of the boxplot represent the 25th and 75th percentiles, and the whiskers indicate the minimum and maximum values. The median is indicated by a horizontal straight line. Statistical analysis results in Table 3.S5.

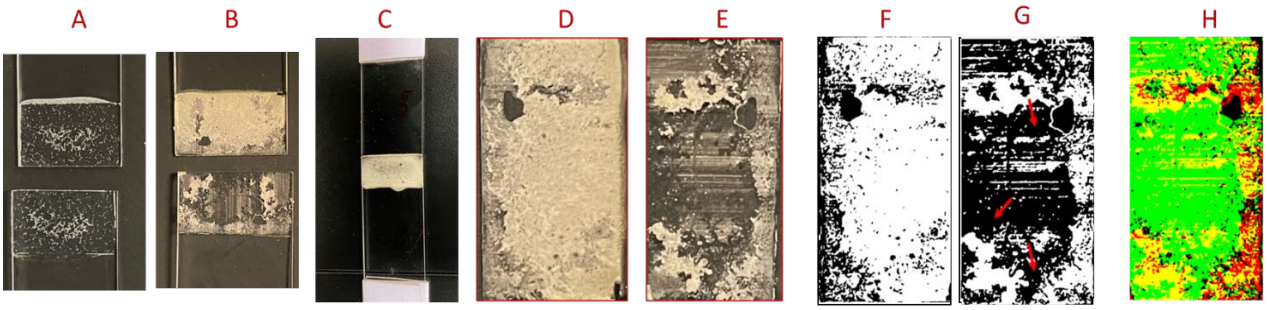

Figure 3.S4: Surface coverage and failure on glass lap joints. (A) MICP guar gum adhesives had incomplete surface coverage of the lapjoints after curing and (B) indicates a mixed failure of a MICP guar gum lapjoint after fracture. (C) MICP soy protein adhesives appear to achieve complete coverage of the overlap area between glass surfaces. Image analysis was performed by considering the (C) initial surface coverage in the overlap area for MICP soy protein as 100%. Surface coverage of the overlap area (D&E) post fracture was measured by thresholding the images using the Otsu method; (F&G) white regions are adhesive coverage against black adherend background and red arrows indicate adhesive or near surface adhesive failure of the adhesives. (H) An overlay image shows the (yellow) overlapping regions indicative of cohesive failure in the adhesives. The red and green areas are adhesive coverage on bonded sides D&E, yellow regions indicate an overlap in surface coverage (indicating cohesive failure), and black regions have little or no adhesive.

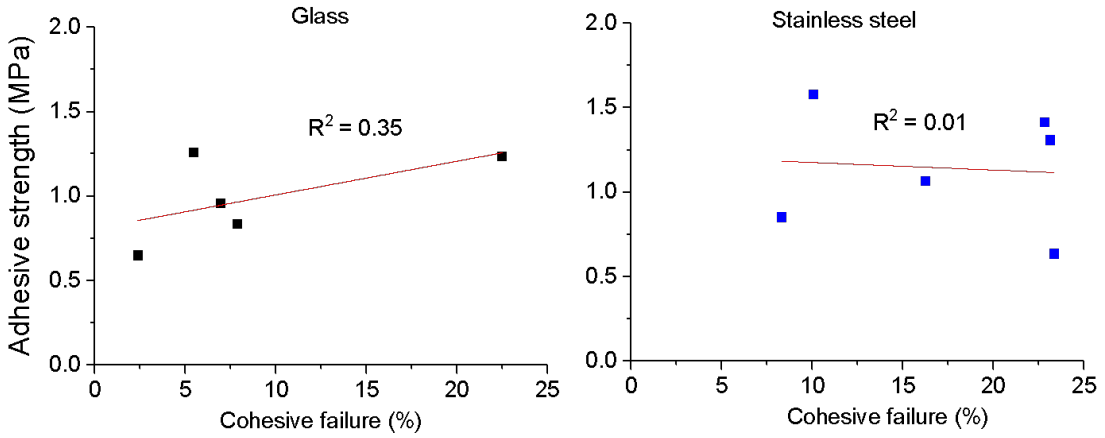

Figure 3.S5: A weak correlation was observed between shear strength and cohesive failure for glass (R^2= 0.35) and none for stainless steel surfaces (R^2= 0.01).

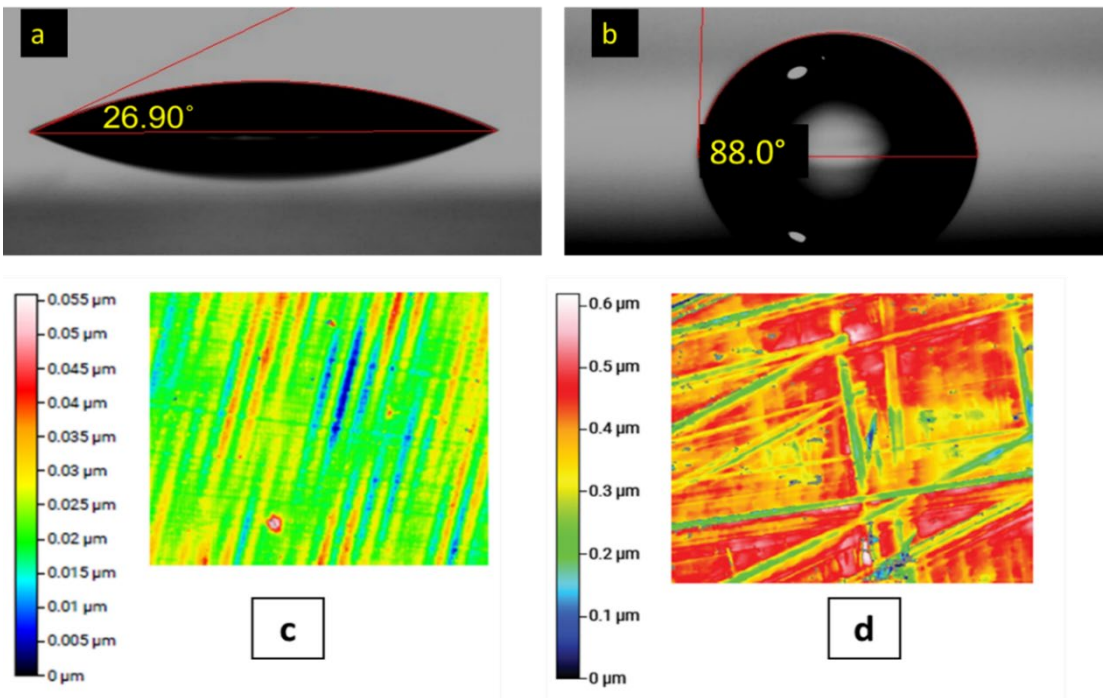

Figure 3.S6: Surface hydrophobicity and surface roughness of glass and stainless-steel surface surfaces. The contact angle of water (yellow text) on (a) glass is 26.9˚ and on (b) stainless steel is 88˚, indicating that the stainless-steel surface is slightly hydrophobic, and the glass surface is highly hydrophilic. Surface roughness of (c) glass and (d) stainless steel surface, color legends show an increasing surface roughness with a transition from blue to red. (c) Color maps of surface roughness show that the glass surface has a lower surface roughness (N=3, 0.046 ± 0.0023µm), than the (d) stainless steel surface (N=3, S_a 0.45 ± 0.0008µm).

Table 3.S1: The adhesive strength of microbially induced calcium carbonate adhesive (MICP) adhesives on glass and stainless-steel lap joints. The table shows calcium concentrations and microbial cell density tested for each biopolymer type. n = number of specimens yielding usable results (see text for details regarding inclusion criteria, *e.g.*, substrate failures).

Adhesive type		Biopolymer (g/l)	Calcium (M) +S. pasteurii OD600		Adhesive strength Mean ±SD (MPa)	
					Glass	Stainless steel
1	MICP soy protein	Soy protein isolate 100	0.165	0.4	0.45 ±0.1 (n=9) a	0.85 ±0.3 (n=6)
2				1.0	0.65 ±0.3 (n=9) a	1.1 ±0.6 (n=6)
3			0.33	0.4	1.26 ±0.2 (n=5) a	1.3 ±0.4 (n=6)
4				1.0	1.24 ±0.2 (n=4) a	1.6 ±0.5 (n=6)
5			0.5	0.4	0.84 ±0.2 (n=6) a	1.26 ±0.3 (n=6)
6				1.0	0.96 ±0.3 (n=4) a	0.64 ±0.3 (n=6)
7	No MICP (SP only)		DI water		0.22 ±0.01 (n=6)	0.25 ±0.1 (n=6)
8	MICP guar gum	Guar gum 7	0.165	0.4	0.17 ±0.06 (n=8) b	-
9				1.0	0.28 ±0.07 (n=10) b	-
10			0.33	0.4	0.20 ±0.05 (n=7) b	-
11				1.0	0.24 ±0.09 (n=9) b	-
12			0.5	0.4	0.06 ±0.02 (n=5) b	-
13				1.0	0.06 ±0.03 (n=6) b	-
14	No MICP (guar gum only)		DI water		0.11 ±0.01 (n=6) b	-

[a] n = 10 replicates were prepared for each group MICP soy protein glass lap joints. Some of the variability in the resulting adhesive strength data size for lap joints comes from the

exclusion of samples with failure of the glass lap joints (substrate failure) before the adhesive bond failure.

[b] n = 10 replicates were tested for each group in MICP guar gum glass lapjoints. The variability in adhesive strength data size comes from the exclusion of samples, for which the lap joints fell apart before and during loading into the test frame for shear, and tensile testing.

- (dashes) indicate that no data are available. The MICP- guar gum adhesives did not provide measurable adhesive strength on stainless steel lap joints for the curing and testing parameters used in this work.

Table 3.S2: The adhesive strength of EICP adhesives on glass lap joints. The table shows urease and calcium concentrations tested for each biopolymer type.

Adhesive type		Biopolymer g/l	Calcium (M) + Jack bean meal urease g/l		Adhesive strength Mean ±SD (MPa)
1	EICP soy protein	Soy protein isolate 100	0.165 M	2.5 (n=3)	1.2 ±0.3
2				5 (n=3)	1.1 ±0.2
3				10 (n=3)	1.0 ±0.3
4				15 (n=3)	0.71 ±0.3
5	EICP control		DI water (n=3)		0.22 ±0.01
6	EICP guar gum	Guar gum 7	0.165 M	2.5 (n=3)	0.1 ±0.025
7				5 (n=3)	0.17 ±0.06
8				10 (n=3)	0.28 ±0.04
9				15 (n=3)	0.25 ±0.05
10	EICP control		DI water (n=3)		0.11 ±0.01

Table 3.S3: Results of a three-factor ANOVA for MICP soy protein on glass lap joints (dependent variable: shear strength, independent variables: biopolymer, calcium concentrations (Ca), and bacterial cell density (OD)).

Analysis of Variance for response shear strength					
Source	DF	Adj SS	Adj MS	F-Value	P-Value
Ca	3	3.31	1.10	30.23	0.00
Biopolymer	1	7.78	7.78	213.54	0.00
Cell O.D.	1	0.04	0.04	0.96	0.33
Ca x Biopolymer	3	3.64	1.21	33.25	0.00
Ca x Cell OD	3	0.20	0.07	1.84	0.15
Biopolymer x Cell OD	1	0.00	0.00	0.01	0.94
Ca x Biopolymer x Cell OD	3	0.15	0.05	1.43	0.24
Error	101	3.68	0.04		
Total	116				

Table 3.S4: Results of a two-factor ANOVA to test the effect of calcium (Ca) and urease concentration on the adhesive strength of EICP adhesives on glass lap joints (dependent variable: shear strength, independent variables: calcium concentration, urease concentration).

Analysis of Variance for response shear strength					
Source	DF	Adj SS	Adj MS	F-Value	P-Value
Ca	2	0.027	0.014	26.34	0.00
Urease concentration	1	0.001	0.002	3.03	0.11
Ca x Urease Concentration	2	0.002	0.001	2.34	0.14
Error	11	0.005	0.000		
Total	16	0.040			

Table 3.S5: Results of a two-factor ANOVA to test the effect of biopolymer type and urease concentration on the adhesive strength of EICP adhesives on glass lap joints (dependent variable: shear strength, independent variables: biopolymer, urease concentration).

Analysis of Variance for log-transformed (ln) response shear strength					
Source	DF	Adj SS	Adj MS	F-Value	P-Value
Enzyme concentration	4	5.40	1.35	16.66	0.00
Biopolymer	1	16.46	16.46	202.90	0.00
Enzyme concentration x Biopolymer	4	3.18	0.79	9.79	0.00
Error	20	1.62	0.08		
Total	29	26.66			

Table 3.S6: Results of a three-factor ANOVA for MICP soy protein (dependent variable: shear strength, independent variables: surface type, calcium concentrations (Ca), and bacterial cell density (OD)).

Analysis of Variance for log-transformed (ln) response shear strength					
Source	DF	Adj SS	Adj MS	F-Value	P-Value
Ca	2	1.14	0.57	20.56	0
Surface	1	0.19	0.19	6.85	0.01
Cell OD	1	0.00	0.00	0.02	0.88
Ca x Surface	2	0.18	0.09	3.25	0.05
Ca x Cell OD	2	0.20	0.10	3.67	0.03
Cell OD x Surface	1	0.05	0.05	1.72	0.20
Ca x Cell OD x Surface	2	0.19	0.10	3.44	0.04
Error	61	1.69	0.03		
Total	72	4.09			

Table 3.S7: Results of a three-factor ANOVA for MICP soy protein (dependent variable: summative surface coverage, independent variables: surface type, calcium concentrations (Ca), and bacterial cell density (OD)).

Analysis of Variance for response summative surface coverage					
Analysis of Variance					
Source	DF	Adj SS	Adj MS	F-Value	P-Value
Ca	2	608.8	304.42	3.86	0.037
OD	1	110.6	110.61	1.4	0.25
Surface	1	961.9	961.95	12.19	0.002
Ca*OD	2	173.4	86.68	1.1	0.352
Ca*Surface	2	284.3	142.16	1.8	0.19
OD*Surface	1	264.8	264.78	3.36	0.081
Error	21	1656.6	78.89		
Lack-of-Fit	1	341.6	341.55	5.19	0.034

Table 3.S8: Surface coverage and failure data for MICP- soy protein adhesives on glass and stainless steel lap joints. The table shows the surface coverage of the adhesive and microbial cell density tested for each biopolymer type.

Biopolymer type	Calcium (M)	OD	Surface coverage (a+b) Mean ±SD	Failure analysis (Cohesive failure %)
MICP- soy protein glass (tested n=10)	0.165	0.4	84.77 ±8.12 (n=9)	(n=0)*
		1.0	96.63 ±7.73 (n=9)[a]	(n=5)* 2.37 ±3.95
	0.33	0.4	102.39 ±6.62 (n=5)[a]	(n=4)* 5.43 ±4.56
		1.0	122.50 ±19.70 (n=4) [a]	(n=2)* 22.47 ±5.59
	0.5	0.4	104.10 ±11.02 (n=6) [a]	(n=5)* 7.85 ±3.95
		1.0	106.92 ±5.87 (n=4) [a]	(n=3)* 6.92 ±4.56
MICP- soy protein stainless steel (tested n=6)	0.165	0.4	103.72 ±9.64 (n=3) [b]	(n=2) 8.30 ±5.91
		1.0	110.29 ±12.29 (n=3)	(n=2)16.24 ±5.91
	0.33	0.4	123.13 ±4.57 (n=3)	(n=3) 23.13 ±4.83
		1.0	110.04 ±11.55 (n=3)	(n=3) 10.04 ±4.83
	0.5	0.4	122.82 ±0.778 (n=3)	(n=3) 22.82 ±4.83
		1.0	110.30 ±24.4 (n=3)	(n=2) 23.33 ±5.91

[a]The variability in the number of replicates used in surface coverage analysis is due to the exclusion of lap joints where the failure occurred in the substrate instead of the bonded region, reducing the number of samples available for image analysis.

*Number of samples included in failure analysis is lower than the number of samples used for surface coverage analysis; only samples with a total surface coverage (a+b) greater than

100%, which indicated cohesive failure, were included in the failure analysis. Adhesive failure was back-calculated from the estimated percentage cohesive failure.

CHAPTER FOUR

IMPROVING THE WATER RESISTANCE AND DURABILITY OF BIOPOLYMER ADHESIVES THROUGH UREOLYSIS-INDUCED CALCIUM CARBONATE PRECIPITATION

Contribution of Authors and Co-Authors

Manuscript in Chapter 4

Author: Sobia Anjum

Contributions: Designed and conducted the experiments, analyzed data, and compiled the manuscript.

Co-Author: Kaylin Clark

Contributions: Supported experiment design and optimization, conducted experiments, reported outcomes and contributed to the writing of the manuscript.

Co-Author: Ethan Viles

Contributions: Conducted experiments and reported data outcomes.

Co-Author: Chelsea M. Heveran

Contributions: Supported experiment design, data analysis, writing, and review of the manuscript.

Co-Author: Robin Gerlach

Contributions: Supported experiment design, data analysis, writing, and review process.

Manuscript Information

Sobia Anjum, Kaylin Clark, Ethan Viles, Chelsea M. Heveran, and Robin Gerlach,

Status of Manuscript:

_X_ Prepared for submission to a peer-reviewed journal

____ Officially submitted to a peer-reviewed journal

____ Accepted by a peer-reviewed journal

____ Published in a peer-reviewed journal

Graphical Abstract

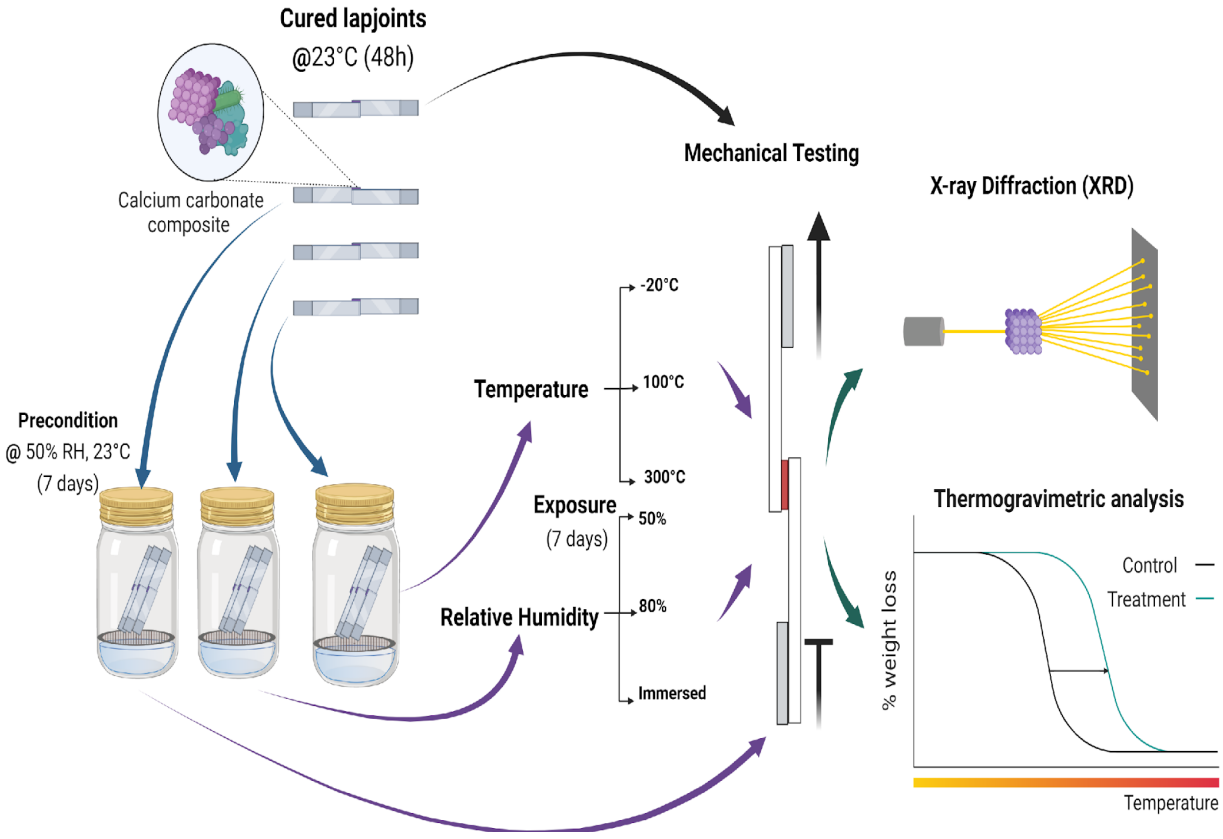

Figure 4. 1: The durability of the MICP-reinforced adhesives was tested after varying exposures for 7 days: immersion (for 24h and 7 days), at relative humidities (50 and 80% RH), and at temperatures (-20, 100, and 300˚C).

4.1 Abstract

Biobased adhesives are an integral part of the journey towards sustainably produced adhesives. Among biobased adhesives, many biopolymer-based adhesives have been developed as alternatives for petrochemical based adhesives However, the biopolymers often require structural modifications to improve their mechanical characteristics and adhesive performance. One such modification is the addition of mineral fillers as reinforcing agents, which has been

shown to improve the adhesive strength of the resulting composites. Among mineral filler-based adhesives, ureolytically induced calcium carbonate precipitation (biomineralization) in soy protein has been shown to deliver adhesive strength comparable to several commercial water-based adhesives. However, the durability of such adhesives upon environmental exposure (i.e., variations in temperature and humidity) remains unexplored. In this work, we demonstrate that the durability of soy protein adhesives reinforced via biomineral precipitation can be improved via biomineralization. The biomineralized soy protein adhesive has significantly higher water resistance than the soy protein alone. The type of biomineralization reaction affects the water resistance of mineral-reinforced biopolymer adhesives, and microbially induced ureolysis delivers a biomineral biopolymer adhesive with higher water resistance than enzymatic neurolysis. The microbially induced biomineral-biopolymer adhesives are also durable at freezing temperatures (T -20C) to moderate temperature and humidity (23˚C and 50% RH). Thermogravimetric and X-ray diffraction analysis show that the durability of the microbial biomineral-biopolymer adhesives at temperatures ≥100˚C and relative humidity ≥80% is potentially limited by the presence of highly soluble salts and low thermal stability of the organics (biopolymer) component of the adhesives. Determining the working range of the composite adhesives is critical for the scope of adhesives applications, and understanding the factors responsible for their performance is valuable for further research and development of biomineral based adhesives.

Keywords: polymer-composite adhesives, biopolymer-biomineral composites, biomineralization, durability, water resistance, water sensitivity, thermal stability.

4.2 Introduction

The development of biobased adhesives is a strategy to decrease the environmental and human health risks associated with synthetic polymers in the adhesives and packaging industry (Höfer et al., 2019; Packham, 2009). Most polymers used in adhesive and packaging applications are derived from petrochemical feedstock and involve the use of high volatile organic compound (VOC) solvents (Li et al., 2021; Packham, 2009; Tolls et al., 2016). To minimize the environmental impacts of petrochemical-based polymers, greener synthesis methods for producing synthetic polymers, and their complete or partial replacement with biopolymers are being explored (Dinte & Sylvester, 2018; Heinrich, 2019; Lamaming et al., 2021; Patel et al., 2013). While protein-based adhesives such as soy protein have gained significant attention with an increasing demand for sustainable adhesives, the limited water resistance of such adhesives significantly limits their broader applicability (Oni et al., 2023).

To improve the water resistance of protein and soy-based adhesives, several methods have been employed. Most common modifications include crosslinking modifications, either by synthetic or biobased crosslinking agents, and protein denaturation by thermal and chemical treatments (Bukartyk et al., 2022; Oni et al., 2023). More recently modified fillers have emerged as a solution for low mechanical performance and water resistance of soy-based adhesives. The modified mineral fillers-based soy- nanocomposite adhesives are developed by combining soy protein denaturation and crosslinking treatments with mineral fillers to achieve high adhesive strength and water resistance as biobased adhesives (Chen et al., 2022; Helanto et al., 2021, 2022; Post et al., 2021; Qi et al., 2016; Sun et al., 2021). These modifications in soy-based adhesives are highly beneficial for their performance, yet, the crosslinking reactions involve the

use of potentially toxic and hazardous reagents thereby lowering the sustainability of the adhesives (Raydan et al., 2021).

Recently (Chapter 3 of this dissertation) our group has shown that biomineralization via ureolytically induced precipitation of calcium carbonate precipitation can significantly enhance the adhesive strength of soy protein-based and guar gum-based biopolymer mineral adhesives. These ureolytically induced calcium carbonate precipitate (UICP)-reinforced adhesives can be produced at ambient temperatures in the biopolymers in-situ, do not require additional crosslinking reactions, and are highly customizable. The ureolysis can be carried out by multiple urease enzyme sources and optimized using several control parameters (e.g., calcium and enzyme concentrations and type of biopolymer additive).

The goal of this work was to determine the durability characteristics of these biomineral-biopolymer adhesives. To determine the durability characteristics of UICP-reinforced adhesives we assess 1) the water resistance of microbially and enzymatically induced biomineral-reinforced biopolymer adhesives upon immersion, 2) the durability of the microbial biomineral-biopolymer adhesives at varying humidity and temperature exposures, and 3) the structural and compositional changes in microbial biomineral-biopolymer adhesives following the humidity and temperature exposures. These data are needed for testing whether biomineral-biopolymer adhesives improve upon the durability characteristics of biopolymer adhesives as well as identifying key areas of performance improvements necessary to advance the utility of biobased adhesives.

4.3 Materials and Methods

Jack bean powder and BD Difco™ Nutrient Broth (NB) were purchased from Sigma Aldrich and Fisher Scientific, respectively. Soy protein isolate was purchased from MP Biomedicals (Fisher Scientific). All solutions were prepared in deionized (DI) water with an electrical resistivity of ≥ 18.2 MΩ.

4.3.1 Microbially Induced Calcium Carbonate Precipitation Reinforced Adhesive

Microbially induced calcium carbonate precipitation (MICP) was induced by mixing a culture of the bacterium *Sporosarcina pasteurii* with a mineralization solution. Bacterial cultures were prepared by inoculating 100 ml of filter-sterilized growth medium (0.33M urea, 0.18M NH_4Cl, 3g/l Nutrient broth) with 1ml of a thawed *S. pasteurii* (ATCC11859) stock culture, which was incubated overnight at 30 ˚C and 150 rpm. One milliliter of the overnight culture was transferred into 100 ml of fresh growth medium and incubated again overnight at 30 ˚C at 150 rpm. This bacterial culture was harvested after 20-22 hours when achieving an optical density of 0.4 ± 0.05 (mean ± SD) measured at 600nm (OD_{600}). Bacterial cultures with an OD_{600} of 1.0 were prepared by concentrating the overnight culture through centrifugation at 5000 x g for 5 minutes at 21˚C; the resulting cell pellet was harvested and resuspended in a sterile growth medium to reach an OD of 1.0 ± 0.05. The optical densities were measured in flat bottom 96-well plates (Polystyrene, Greiner Bio-One) using a Synergy HT Spectrophotometer (Biotek); at 200µl of liquid, the path length was estimated to be 5mm. Absorbance values of 200 µl of sterile growth medium in a 96 well plate well was subtracted from sample readings to remove the OD contribution of the growth medium and the plate itself. The mineralization solution had the same

composition as the growth medium but additionally contained calcium chloride (0.33M). The microbial culture and mineralization solutions were mixed in a 1:1 ratio to achieve a calcium concentration of 0.165M. The MICP-reinforced biopolymer adhesive was prepared by adding soy protein isolate (SP) to the formulation at 10% (w/v).

4.3.2 Enzymatically Induced Calcium Carbonate Precipitation Reinforced Adhesive

Enzymatically induced calcium carbonate precipitation (EICP) was induced by mixing a solution of jack bean meal urease with a mineralization solution. Jack bean meal (JBM) extracts were prepared by suspending 5 g/l of fine powdered JBM in deionized water for 4 hours. Before use, the suspensions were filtered through 0.22 μm pore size bottle top filters (Nalgene Rapid-Flow Filters, Thermo Scientific). Mineralization solutions were prepared with both urea and calcium chloride at 0.33M. JBM extract and mineralization solution were mixed in a 1:1 ratio to achieve a calcium concentration of 0.165M. The EICP-reinforced biopolymer adhesive was prepared by adding soy protein isolate (SP) to the formulation at 10% (w/v).

4.3.3. Lapjoint Preparation and Adhesive Strength Testing

Borosilicate glass adherends (25mm x 75mm) were cleaned with deionized water and 70% ethanol. The MICP and EICP-reinforced biopolymer adhesives were vortexed for 5s, and 100μl of an adhesive was applied to 12.5mm x 25mm edge of one adherend placed flat on a bench top. The second adherend (*i.e.*, a second slide) was placed on top to make a 12.5mm x 25mm overlap area (Figure 1, ASTM method D1002-10). No additional external pressure was applied. The sample was allowed to cure for 48 hours at 23 ˚C ±2 ˚C. The adhesive strength of the adhesives was tested in tension at 0.01 mm/sec displacement rate to failure (Instron 3340). The maximum load (N) at

the point of bond failure divided by the overlap area (322 mm^2) was used to calculate the adhesive strength of the sample in MPa.

4.3.4 Water Resistance and Durability Testing

The water resistance of the MICP and EICP-reinforced biopolymer adhesives was compared in a 24-hour immersion test. Cured MICP and EICP adhesive lapjoints were immersed in DI water for 24 hours. The lapjoint joints that remained intact post-immersion were tested for their wet adhesive strength.

The durability of MICP-reinforced adhesives at various humidity regimes was tested at 7-day exposures to 50% RH, 80% RH, and immersion. The humidity chambers were prepared in 64-ounce wide-mouth mason jars with magnesium nitrate and potassium chloride salt slurries to maintain 50% and 80% humidity, respectively, at 23 ± 1˚C. Samples were preconditioned at 50% RH at 23 ± 1˚C for 7 days. The lapjoints were then transferred to 50% RH and 80% RH humidity chambers for 7 additional days. For a 7-day immersion exposure, lapjoints were immersed in DI water in a closed airtight container. Humidity in the mason jars was monitored using Elitech GSP-6 humidity probes.

The durability of the adhesives was tested with temperature exposures at -20˚C, 100˚C and 300˚C for 7 days. The preconditioned lapjoints (50% RH at 23 ± 1˚C for 7 days) were placed at -20 ± 1˚C into a Whynter (FM65-G) Portable Freezer, 100˚C in a Gravity Convection Oven (Quincy Lab, inc. 10GCE-LT), and 300 ± 5˚C in a Muffle Furnace (Fisher Scientific Isotemp 650 Series Model 58). To prevent sudden temperature changes in contact with the incubator, oven, and freezer surfaces, the samples were placed in mesh holders inside mason jars. The oven

and furnace temperatures were tracked using Infrared Thermometer (Etekcity Lasergrip 1080), and the freezer temperatures were logged using a GSP-6 temperature probe.

Table 4.1: Test parameters for temperature and humidity exposure conditions (ASTM D1151-00).

Samples	Temperature (˚C)	Time (days)	Moisture Conditions
Cured (C)	23	2	Uncontrolled humidity
Preconditioned (PC)	23	C + 7	50% RH
Temperature exposures	-20	PC +7	Uncontrolled humidity
	100	PC +7	Uncontrolled humidity
	300	PC +7	Uncontrolled humidity
Humidity exposures	23	PC +7	50% RH
	23	PC +7	80% RH
	23	PC +7	Immersed in water

4.3.5 Statistical Analysis

A two-way ANOVA was used to test the effects of bacterial cell density, immersion, and their interactions on the adhesive strength of MICP-reinforced adhesives. One-way ANOVA tested the effects of relative humidity and temperature on the adhesive strength of MICP adhesives. Dunnett's test was used to determine the pairwise significance of differences in means after humidity and temperature exposures as compared to preconditioned lapjoints. The critical α was set a prior at 0.05.

4.3.6 Mineral and Organic Phase Characterization

The mineral phase composition of the adhesives was analyzed by X-ray diffraction (XRD). The XRD spectra were obtained at 2θ from 5˚-70˚ using a Cu-Kα X-ray source in a Bruker D8 Advance X-ray diffractometer. The crystalline phases were identified using the Jade software.

Thermogravimetric analysis was used to assess the variations in organic and mineral content of the adhesives before and after the humidity and temperature exposures. The thermal decomposition profiles of the adhesives were tracked by their respective rates of weight loss between 50 to 800 ˚C at a heating rate of 10 ˚C/min in a nitrogen (N_2) atmosphere. The thermal weight loss profiles of individual components, *i.e.,* soy protein isolate, ammonium chloride, and calcium carbonate, were acquired separately for reference.

4.4 Results

4.4.1 MICP-Reinforced Soy Protein Adhesives have Higher Water Resistance than Non-Mineralized Biopolymer and EICP-Reinforced Soy Protein Adhesives

This study demonstrates that MICP reinforced adhesives had higher water resistance than non-mineralized biopolymer and EICP reinforced adhesives lapjoints. Both non-mineralized SP and EICP reinforced adhesives deteriorated during immersion in water at 23± 0.5˚C for 24 hours (Figure 4.2) indicating that the effectiveness of water resistance depended on the biomineralization method. Both non-mineralized SP and EICP-reinforced adhesives deteriorated after 24 hours of immersion in water, indicating that the enzymatically induced calcium carbonate precipitation does not confer any noticeable water resistance to the soy protein adhesive.

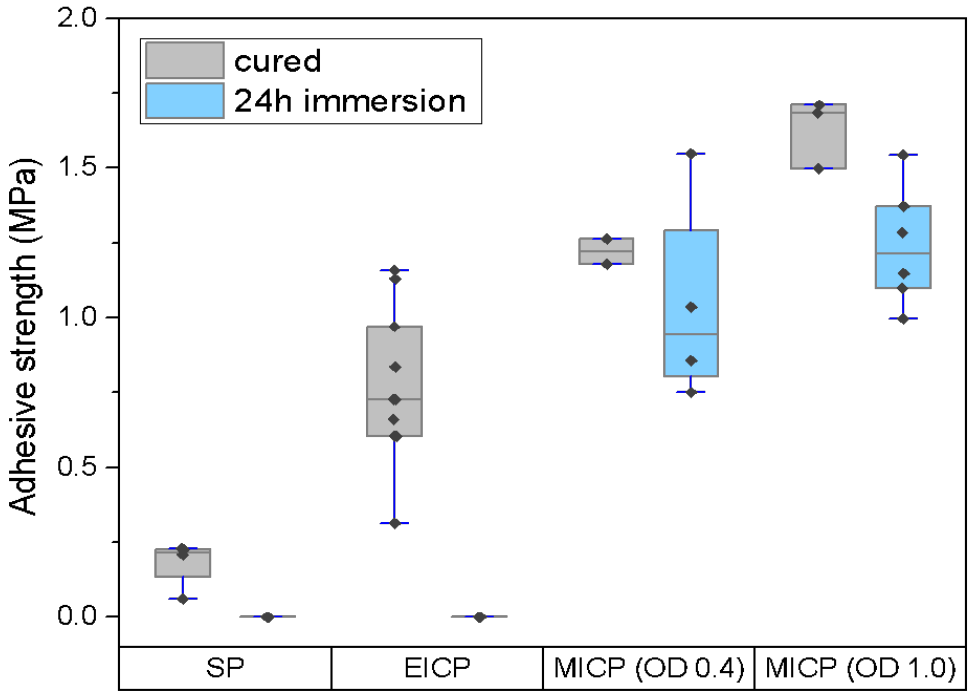

Figure 4. 2: The adhesive strength of non-mineralized biopolymer (SP), enzymatically and microbially induced calcium carbonate reinforced adhesives, before and after 24 hours of immersion. The SP and EICP-reinforced adhesives lapjoints deteriorate after immersion whereas the MICP-reinforced adhesives prepared with low (OD 0.4) and high (OD 1.0) cell density retain 75 to 81% of their adhesive strength. The box plots show data for n=3 each (no exposure), n=4 low OD immersed, and n=6 high OD immersed replicates. The upper and lower bounds of the boxplots represent the 25th and 75th percentiles, and the whiskers indicate the minimum and maximum values for data points (♦), The median is indicated by a horizontal straight line.

The MICP lapjoints retained 75-81% of their adhesive strength after immersion as compared to dry samples (before vs. after immersion adhesive strength p= 0.053, Figure 4.2). The dry and wet adhesive strength of MICP adhesives produced with higher cell density (OD 1.0) were 1.63 MPa and 1.24 MPa, respectively, compared to 1.22 MPa and 1.04 MPa, respectively for MICP adhesives produced with lower cell density (OD 0.4). At OD 0.4, two of the six MICP lapjoints experienced bond failure while they were being loading into the test frame, whereas no OD 1.0 MICP lapjoints experienced bond failure during loading. The fragility of two of the six MICP OD 0.4 lapjoints indicates variability in their water resistance. There was

no significant Biomineralization in the presence of bacterial cells and their extracellular products has been shown to protect organic matter in soils against environmental factors (Kleber et al., 2005). During in-vitro biomineralization reactions, ureolytically induced calcium carbonate precipitation in the presence of *S. pasteurii* cells has been shown to produce calcium carbonate precipitates lower the dissolution rates than abiotic calcium carbonate precipitates (Mitchell & Grant Ferris, 2006). The synergistic interactions between bacterial cells, cell products and the mineral content of the MICP adhesives may be responsible for their improved performance upon immersion for 24 hours.

MICP adhesives show higher retention in adhesive strength after water exposure than most of the emerging biopolymer-mineral adhesives reported in the literature. The MICP adhesives with low OD (OD 0.4) retained up to 81% of its adhesive strength after 24 hours of immersion in water at 23˚C. The water resistance shows their potential suitability for indoor applications where a short water exposure, e.g., a water spill does not result in failure of the bonded joints. Mineral filler-based soy flour (SF) adhesives in other work made mineral fillers like montmorillonite have been shown to retain ~45 to 60% of their adhesive strength on plywood after three hours of immersion in water at 63˚C (Sun et al., 2021). However, the biopolymer-mineral adhesive films made with nanoparticle fillers retain only 3-4% of the adhesive strength on aluminum substrates after 24 hours of immersion at 25˚C (Li et al., 2018). in comparison.

4.4.2 The Adhesive Strength Of MICP-Reinforced Adhesive is Maintained at Low to Ambient Relative Humidity Exposures

Preconditioning the MICP lapjoints (at 50%RH) prior to humidity exposures, did not significantly affect their adhesive strength compared to the cured samples (1.72 ± 0.23 vs. 1.45 ± 0.36, p= 0.37, Figure 4.3). Subsequent exposure to 50% RH humidity for 7 additional days, did not change the adhesive strength of the adhesives post exposures (p>0.05, Table 4.S4). The exposure to 80% RH and immersion significantly decreased the adhesive strength compared to the preconditioned lapjoints (95% decrease, p=0.001). The MICP adhesives had high water resistance after 24h immersion (section 4.4.1) but after 7 days of immersion, most of the MICP lapjoints deteriorated. The immersed lapjoints that did not deteriorate retained only 3-4% of their adhesive strength compared to the preconditioned samples (p<0.001).

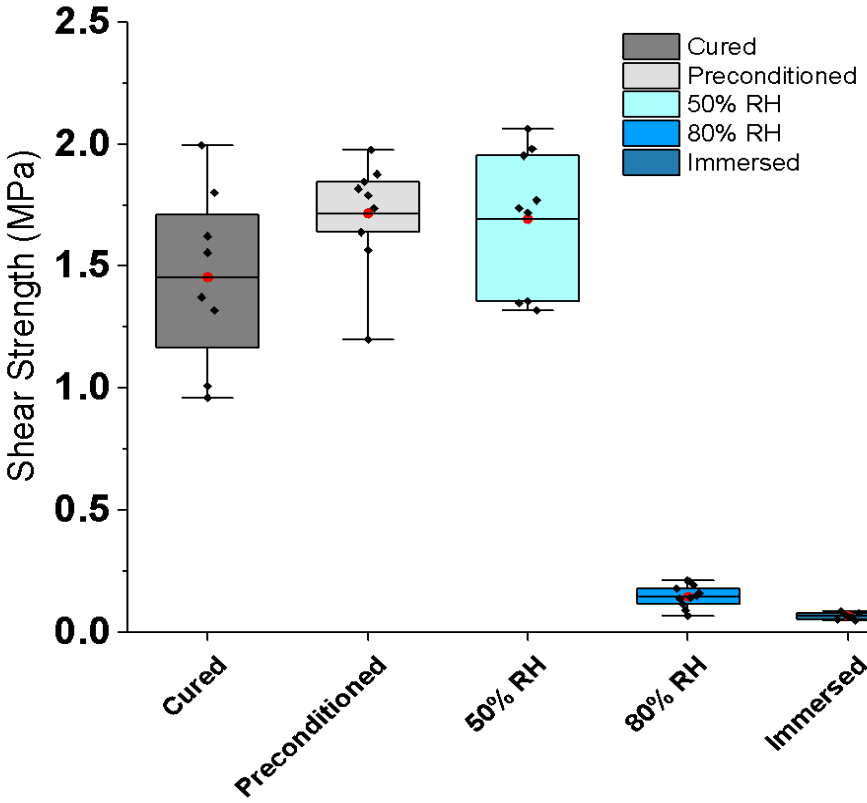

Figure 4. 3: Adhesive strength of MICP adhesives after exposure to varying relative humidity regimes or after immersion in water for 7 days. The boxplots contain datapoints for n=7 to n=10 replicates. The variability in sample sizes occurs due to substrate failure during strength testing (50% RH) and bond failure before testing (80% RH and immersion). The upper and lower bounds of the boxplot represent the 25th and 75th percentiles, and the whiskers indicate the minimum and maximum values for data points (♦), The median is indicated by a horizontal straight line, and the mean is represented by (●).

4.4.3 The MICP-Reinforced Adhesive is Durable at Below Freezing Temperatures

Freezing MICP-reinforced adhesives at -20˚C for 7 days and thawing them before testing did not affect their adhesive strength, while exposure to higher temperature (100 and 300 ˚C) decreased the adhesive strength of MICP-reinforced adhesives (Figure 4.4). The MICP adhesives retained their adhesive strength after 7-day exposure to -20˚C as compared to the preconditioned samples ($p > 0.05$, Table 4.S6). In contrast, the adhesive strength of MICP adhesives might have decreased by 45% upon exposure to 100˚C ($p=0.005$). However, five of the ten replicates exposed to 100˚C experienced a failure in the glass substrate instead of the bonded region during the lap shear tests, thus having a potentially having greater adhesive strength. While the remaining five lapjoints failed in the bonded region and showed a 45% decrease in adhesive strength as compared to the preconditioned lapjoints. The decrease in the adhesive strength of the soy-based adhesive after high-temperature exposures (100-150˚C) differs from previous reports, which report an increase in adhesive strength after heat treatments (Chen et al., 2022; Jensen et al., 2015; Lamaming et al., 2021). Exposure of the adhesives to 300˚C resulted in a 95% loss in the adhesive strength of the adhesives ($p<0.001$, Table 4.S6), and 3 of 10 lapjoints deteriorated before testing. At the curing conditions investigated here, the MICP-reinforced adhesives are highly suitable for below-freezing temperature applications, whereas the adhesives need further optimizations for reliable performance at 100˚C. The performance of the adhesives is potentially

limited by thermal degradation of soy protein at higher temperatures (>200˚C) (Chen et al., 2022; Lamaming et al., 2021).

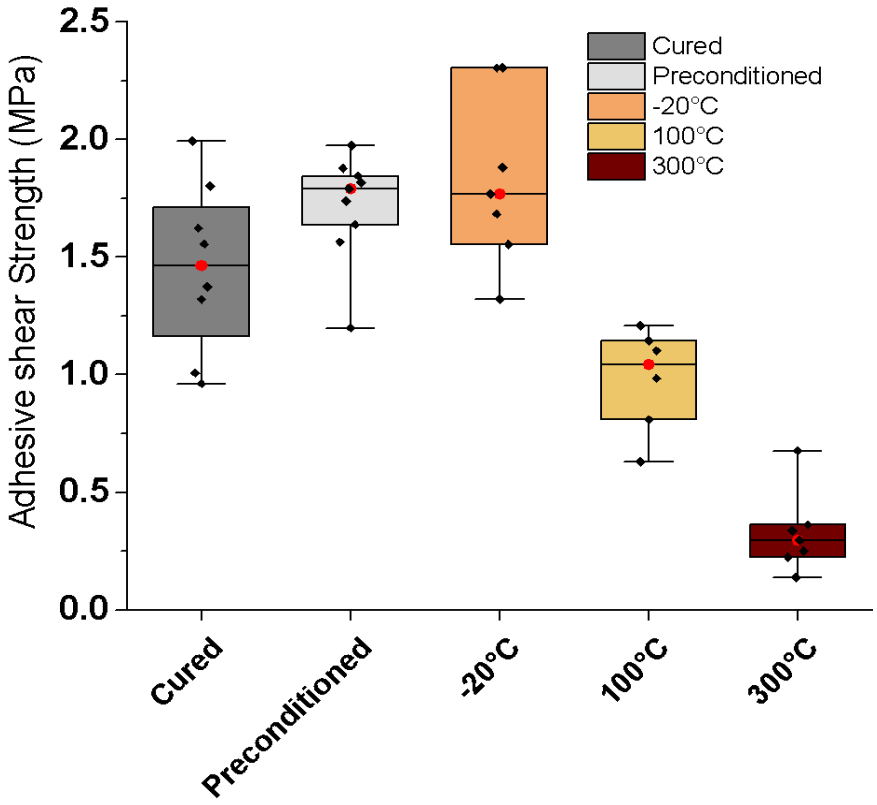

Figure 4. 4: Adhesive strength of MICP adhesives pre- (cured and preconditioned) and post-temperature exposure for 7 days. The boxplots contain n=6 to n=10 replicates. The variability in sample sizes occurs due to substrate failure during testing (-20 ˚C and 100 ˚C) or bond failure before testing (300 ˚C). The upper and lower bounds of the boxplot represent the 25th and 75th percentiles, and the whiskers indicate the minimum and maximum values for data points (♦), The median is indicated by a horizontal straight line, and the mean is represented by (●).

4.4.4 The Organic Components of MICP-reinforced adhesives are Susceptible to Immersion

The MICP adhesives before and after the 7-day humidity exposures had similar mineralogy as the cured and preconditioned samples. Calcium carbonate, sodium chloride, and ammonium chloride were detected in all adhesives (Figure 4.5). Calcium carbonate was present as calcite in cured samples and preconditioned samples, but after exposure to 50% RH and 80%

RH, vaterite peaks were detected as well. An absence of vaterite in cured and preconditioned samples, but its noticeable presence in MICPs after exposure to 50% RH and 80% RH, indicated the potential occurrence of dissolution-precipitation kinetics at moderate to high humidities resulting in the formation of vaterite.

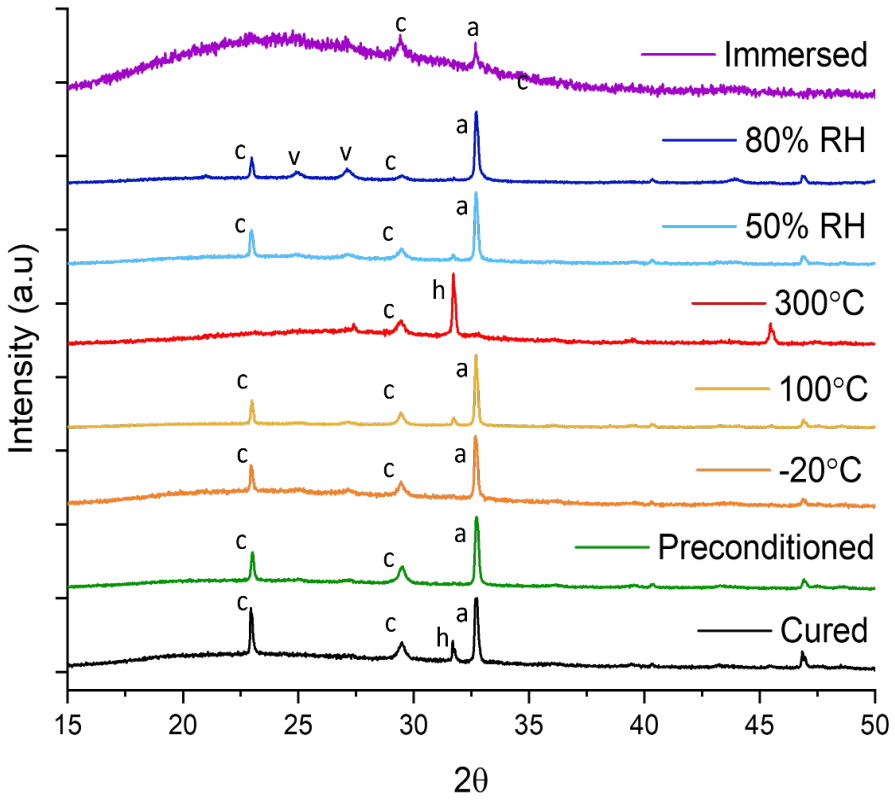

Figure 4. 5: X-ray diffraction spectra of MICP adhesives pre- and post-humidity and temperature exposures. The crystalline phases detected in MICP adhesives were ammonium chloride (a), calcite (c), halite (h), and vaterite (v).

To determine the relative mineral and organic content of the MICPs before and after humidity exposures, their thermal degradation profiles were analyzed (Figure 4.6). Preliminary tests showed that, the soy protein volatilizes between 200-550˚C, and calcium carbonate between 600-750˚C (Figure 4.S1). The thermal degradation of ammonium chloride and soy protein

overlaps between 250-325˚C. The weight loss between 50-100˚C was assigned to the loss of adsorbed water, and the weight loss between 100-250˚C was associated with biomass and low volatile organic compounds.

The weight loss profiles of the MICPs after 50 and 80% RH exposures were similar to the preconditioned samples (Figure 4.6 A&C). However, the weight loss profile of the 7-day immersion samples was different from the preconditioned sample. This loss in adhesive during immersion was attributable to the absence of biomass and low VOCs peak (100-250˚C), suggesting their solubilization upon immersion (Figure 4.6C). Additionally, the peak height in the 250-550˚C region was smaller for immersed samples than for the preconditioned samples, suggesting the solubilization of ammonium chloride and possibly even soy protein (Figure 4.6C). The weight loss between 600˚C-750˚C confirmed the presence of calcium carbonate in the immersed adhesives.

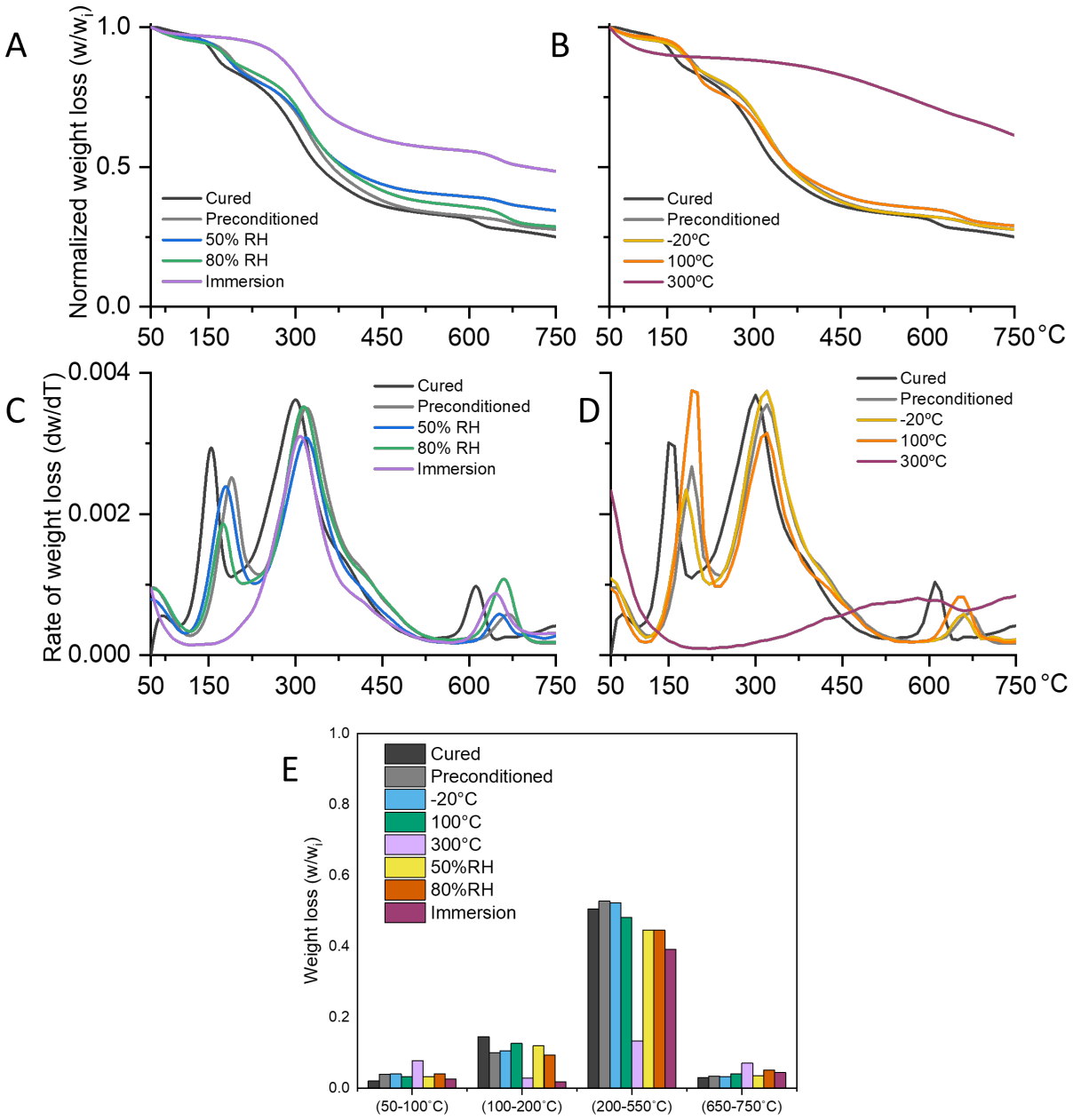

Figure 4. 6: The thermogravimetric profiles of the MICPs before and after humidity. (A, C) and (B, D) temperature exposures were developed by tracking weight loss (normalized to initial weight, w/w_i) and rate of weight loss ($\Delta(w/w_i)/\Delta T$) from 50 to 750˚C, at 10˚C/min heating rate. (E) The weight loss from 50 to 100˚C, 100 to 200˚C, 200 to 550 ˚C, and 650 to 750˚C associated with water loss, low MW organics, soy protein, and calcium carbonate, show the variations in the mineral and organic content of the adhesives after humidity and temperature exposures.

4.4.5 Thermal Degradation of Organics may be a Limiting Factor for MICP Adhesives Durability

The MICP-reinforced adhesives before and after the 7-day temperature exposures had similar mineralogy as preconditioned samples, except after the 300˚C exposure (Figure 4.5). The calcium carbonate was present as calcite in all temperature exposure samples, as well as in cured and preconditioned samples. No ammonium chloride was detected after exposure to 300˚C, indicating that the ammonium chloride may have sublimated at prolonged exposure to 300˚C.

There were no differences in the weight loss profiles of the samples exposed to -20 or 100˚C exposure samples compared to the preconditioned samples (Figure 4.6 B&D). At 300˚C, no distinct peaks were detectable in the derivative plot (Figure 4.6 D), a d weight loss of only ~43 % was observed for 300˚C exposure samples as compared to ~75% weight loss in preconditioned samples. The lower weight loss in 300˚C samples during thermogravimetric samples may have occurred due to the degradation of thermally labile organic components and the loss if ammonium chloride during 7-day exposure at 300˚C. A significant amount of the weight loss in the 300˚C exposure samples occurred between 600 and 750˚C, indicating a prevalence of calcium carbonate.

4.4.6 Implications of Mineral and Organic Content for the Durability of MICP adhesives

There are multiple possible reasons explaining the decrease in the adhesive strength of MICPs with water immersion and high humidity. One of these is that the MICPs contain substantial quantities of highly soluble salts, such as ammonium chloride and sodium chloride as indicated by XRD data (Figure 4.4). These salts may contribute to a high capacity for water vapor retention. Nevertheless, MICPs have higher water resistance than non-mineralized

biopolymers after 24 hours of immersion. Moreover, the adhesive strength retained by MICPs after water immersion is much greater (~2x) than a range of soy adhesives made by crosslinking soy with kaolin, clay, and calcium carbonate minerals (Sun et al., 2021). The durability of MICP adhesives to water exposure could further improve by lowering the presence of high solubility salts in the formulations. Lowering the water retention potential of the adhesives can potentially further improve their prospects for long-term high humidity exposure applications, e.g., as outdoor adhesives in humid climates.

The high organic content of the MICPs may also influence the degradation characteristics of these materials with immersion and humidity (Figure 4.5). The role of microbial biomass in the adhesive adhesives is evident by a significant (75-81%) retention of the adhesive strength in MICP-reinforced adhesives, as compared to EICP-reinforced adhesives that deteriorate after 24 hours of immersion. Yet after 7 days of immersion, the MICPs deteriorate as well. The thermogravimetric analysis shows the loss of biomass and soy protein in the 7-day immersion samples. This loss of organics at humidity and temperature extremes and the corresponding loss in the adhesive strength in adhesives highlight the significance of the organic components for the performance of the adhesive adhesives.

Some of the ways to counter the solubilization of organics and reduce the water susceptibility of the adhesives might be to protect the functional groups by the crosslinking of the biopolymers, as demonstrated for other biopolymer-mineral adhesives (Azeredo & Waldron, 2016; Jayachandran et al., 2022; Kim et al., 2021). Cross-linking between biopolymer and bacterial cells can serve the dual function of protecting the water susceptible groups and increasing the cohesive strength (stiffness) of the adhesives (Oni et al., 2023). The thermal stability of the adhesives at 300˚C remains limited by the thermal degradation of the soy protein,

and the stability of the MICP adhesives beyond 100˚C is out of the scope of their intended indoor and outdoor applications.

4.5 Conclusions

This study demonstrates that microbially induced calcium carbonate adhesives produced in the presence of soy protein (MICP) have a higher water resistance than non-biomineralized soy protein specimens at 24-hour immersion exposures. The water resistance of MICP-reinforced adhesives is also higher than the EICP-reinforced adhesives at 24-hour immersion exposures. The durability of MICP at 7-day exposures is, however, limited to low and moderate humidity environments. The low water resistance of MICP at 7-day exposures can be attributed to the presence of hydrophilic salts and water-soluble soy protein. The adhesive strength of the MICP is stable at sub-freezing temperatures. The thermal stability of the adhesive at high temperatures is also strongly limited by the thermal decomposition of the biopolymer and other organics. The MICPs are durable at sub-freezing temperatures and in indoor environments, which ideally have a relative humidity (RH) between 30 and 50%. This work offers potential pathways for further improvements in the performance and durability of biomineral-biopolymer adhesives. Overall, biomineralization offers significant improvements in the water resistance of biopolymer adhesives and may increase the range of applications where biobased adhesives can be used.

4.6 Acknowledgments

This research was made possible by the Center for Biofilm Engineering, Department of Chemical and Biological Engineering, Mechanical & Industrial Engineering, and the Norm Asbjornson College of Engineering at Montana State University. This material is based upon

work supported by the National Science Foundation under Grant #s 1736255 (BuG ReMeDEE) and 2036867 (BRICS). Part of this work was performed at the Montana Nanotechnology Facility, an NNCI facility supported by the National Science Foundation (NSF) under Grant ECCS-1542210. Partial funding was supplied by the Undergraduate Scholars Program at Montana State University. Mechanical testing was completed in Dr. Stephen Sofie's lab at MSU. Graphics were created with BioRender.com.

4.7 Supplemental Information

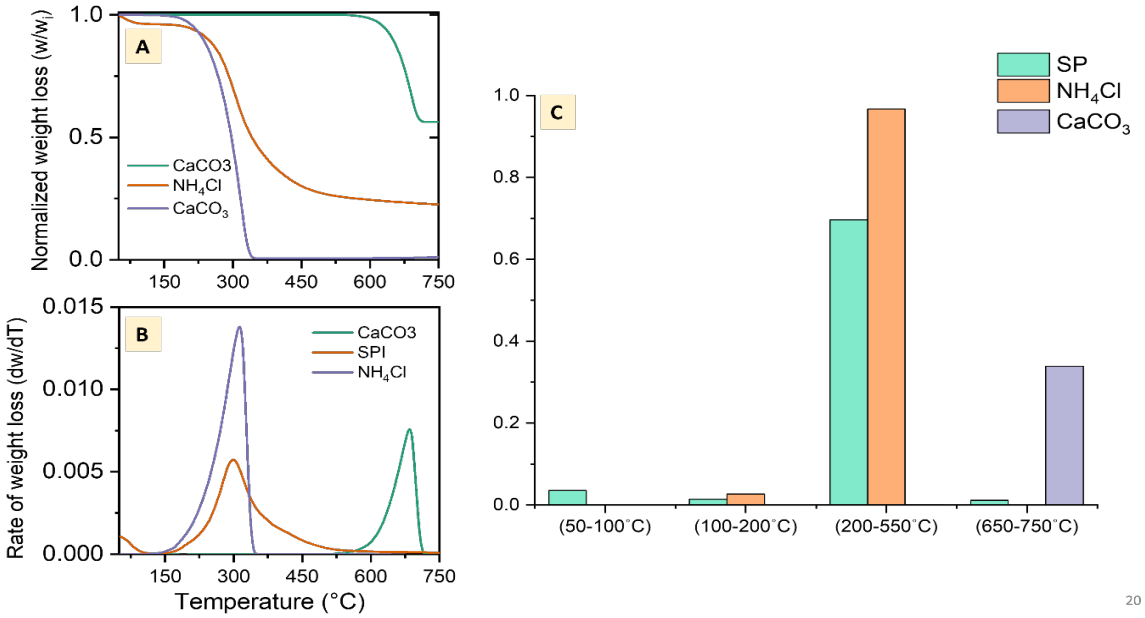

Figure 4.S1: Weight loss, derivative of weight loss and normalized weight loss of soy protein isolate, ammonium chloride and calcite during thermogravimetric analysis at 10˚C/min between 50 to 800˚C.

Table 4.S1: Results of a two-factor ANOVA to test the effect of cell density and immersion on the adhesive strength of MICP-reinforced adhesives.

Analysis of Variance for Transformed Response (λ=2)					
Source	DF	Adj SS	Adj MS	F-Value	P-Value
Immersion	1	1.5653	1.5653	4.70	0.053
Cell density	1	1.9386	1.9386	5.83	0.034
Immersion*Cell density	1	0.5055	0.5055	1.52	0.243
Error	11	3.6600	0.3327		
Total	14	7.6895			

Table 4.S2: Descriptive statistics of the wet and dry adhesive strength of MICP reinforced adhesives before and after immersion in water, respectively.

Cell density	Immersion	Total Count	Mean	SE Mean	St Dev	Variance	Median
OD 1.0	Dry	3	1.6307	0.0667	0.1156	0.0134	1.6838
	Wet	6	1.2401	0.0815	0.1998	0.0399	1.2156
Variable	Exposure	Total Count	Mean	SE Mean	St Dev	Variance	Median
OD 0.4	Dry	2	1.2209	0.0417	0.0590	0.0035	1.2209
	Wet	6	1.047	0.177	0.354	0.125	0.945

Table 4.2: Results of a two factor ANOVA to test the effect of varying humidities on the (log transformed) adhesive strength of MICP-reinforced adhesives.

Source	DF	Adj SS	Adj MS			F-Value	P-Value
Humidity exposures	4	80.345	20.0863			327.67	0.000
Error	37	2.268	0.0613				
Total	41	82.613					

Table 4.3: Paired Dunnett's comparisons for the adhesive strength of the MICP-reinforced adhesive lapjoints after relative humidity exposures as compared to preconditioned lapjoints.

Difference of Sample Levels	Difference of Means	SE of Difference	Simultaneous 95% CI	T-Value	Adjusted P-Value
50 RH – PC	0.009	0.120	(-0.299, 0.317)	0.08	1.000
80 RH – PC	-2.517	0.114	(-2.808, -2.226)	-22.13	0.000
Cured – PC	-0.185	0.120	(-0.493, 0.123)	-1.54	0.367
Immersion - PC	-3.274	0.125	(-3.593, -2.955)	-26.24	0.000

Individual confidence level = 98.52%

Table 4.4: Results of a one-factor ANOVA to test the effect of varying temperatures on the adhesive strength of MICP-reinforced adhesives.

Source	DF	Adj SS	Adj MS	F-Value	P-Value
Temperature exposures	4	10.657	2.66430	31.10	0.000
Error	30	2.570	0.08567		
Total	34	13.227			

Table 4.5: Paired Dunnett's comparisons for the adhesive strength of the MICP-reinforced adhesive lapjoints after varying temperature exposures as compared to preconditioned lapjoints.

Difference of Sample Levels	Difference of Means	SE of Difference	Simultaneous 95% CI	T-Value	Adjusted P-Value
100˚C – PC	-0.582	0.165	(-1.011, -0.152)	-3.52	0.005
300˚C – PC	-1.755	0.149	(-2.143, -1.367)	-11.76	0.000
Cured – PC	-0.185	0.144	(-0.559, 0.189)	-1.28	0.542
Neg 20˚C – PC	0.060	0.156	(-0.346, 0.465)	0.38	0.988

CHAPTER FIVE

BOVINE SERUM ALBUMIN ALTERS THE NANOMECHANICAL PROPERTIES OF UREOLYTICALLY INDUCED CALCIUM CARBONATE PRECIPITATES

Contribution of Authors and Co-Authors

Manuscript in Chapter 5

Author: Sobia Anjum

Contributions: Designed and conducted the experiments, analyzed data, and compiled the manuscript.

Co-Author: Kaylin Clark

Contributions: Prepared samples for nanoindentation and AFM testing.

Co-Author: Amir Darabi

Contributions: Conducted AFM testing, prepared figures and supported data analysis.

Co-Author: Lewis Cox

Contributions: Supported experiment design and data analysis for AFM experiments.

Co-Author: Robin Gerlach

Contributions: Supported experiment design, data analysis, writing, and review process.

Co-Author: Chelsea Heveran

Contributions: Supported experiment design, data analysis, writing, and review process.

Manuscript Information

Sobia Anjum, Kaylin Clark, Amir Darabi, Lewis Cox, Chelsea Heveran, and Robin Gerlach

Status of Manuscript:

_X_ Prepared for submission to a peer-reviewed journal

____ Officially submitted to a peer-reviewed journal

____ Accepted by a peer-reviewed journal

____ Published in a peer-reviewed journal

5.1 Abstract

Biologically and enzymatically induced biomineralization has been well optimized for engineering applications such as soil consolidation, concrete remediation, and below-ground fracture biocementation. The broad structural applications of biologically induced biomineralization stem from the robustness and customizability of the process. Yet, for applications such as mineral fillers in engineering adhesives, the role of organics in modulating the microscale material properties of such biominerals is not well understood. The material properties of biogenic biomaterials on the other hand, are well understood and highly dependent on the organic-mineral interface and its hierarchical distribution. The biomimetics of biogenic biominerals offers the inspiration for the use of organics to control mineral structure and material properties in biologically induced mineral precipitation. The goal of this study was to determine the structure and material properties of enzymatically induced calcium carbonate minerals formed in the presence of a well-known protein additive, bovine serum albumin. The calcium carbonate precipitates were formed using jack bean meal, both in the absence and presence of bovine serum albumin. The structural and polymorphic variations of the mineral precipitates were assessed by FE-SEM and XRD analysis, and the material properties of the mineral aggregates were assessed by nanoindentation and atomic force microscopy (AFM). The calcium carbonate precipitates formed in the presence of bovine serum albumin had lower moduli than those formed without these organics. Atomic force microscopy analysis confirmed the presence of low moduli regions in the abiotic and enzymatic precipitates formed in the presence of bovine serum albumin. Furthermore, the presence of bovine serum albumin introduced structural variations and moduli gradation in biominerals that resemble structural and material properties

heterogeneities observed in biogenic and geologic minerals. These results demonstrate that the presence of organics can alter the nanoscale structure and material properties of calcium carbonate precipitates.

5.2 Introduction

Biomimetic biomineralization is a frontier in synthetic biochemistry that uses nature-inspired pathways to achieve specific structure and function for the development of new materials (Deng et al., 2022c; Harris et al., 2017; Weiner, 2008). Biomineralization is referred to here as the precipitation of inorganic mineral phases through interactions between bio-macromolecules (e.g., enzymes or whole cells) and inorganic ions. The two broad categories of biominerals that have been extensively researched are biogenic minerals and geologic minerals (Görgen et al., 2021; Harris et al., 2017). Biogenic minerals are made because of cellular activity. In this process, biomacromolecules play an active role in control of mineral size, morphology, orientation, and consequently their material properties (Evans, 2017; Kunitake et al., 2013; Wallis et al., 2022). In the past the presence of organics in geologic minerals was assumed to be entirely coincidental, and it was debated whether the organics played any role in the mineral precipitation (Dhami et al., 2018). Today, there is a growing body of evidence that shows that microbial activity also plays a significant role in the formation of geological minerals (Kleber et al., 2021; Possinger et al., 2020). The geologic minerals in nature have a complex organic profile depending on the environmental conditions and the archeological and microbe-mineral interaction-based origins (Weiner & Dove, 2003). The formation of biominerals by microbial activity and products of microbial activity are referred to as biologically or microbially induced mineral precipitates. The limited understanding of the role of organics and the

apparently passive role of organics in biologically induced mineralization may have limited the active use of organics in potential engineering applications.

The use of organics has been central for the control of mineral morphology and material properties in biomimetic synthesis of biogenic minerals (Bar-Cohen, 2012; Liu & Oyen, 2014; Nudelman & Sommerdijk, 2012; Xiong et al., 2018), but the use of organics in biologically induced mineral precipitation remains relatively unexplored. Biogenic minerals have been of high interest due to the unique material properties, which are influenced by their microscale structural motifs. Studies on the material properties of biogenic biominerals have shown that microscale distribution of mineral and organic interfaces confers unusual combinations of high strength, stiffness as well as fracture toughness to biomaterials such as nacre and bones (Barthelat et al., 2016). The biomineral features in certain regions of sea urchin spicule, nacre and mollusk shell have high hardness and elastic modulus but are surprisingly resistant to inelastic deformation and cracking (Bar-Cohen, 2012; Labonte et al., 2017). Where synthetic minerals and ceramics are prone to brittle fractures, biominerals often have crack deflection mechanisms due to disordered structures at the nanoscale (Deng et al., 2022). This toughness and nanoscale disorder of biogenic minerals has been attributed to ion substitutions in minerals, the presence of intra-crystalline organics, amorphous phases, polycrystallinity and twinning boundaries within the biominerals (Deng et al., 2022; Deng & Li, 2021). The common underlying factor associated with these structures is the presence of organics.

The presence of organics is ubiquitous to mineral precipitation in nature from biosignatures of flora and fauna in geologic minerals (Dhami et al., 2018), interactions of microbes and microbial exopolymeric substances with minerals (Azulay et al., 2018; Zhu & Dittrich, 2016), to precise control of calcitic structures in eukaryotes (Nudelman & Sommerdijk,

2012). Harris et al. proposed that the presence of inter and intra- crystalline organics is a structural commonality between biogenic and geological minerals (Harris et al., 2017). Yet, the structure-material property relationships have mostly been explored for biogenic minerals so far. The challenge and opportunity lie in determining the commonalities in structure-property relationships in biominerals to improve the design of biominerals by both biogenic and biologically induced mineralization pathways (Cranford et al., 2013).

The role of organics in biologically induced mineralization is highly complex due to timescale of geological mineral formation, and a large variability in environmental conditions that can influence the mineral precipitation kinetics (Cho et al., 2019; De Yoreo, 2003), morphology and polymorphism (De Yoreo, 2020; Evans, 2017; Xu et al., 2019). In-vitro experiments have been conducted to understand and modify the aggregation behaviors in geologic minerals in the presence of a concoction of microbial extracellular materials similar to found in nature (Cho et al., 2019; Guhra et al., 2019; Newcomb et al., 2017) In-vitro incorporation of nacre proteins has been shown to modify even the material properties of abiotic calcite crystals (Risan et al., 2018). The work of adhesion between bacterial EPS and geological minerals has been shown to depend on the respective charges on the compounds, positively charged mineral showed favorable interactions with microbial extracellular polymeric substances which carry negative charges (Sand et al., 2017). Protein-like micelles (PSPMA30-PDPA47) were shown to incorporate into geologically sourced calcium carbonate during mineral growth, whereas Bovine serum albumin was shown to have no structural or kinetic influence of crystal growth (Cho et al., 2019). Cho et al proposed that the inclusion of the protein and protein-like micelles in mineral was dependent on the binding strength of a macromolecule to a mineral face and the growth rate of the mineral. The use of complex organics such as EPS and geologic

minerals to determine organo-mineral interactions offers insights into the in-vivo interactions at the soil-mineral-organic interfaces but remains too complex to determine specific cause-effect relationships to mimic the processes in-vitro. Other in-vitro studies are often carried out by abiotic precipitation of mineral precipitates have shown that the presence of organics such as amino acids and oligopeptides can influence the shape and morphology of carbonate minerals (Finney et al., 2020), as well as material properties such as hardness of calcium carbonate precipitates (Côté et al., 2015; Kim et al., 2016). However, the role of biomacromolecules as additives and their structure-property relationships for enzymatic and microbially induced biomineralization remains unclear.

Ureolytically induced calcium carbonate precipitation (UICP) is a type of biologically induced biomineralization process which has been extensively engineered for binder and sealants, bioremediation, and bioaccumulation applications (Phillips et al., 2013; Van Wylick et al., 2021; Zhu & Dittrich, 2016). The ureolytically induced biomineralization is relatively simple, scalable, and is effective for heterogeneous biomineralization applications in porous substrates (Krajewska, 2018; Knorre & Krumbein, 2000). A few studies have also shown recently that the compressive strength of porous materials cemented by ureolytically induced biomineralization can be improved by the addition of animal-based protein complexes such as whey, milk and single protein e.g., casein (Arab et al., 2021; Miyake et al., 2022). It has been shown that the use of different ureolytic strains of bacteria can also alter the nanoscale material properties of the biologically induced minerals, but it remains undecided whether bacterial cells or their by-products affected these material properties (Heveran et al., 2019).

In this study, we explore the material properties of calcium carbonate precipitates formed by UICP in the presence of bovine serum albumin. The ureolysis was carried out by jack bean

ureases which hydrolyze urea to release carbonate ions, and ammonium ions. The stoichiometric balance of the ammonium and carbonate production by ureolysis results in a pH increase which favors precipitation of calcium carbonate (Hammes & Verstraete, 2002; Parks, 2009). To determine the effect of a protein on the physicochemical and material properties of the biominerals, the reaction was carried out in the presence and absence of BSA. This work offers insight into the use of a protein to control the material properties of ureolytically induced calcium carbonate precipitates for their applications as biominerals in biopolymer materials.

5.3 Materials and Methods

Jack bean meal (JBM) and bovine serum albumin (BSA) were purchased from Sigma Aldrich. All solutions were prepared in deionized water with an electrical resistivity of ≥ 18.2 MΩ.

5.3.1 Preparation of Enzymatically Induced and Abiotic Calcium Carbonate Precipitates

The ureolytic solution was prepared by mixing 5 g/l of fine powdered JBM in deionized water for 24 hours. Before use, the resulting suspensions were filtered through 0.22 μm pore size bottle top filters (Nalgene Rapid-Flow Filters, Thermo Scientific). The enzymatically induced calcium carbonate precipitates (EICP) were prepared by mixing JBM solution with a solution containing 100mM urea and 100mM calcium chloride at a 1:1 ratio, to reach final concentrations of 2.5g/l JBM, 50mM urea, and 50mM calcium at a final volume of 40ml in Falcon® 50 ml polypropylene centrifuge tubes (Corning). The EICP-BSA treatments contained a final concentration of BSA of 10g/l. The abiotically induced calcium carbonate precipitates (AICP) were prepared by mixing 20ml each of 100mM $CaCl_2$ and 100mM $NaHCO_3$ solutions to reach a

final concentration of 50mM for each compound. AICP-BSA samples were prepared with a final concentration of 10g/l BSA; BSA-free controls were set up as well. Four replicates were prepared for each reaction type, EICP, EICP-BSA, AICP, and AICP-BSA. The vials were placed in a shaking incubator at room temperature 23± 2℃ for 5 days to allow ureolysis, induction of $CaCO_3$ precipitation, and precipitate maturation. After 5 days precipitates were harvested using centrifugation at 5000 x g for 5 minutes at 21˚C. Precipitates were rinsed in DI water and air-dried at room temperature 23± 2℃ for 24 hours followed by 30± 2℃ for 5 days.

5.3.2 Mineral Morphology and Composition Assessments

The mineral precipitates were mounted on carbon tape and coated with a carbon layer to prevent charging during imaging. The imaging was done between accelerating voltage of 1-5kV at a 30μm aperture size, on a Zeiss SUPRA 55VP Field Emission Scanning Electron Microscope (FE-SEM).

For X-ray diffraction analysis (XRD), approximately 3-5mg of precipitates were crushed into a powder on a glass slide using stainless steel metal spatula, and 70% ethanol was used to disperse the powders into a thin layer. After the ethanol evaporated, the sample was inserted into a Bruker D8 Advance instrument. X-ray diffraction spectra were obtained using a 2θ range from 5-70° at the instrument's Cu K-alpha source. The sample spectra were analyzed for peak fits using MDI Jade software.

Subsets of the dried precipitates from each sample were embedded in epoxy and prepared for materials testing as described in section 5.3.3. After the materials testing by nanoindentation (5.3.4 & 5.3.5), the epoxy-embedded samples were sputter-coated with carbon before undergoing

high-resolution backscatter imaging (15kV, aperture 30µm) using FE-SEM. The samples were scanned to assess density variations within and between the precipitates for each sample.

5.3.3 Microscale Assessment of Material Properties of Mineral Precipitates

Subsets of the dried precipitates from each sample were embedded in epoxy (Buehler Epoxicure) and sectioned with a low-speed diamond saw (Isomet, Buehler), irrigated with water. The epoxy-embedded samples were smoothed with 600 and 1000-grit silicon carbide papers (Buehler), followed by polishing with 9, 6, 3, and 1 µm oil-based Beuhler MetaDi diamond suspensions. The final polishing step was performed with a 0.05µm alumina suspension to achieve a mirror finish. Between each polishing step, the samples were rinsed and sonicated in 100 percent ethanol to minimize the dissolution of $CaCO_3$ in water. Nanoindentation (NI) analysis was performed on each of the 4 experimental groups (4 replicates each; N =16 samples) using a Berkovich tip, KLA Tencor iMicro. The nanoindentation sites were selected such that a grid of 150-200 indents was placed on each region with spacing of 15µm (x and y). A trapezoidal load profile was applied using a 30s loading, hold, and unloading cycle, with a target load of 3 mN. The hold time was sufficient to dissipate viscoelastic energy within the sample. The moduli of the samples were calculated using the Oliver Pharr method (Oliver & Pharr, 1992). Briefly, a polynomial curve was fitted to the 95th – 20th percentiles of the unloading curve. The reduced nanoindentation modulus (E_r) can be calculated from:

Equation 5.1
$$E_r = \frac{S}{2}\sqrt{\frac{\pi}{A_c}}$$

The stiffness (S) of the samples was calculated from the derivative of a tangent line at the beginning of the polynomial fit. The tip contact area (A_c) was calibrated as a function of depth

(h_c) on a fused silica reference sample. However, the E_r is a function of the material properties (moduli) of the sample (E_s) and the indenter tip (E_t) as well as the Poisson ratios of the sample (v_s) was assumed to be 0.3 and the tip (v_t) defined by:

Equation 5.2 $$\frac{1}{E_r} = [\frac{1(1-v_s^2)}{E_s} - \frac{(1-v_t^2)}{E_t}]$$

The nanoindentation modulus E_i of samples was calculated from the reduced modulus E_r using Equation 5.3, where the tip properties (v_t and E_t) are known, and Poisson ratio v_s assumption is 0.3.

Equation 5.3 $$E_i = \frac{E_s}{(1-v_s^2)} = [\frac{1}{E_r} + \frac{(1-v_t^2)}{E_t}]^{-1}$$

Each loading and unloading curve for a nanoindentation indent was analyzed before calculating the E_i and H values for a sample. It is known that strain hardening, strain softening, and displacement bursts (porosity) of samples can contribute to errors in measurements of the elastic moduli and hardness of the data (Gale & Achuthan, 2014). The sample load depth profiles with representative effects of strain hardening, strain softening, and porosity on the load depth profiles excluded from further data analysis (Figure 5.S1). Example subsets of load depth profiles included in data analysis for each sample are given in Figure 5.S2. The epoxy used for the embedding of the samples has an E_i of ~5 GPa upon curing. The nanoindentation data points of moduli ≤5 GPa were removed from the analyses, as they were likely from epoxy or an epoxy-rich mineral interface.

Indentation hardness (H_i) was used to quantify the contributions from both elastic and inelastic deformation on the sample during indentation. Indentation hardness was calculated from maximum load and corresponding contact area by:

Equation 5.4 $$H_i = \frac{P_{max}}{A_c}$$

The resistance to deformation for each sample was measured by H_i / E_i.

5.3.4 Submicron Scale Assessment of Material Properties of Mineral Precipitates

One sample from each experimental group was taken for nanoscale analyses using atomic force microscopy (AFM, Asylum research, Cypher S). A 200 N/m spring constant tip (RTESPA-525, Bruker) was used to accommodate the high stiffness of the samples. AFM was operated in two different modes: AC tapping mode for topography scans and fast force mapping (FFM) for modulus maps. Using AC tapping mode, the cantilever was driven at a constant amplitude at its resonance frequency and scanned across the surface to locate minerals and measure their topography. Fast force mapping generated an array of local force-distance curves, obtained at high speed with nanometer spatial resolution, and was used to characterize modulus profiles of mineral precipitates. Tip parameters were calibrated and resulting force curves were fit to a Hertzian contact model to calculate the contact modulus of the material. First, calibration of a cantilever spring constant was obtained via thermal tune. Next, a force-distance curve was performed on a silicon wafer (Silicon Inc., Boise, ID) to calculate optical lever sensitivity. Once these values were obtained, tip radius was calibrated by first acquiring a fast force map (320 × 320-pixel map) of a glass surface with known modulus (72 GPa, Fisherbrand, Pittsburgh, PA) then identifying the tip radius value needed to generate agreement of the Hertz model with the glass calibration surface. AC tapping mode was used to generate 20µm x 20µm topography maps of three random locations across the surface of the sample. Additionally, two regions of 7µm x 7µm were scanned to generate topography maps. FFM-provided modulus maps at a trigger force of 500 mN and analyzed using a Hertzian model. After each modulus scan, the radius of the tip was calibrated on a glass surface with known modulus (72 GPa, Fisher brand) to account for

possible tip wear during each FFM scan. All topography and modulus scans were conducted at 320 x 320 pixels.

5.3.5 Statistical Analysis

Two-factor ANOVA was used to test whether the material properties E_i, H_i or H_i/E_i were influenced by enzymatic ureolysis, the presence of BSA, or an interaction between the two factors. Significance was set at 95% confidence, and p-values < 0.05 were deemed indicators for statistically significantly different values. For all models, residuals were tested for normality and homoscedasticity. Post-hoc testing was performed for significant interactions using a Tukey correction to adjust critical alpha for family-wise error.

5.4 Results

5.4.1 Mineral Morphology and Mineral Phase Assessments

The EICP formed had varying morphologies, including rhombohedral, spherulite, polycrystalline mineral precipitates (Figure 5.1). The AICP show rhombohedral calcite-like morphology, with terraces (1) on some of the crystal growth faces, possibly due to the presence of impurities in the solutions (Figure 5.1 A). The polycrystalline precipitates (1) in EICP have multiple crystalline faces growing in different directions (Figure 5.1 B). The spherulite morphology in EICP includes smooth spherical precipitates of varying sizes (2). In AICP-BSA and EICP-BSA conditions the size of the precipitates was smaller, and the predominant morphology was spherical.

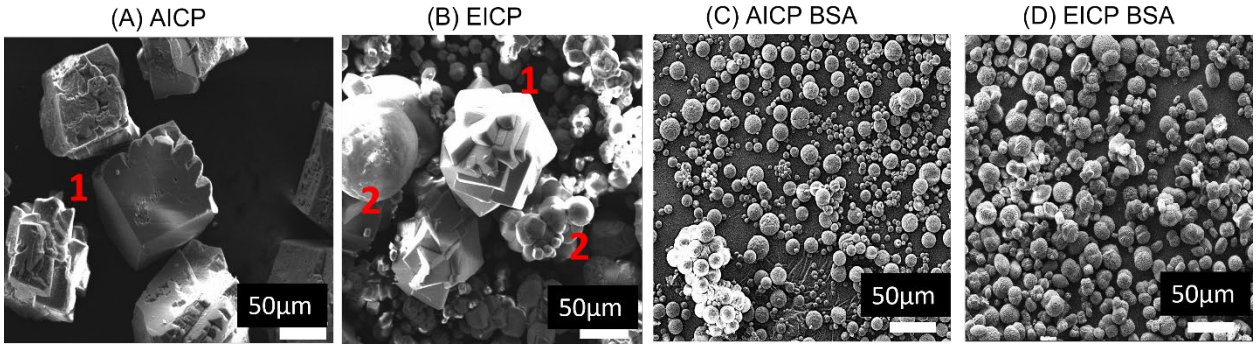

Figure 5.1: The mineral precipitates in (A) AICP have sharp smooth edge morphology with rhombohedral form commonly observed in calcite polymorphs of calcium carbonate, with precipitates that show growth terraces. (B) The EICP have varying morphologies, including polycrystalline calcite like morphology (B1) and spherulites (B2). (C &D) The AICP-BSA and EICP-BSA precipitates have smaller precipitates and predominantly spherical morphologies.

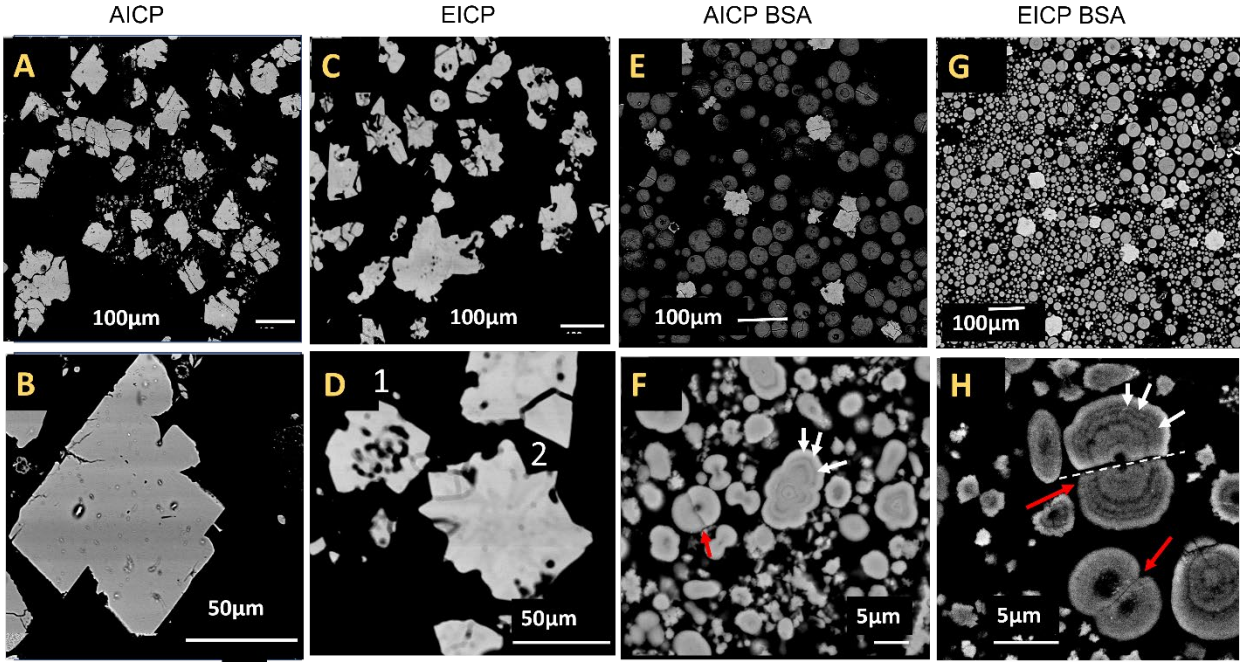

Figure 5.2: Backscattered electron (BSE) images of AICP, EICP, AICP-BSA and EICP-BSA samples embedded in epoxy. (A, B, C, D) The AICP and EICP samples have larger precipitate sizes than (E, F, G, H) AICP-BSA and EICP-BSA precipitates. (E, F) The AICP-BSA and (G, H) EICP-BSA show density variations in the precipitates, based on the BSE signal intensity. Brighter precipitates indicate a higher BSE signal and potentially have a higher molecular density. (F, H) At higher magnifications, the AICP-BSA and EICP-BSA samples show density variations within precipitates in the form of lamellar structures and circular growth rings in the precipitates, indicated by white arrows, and twinning features indicated by red arrows.

Backscattered electron images of the sections show the density variations in the internal structure of precipitates exposed after sectioning and polishing the samples (Figure 5.2 D, F&H). The EICP single crystal shows porosity (D1) as well as density variations in the single crystal (D2) indicative of multiple planes of crystal growth (Figure 5.2 D). The variations in density within a single crystal in EICP precipitates agree with the observations of polycrystallinity in Figure 5.1 B. Both AICP-BSA and EICP-BSA show the presence of growth rings/lamellae and twin structures indicated by white arrows and red arrows respectively in Figure 5.2 F&H. Formation of rings, lamellae, polycrystalline calcite polymorphs, and twinning calcite have previously been reported for biogenic and geologic minerals in-vivo (Barthelat et al., 2016; Kunitake et al., 2013; Liu et al., 2023; Locht, 2014) and in-vitro (Côté et al., 2015; Deng et al., 2020; Pokroy et al., 2007).

The AICP and EICP specimens mostly consist of calcite, and there was no detectable vaterite (Figure 5.3). Abiotic and enzymatic mineral precipitates formed in the presence of BSA has spherulite morphologies (Figure 5.1 C&D), but EICP-BSA was calcite, but both AICP-BSA was vaterite.

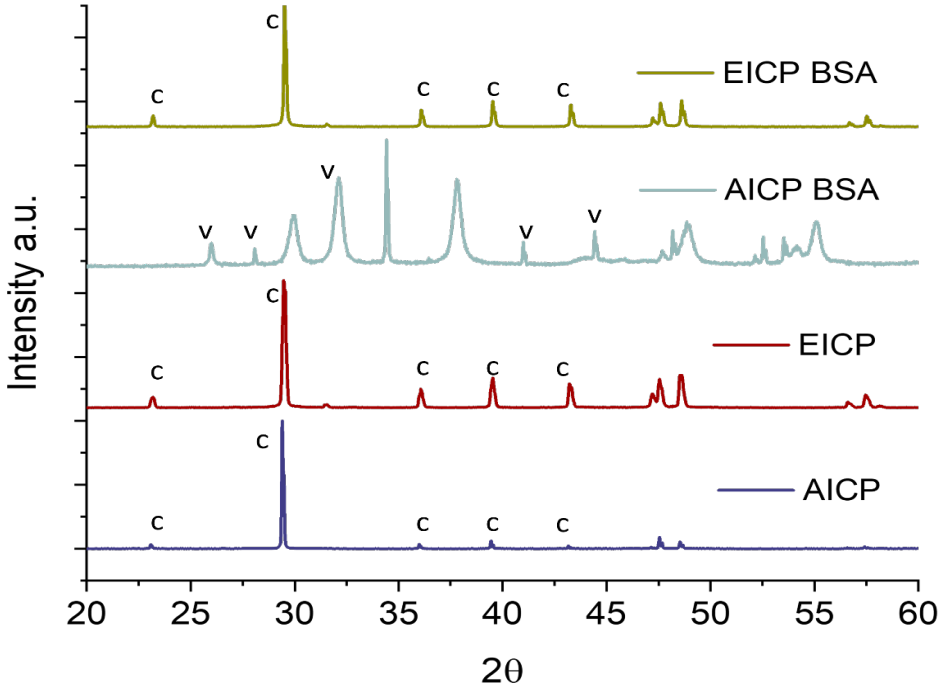

Figure 5.3: X-ray Diffraction spectra of AICP, EICP, AICP-BSA, and EICP-BSA samples. Letters ‘c’ and ‘v’ indicate peaks indicative of calcite and vaterite, respectively. The AICP, EICP, and EICP-BSA spectra appear to be dominated by peaks indicative of calcite, whereas the AICP-BSA samples have peaks indicative of vaterite.

5.4.1 BSA Modifies the Elastic Moduli and Hardness of enzymatically induced mineral precipitates

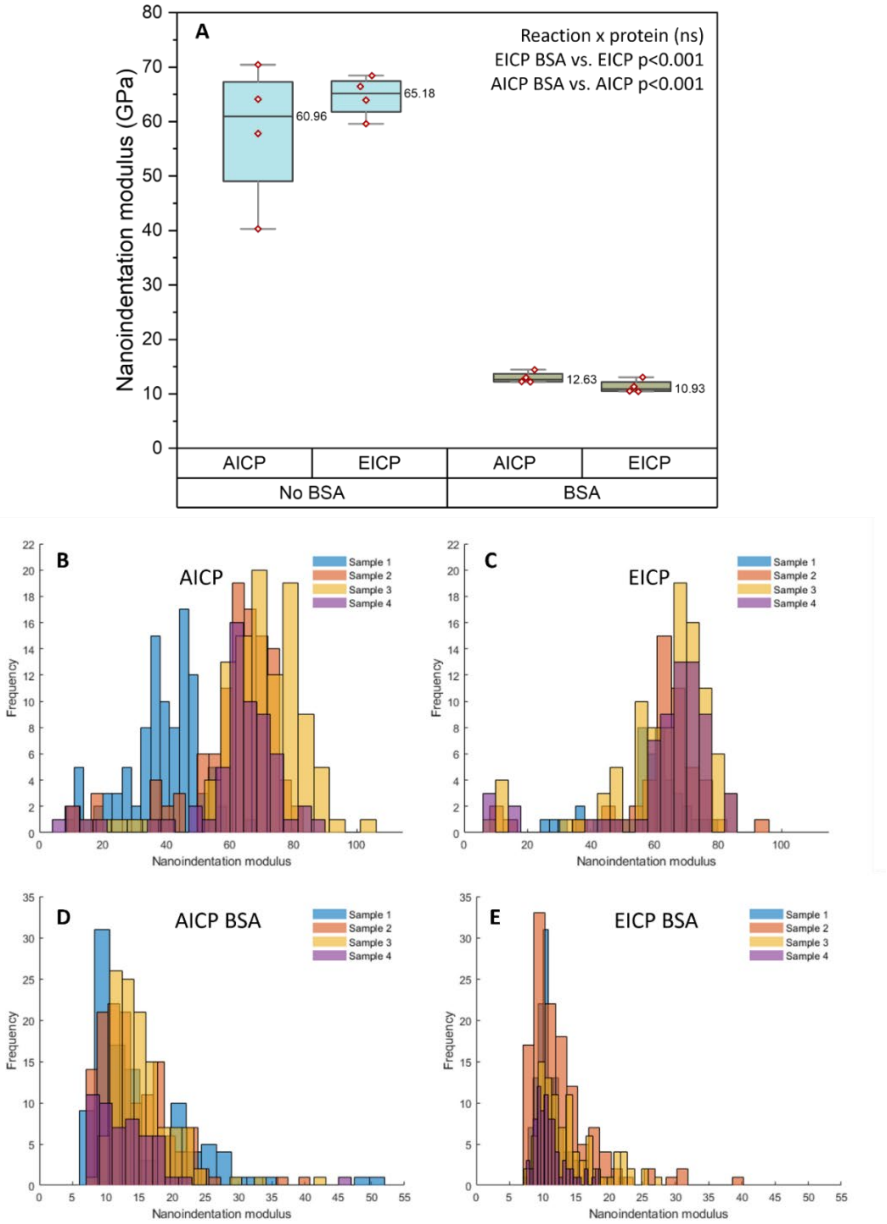

Figure 5.4: (A) Nanoindentation elastic moduli (E_i in GPa) and (B-E) their probability distribution for AICP, EICP, AICP-BSA, and EICP-BSA samples. (A) Nanoindentation moduli for abiotically and enzymatically induced precipitates formed without BSA were significantly higher than the respective samples with BSA. The data points (◊) on each box represent the median of 50-100 indents for each replicate (n=4) in each experimental condition. The upper and lower bounds of the boxplot represent the 25th and 75th percentiles, and the whiskers indicate the minimum and maximum values. (B, C) The distribution of nanoindentation moduli in AICP

and EICP is skewed left towards lower moduli. (D, E) The AICP-BSA and EICP-BSA samples have a right-skewed distribution toward higher moduli.

The nanoindentation moduli of the samples were significantly influenced by the presence of BSA ($p= 0.001$), but not by the reaction type. *i.e.*, abiotic vs. enzymatic precipitation reaction ($p>0.05$) (*cf*. Figure 5.5 and Table 5.S1). The elastic moduli of AICP-BSA and EICP-BSA were 78.4% and 83.1% lower than their respective BSA-free AICP and EICP samples ($p<0.001$ in both cases). The effect of BSA on the elastic moduli of the precipitates was independent of the effect of reaction type (abiotic vs enzymatic precipitation), *i.e.*, the interaction between the presence of BSA and reaction type was not significant ($p=0.1$).

In contrast, the effect of BSA on the nanoindentation hardness of precipitates was dependent on the effect of reaction type (reaction x protein, $p = 0.01$). The hardness of EICP was significantly higher than that of AICP (3.32 ±0.75 GPa vs. 2.42 ±0.52 GPa, $p=0.01$), but the hardness for AICP-BSA and EICP-BSA was not statistically significantly different ($p=0.4$, Table 5.1). As with nanoindentation elastic moduli, the nanoindentation hardness of the AICP-BSA and EICP-BSA were significantly lower than AICP and EICP, respectively ($p<0.001$ for both AICP vs. AICP-BSA and EICP vs. EICP-BSA).

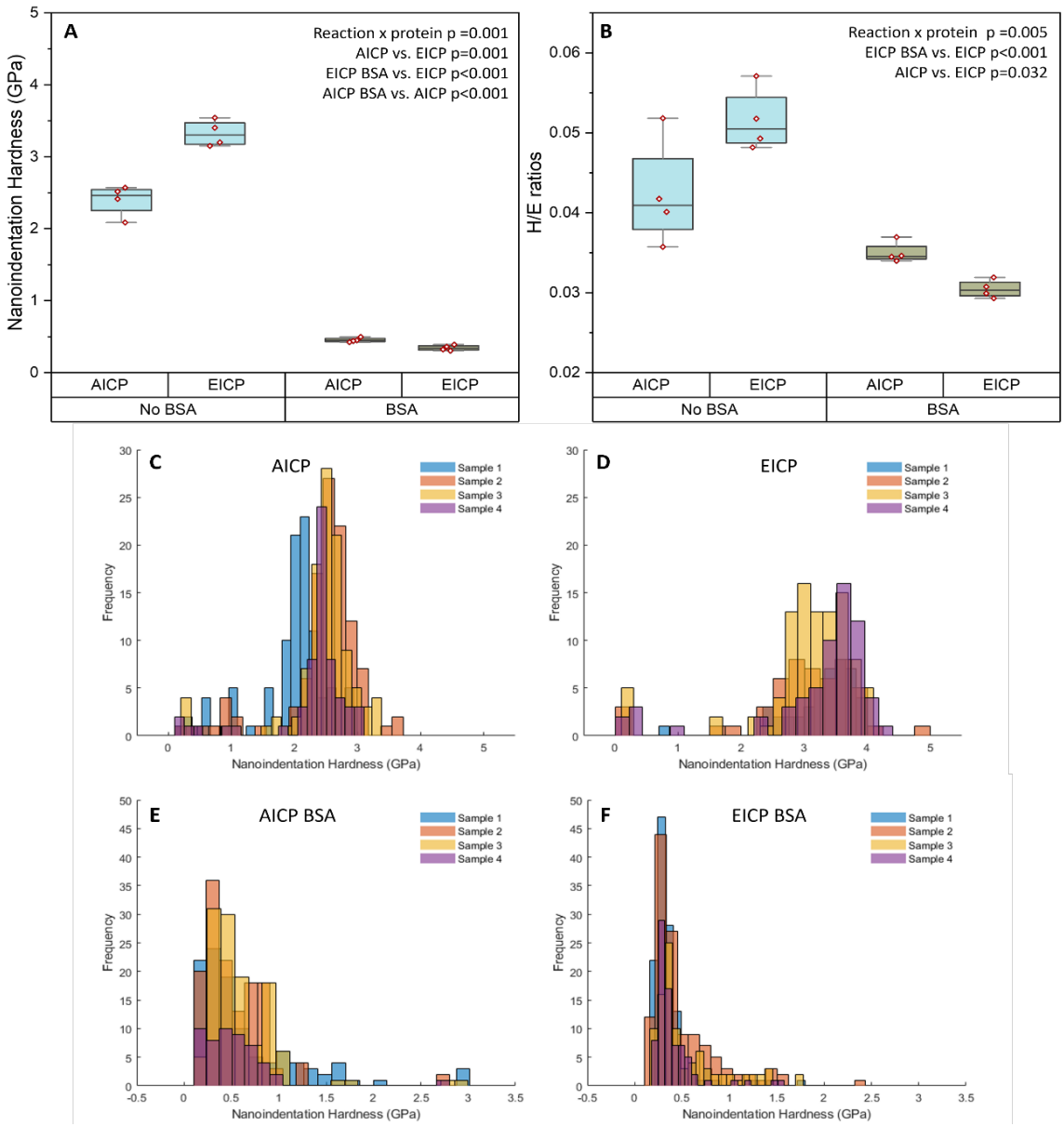

Figure 5.5: (A) Boxplots for nanoindentation hardness (H_i in GPa), (B) the resistance to inelastic deformation (H_i/E_i) and (C-F) probability distributions of AICP, EICP, AICP-BSA, and EICP-BSA samples. (A) Nanoindentation hardness for abiotically and enzymatically induced precipitates formed without BSA were significantly higher than the respective samples with BSA. The data points (◊) on each box represent the median of 50-100 indents for each replicate (n=4) in each experimental condition. The upper and lower bounds of the boxplots represent the 25th and 75th percentiles, and the whiskers indicate the minimum and maximum values. (C, D) The distribution of nanoindentation hardness in AICP and EICP skews left towards lower moduli. (E, F) The AICP-BSA and EICP-BSA nanoindentation hardness have a right-skewed distribution towards higher values.

The probability distributions of nanoindentation moduli and hardness for AICP and EICP are left skewed (Figure 5.4 B & C, Figure 5.5 C&D). For example, the 25th and 75th percentile of nanoindentation hardness for AICP is between 2.12 and 3.7 GPa, with a small probability distribution of hardness values <2 GPa. Similarly, the 25th and 75th percentile of AICP nanoindentation moduli is between 45.07 and 70.07 GPa, and a small probability distribution of indents with moduli <25 GPa. Though indents were excluded on epoxy or evidently on epoxy interfaces, some indents may nonetheless interact with epoxy subsurface and potentially contribute to the few lower values.

The low elastic moduli for AICP-BSA may be due to the presence of vaterite (Figure 5.3). Yet, the reason for reduced elastic moduli in EICP-BSA is probably different. For EICP-BSA samples, only calcite was detected while vaterite was below detection limits. Therefore, the low elastic moduli in EICP-BSA are not necessarily low due to the presence of a less crystalline mineral polymorph and may be due to the inter- and intra-crystalline protein-mineral interactions.

The probability distributions of nanoindentation moduli and hardness for AICP-BSA and EICP-BSA are right-skewed (Figure 5.4 D&E). This right skew could result from a few precipitates with higher relative density in the AICP-BSA and EICP-BSA, where a few higher relative density precipitates are interspersed with predominantly low relative density precipitates (Figure 5.2 E&G). Regions of high atomic density can have higher hardness (Rabiei et al., 2020).

Table 5.1: Distribution of nanoindentation moduli and hardness data for abiotically and enzymatically induced calcium carbonates formed in the presence and absence of BSA.

Nanoindentation modulus	Min	Q1	Median	Q3	Max	IQR
AICP	6.912	45.071	61.352	70.071	104.473	25
AICP-BSA	7.176	10.593	13.253	17.571	50.901	6.978
EICP	7.835	57.956	65.088	70.821	94.407	12.865
EICP-BSA	7.352	9.67	11.022	13.418	40.022	3.747
Nanoindentation hardness	Min	Q1	Median	Q3	Max	IQR
AICP	0.139	2.1205	2.4285	2.648	3.701	0.5275
AICP-BSA	0.166	0.3	0.463	0.741	3.02	0.441
EICP	0.113	2.8742	3.3155	3.6335	4.802	0.7593
EICP-BSA	0.163	0.271	0.341	0.489	2.427	0.218

Previous research has shown that the hardness and modulus data from nanoindentation can be used to assess elastic vs. plastic deformation in materials by measuring their H_i/E_i ratios (Cheng & Cheng, 1998; Yang et al., 2008). A high H_i/E_i suggests a brittle fracture in materials upon fracture and vice versa. Therefore, low H_i/E_i is a desirable feature of biominerals as it represents a higher elastic vs. plastic deformation in materials (Labonte et al., 2017).

The resistance to inelastic deformation, used as an indicator of resistance to crack propagation) was measured from the elastic modulus and hardness of the precipitates. The resistance to inelastic deformation was significantly lower in the presence of BSA for both abiotic and enzymatic calcium carbonate precipitates (Figure 5.4B). EICP specimen had the highest resistance to deformation, whereas EICP-BSA specimen had the lowest resistance to deformation in the presence of BSA (EICP vs. EICP-BSA, $p < 0.001$). Overall, there was a

significant effect of BSA on all material properties of the samples, *i.e.*, nanoindentation modulus, hardness, and resistance to inelastic deformation. For AICP vs. AICP-BSA and EICP vs. EICP-BSA, the hardness and elastic moduli are significantly lower in the presence of BSA $p < 0.001$. The resistance to inelastic deformation (H_i/E_i) of EICP-BSA stands out as significantly lower than all other precipitates (AICP-BSA vs. EICP-BSA, $p=0.032$, and EICP vs. EICP-BSA $p< 0.001$, Table5.S5).

In biogenic minerals, the low H_i/E_i or a high elastic response is explained by their fracture mechanisms. For example, in marine shell bivalve *Atrina rigida*, fractures occur at the micron and submicron scale during nanoindentation and the intracrystalline defects in minerals offer tortuous paths for crack propagation (Deng et al., 2020). Such microscale fractures can dissipate stress and block crack propagation and improve damage tolerance of biominerals. Another reason for low H_i/E_i can also be the presence of low-stiffness components such as organics or a biopolymer matrix. For example, Risan et al. showed that incorporation of recombinant nacre protein hydrogel in the calcite crystals lowered their stiffness and hardness (Risan et al., 2018). Since the hardness, as well as stiffness is significantly lowered for abiotic and enzymatic calcium carbonate precipitates formed in the presence of BSA, there is a higher probability that the mineral itself is not stiff or there is considerable incorporation of organics into the minerals.

5.4.3 The Presence of BSA Increases Microscale Heterogeneity in Biomineral Precipitates

To assess whether the low hardness and elastic moduli observed in AICP-BSA and EICP-BSA precipitates were similarly represented at submicron scale, AFM force mapping was conducted for the epoxy embedded AICP, EICP, AICP-BSA, and EICP-BSA precipitates. The

AICP and EICP maps show a relatively uniform surface topography and a normal distribution of moduli whereas the AICP-BSA and EICP-BSA samples show topographical variability and a right skewed distribution of moduli (Figure 5.6 vs. Figure 5.7). To evaluate the distribution of moduli in the AFM modulus maps, the data was first screened for modulus values that fit the AFM tip calibration range. AFM moduli valued ≤0 GPa were excluded as illogical outputs and ≥150 GPa were excluded due to the tip calibration limits. AFM moduli of epoxy regions were calculated to be ~5.12 GPa, hence AFM moduli ≤5 GPa were eliminated to exclude epoxy rich regions from the median calculation outputs.

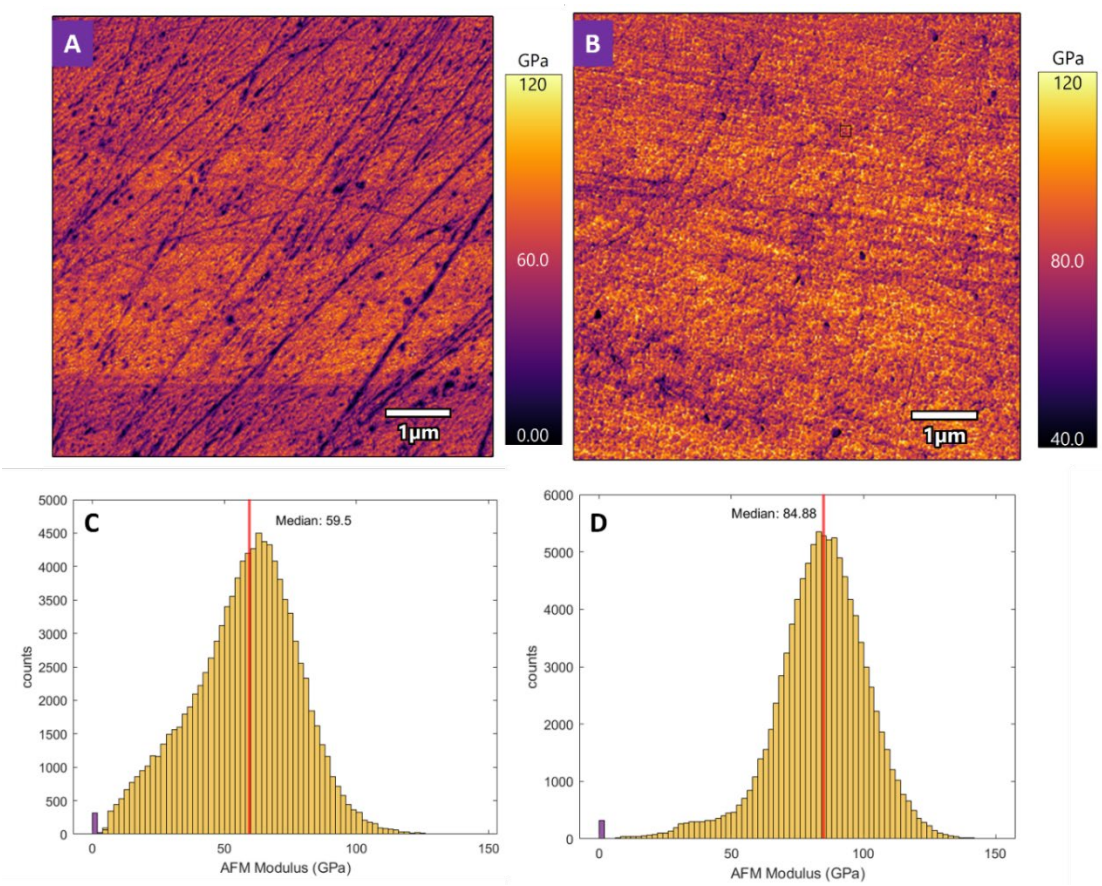

Figure 5.6: AFM modulus maps of (A) AICP and (B) EICP show a distribution of moduli across the samples. The histograms were generated by screening the AFM modulus data and are separated by modulus values: <5GPa (magenta) likely from epoxy regions and >5GPa and <150GPa modulus values in (yellow) bins likely from calcium carbonate precipitates. The

distribution of moduli for both (C) AICP and (D) EICP is quasi-Gaussian-normal; the AICP have a higher number of events in the lower moduli regions <50GPa. Overall, the median of the AICP moduli (59.5 GPa) are lower than the median of the EICP moduli (84.88 GPa), p>0.05 (Table 5.S7).

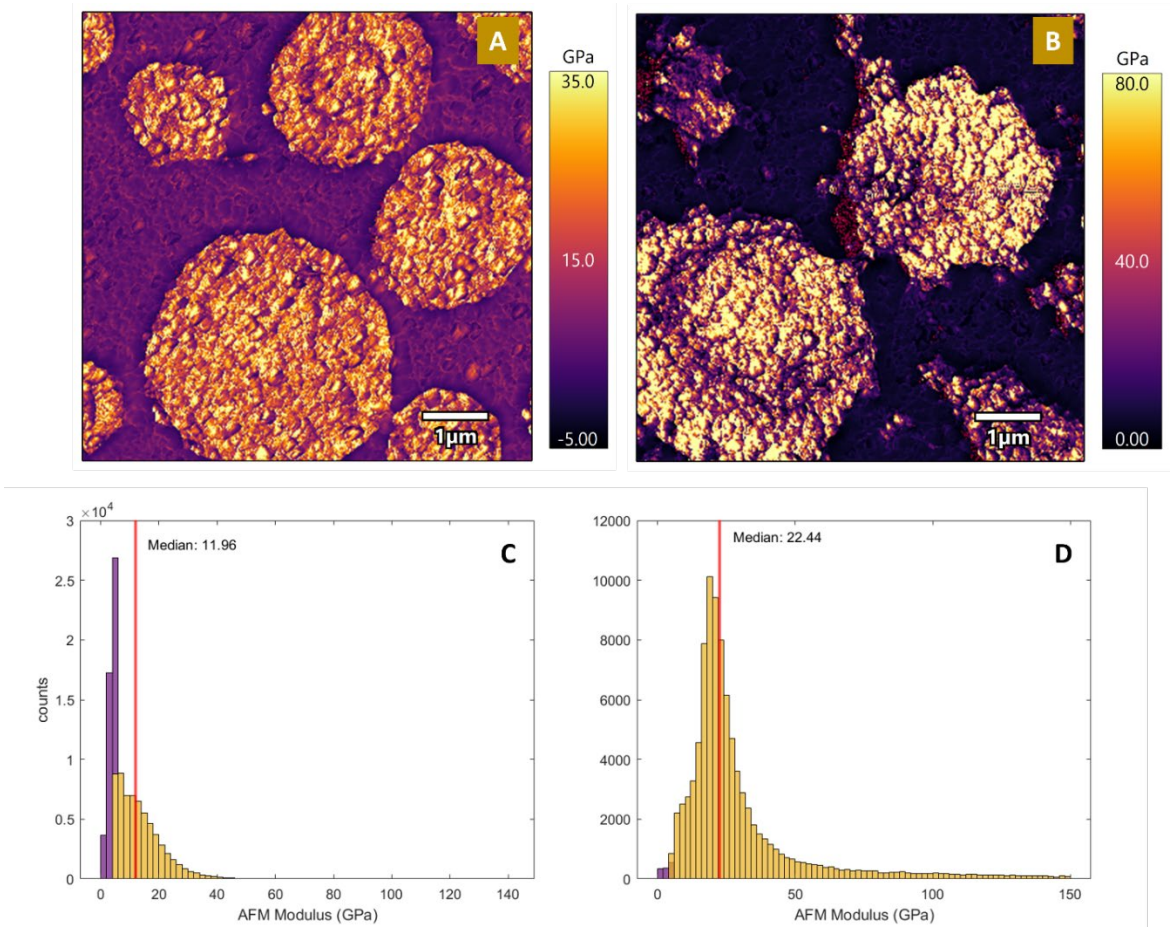

Figure 5.7: AFM modulus maps of (A) AICP-BSA and (B) EICP-BSA precipitates show a distribution of moduli across the samples. The histograms were generated by screening the AFM modulus map data, and separated by modulus values: <5GPa (magenta)for epoxy regions and >5GPa and <150GPa modulus values in (yellow) bins likely from calcium carbonate precipitates. The distribution of moduli for both (C) AICP-BSA and (D) EICP-BSA are left skewed and in agreement with the nanoindentation data in (Figure 5.4 D&E). The upper limit of moduli for AICP-BSA is lower (50 GPa) as compared to EICP-BSA precipitates (150 GPa).

Table 5.2: Sample medians of elastic modulus (GPa) of regions analyzed using AFM force mapping.

AFM map region	AICP	EICP	AICP-BSA	EICP-BSA
1	42.6	55.99	12.88	10.34
2	57.78	60.87	11.96	13.23
3	47.65	84.09	11.76	9.06
4	73.18	84.2	11.12	22.44

The larger size and higher AFM moduli (indicative of higher compactness) of AICP and EICP samples potentially minimized the penetration of epoxy and its interference with the moduli measurements. There is a clear distinction between the bins with moduli ≤5 GPa and the ones that are higher (Figure 5.6 C&D). The AFM moduli for AICP and EICP show a normal distribution (Figure 5.6). However, the AICP-BSA and EICP-BSA samples show a left skew in their moduli distribution (Figure 5.7).

The distributions of moduli in AFM maps highlight differences in moduli gradation between AICP-BSA and EICP-BSA samples. The EICP-BSA samples have a broader range of moduli distribution (5 to 150 GPa) than the AICP-BSA (5- 50 GPa). The upper bound of AFM moduli in EICP-BSA samples is limited by tip calibration.

The low AFM moduli for the EICP-BSA are in agreement with the nanoindentation analyses (Figure 5.3). These low moduli occur despite the presence of calcite in the samples as indicated by XRD analyses, and thus indicate changes in the moduli of mineral precipitates due to presence of BSA. Although specific mechanisms for the low moduli in the presence of BSA

remain unclear, the possibility that the moduli are low due to the presence of intracrystalline BSA remains a strong possibility.

The ring structure observed in the topography maps of the precipitates in AFM phase diagram of EICP-BSA (Figure 5.7 C) is similar to ring structures observed in the BSE image analysis (Figure 5.2 D). The AFM phase diagrams are influenced by a complex set of topographical and compositional factors. The dark regions observed in phase diagrams are also the low moduli regions on modulus maps which indicate that factors other than topography, such as compositional or density differences, influence the high contrast in the ring structures in EICP-BSA precipitate (Figure 5.7 D). The formation of mineral growth rings in AICP-BSA and EICP-BSA precipitates observed in BSE images, and AFM phase maps are also imitations of lamellae formed in mussels and alternating layers of organics in the shell of pearl oysters (Wallis et al., 2022). Furthermore, the gradation in moduli of AICP-BSA and EICP-BSA is also reminiscent of the gradation of moduli in biogenic mineral precipitates where organics are present in biominerals (North et al., 2017).

While the material properties of these biominerals formed in the presence of BSA are incomparable to biogenic minerals in strength and stiffness, the outcomes of this study provide evidence that organics can be used to modify material properties of biominerals in ureolytically induced mineral precipitates. Optimization of the types of organics used and their concentrations can be used to develop not only structure-property relationships in such biominerals but also develop methods to manipulate microscale material properties for enhanced macroscale performance of biominerals in engineered applications as well design of biomineral aggregates with specific morphologies and material properties.

5.5 Conclusions

This work shows that BSA can alter the structural and material properties of biominerals. The abiotically and enzymatically induced calcium carbonate (AICP and EICP) precipitates formed in the presence of BSA (AICP-BSA and EICP-BSA) had smaller particle sizes as compared to the AICP and EICP formed without BSA. The AICP-BSA and EICP-BSA precipitates also exhibited density variations within the precipitates during backscattered imaging. The nanoscale structural heterogeneity in the precipitates was confirmed by AFM phase diagrams. The mineral precipitates in the presence of BSA had lower elastic moduli and hardness than their BSA-free counterparts in the absence of BSA. The lower moduli of abiotic and enzymatic precipitates were confirmed by AFM force mapping of the mineral precipitates. The low moduli regions in AFM maps also corresponded with the phase contrasts in AFM phase diagrams. Overall, these results indicate that morphology and material properties can be manipulated in ureolytically induced mineral precipitation through purposeful addition of organics. Further research in this area will support the advancement of biologically induced mineralization with higher control on mineral morphology and material properties to deliver macroscale toughness for engineering applications such as construction, binder and adhesive applications.

5.6 Acknowledgments

This research was made possible by the Department of Chemical and Biological Engineering and the Center for Biofilm Engineering at the Norm Asbjornson College of Engineering at Montana State University, a Ray and Erin Schultz Emerging Scholars Fellowship,

and the United States Education Foundation Pakistan Fulbright Commission. This work was also partially supported by the National Science Foundation (CMMI 20368687 to CH and RG and 1736255 to RG). This work represents the authors' views and opinions, and not necessarily those of the sponsors.

5.7 Supplemental Information

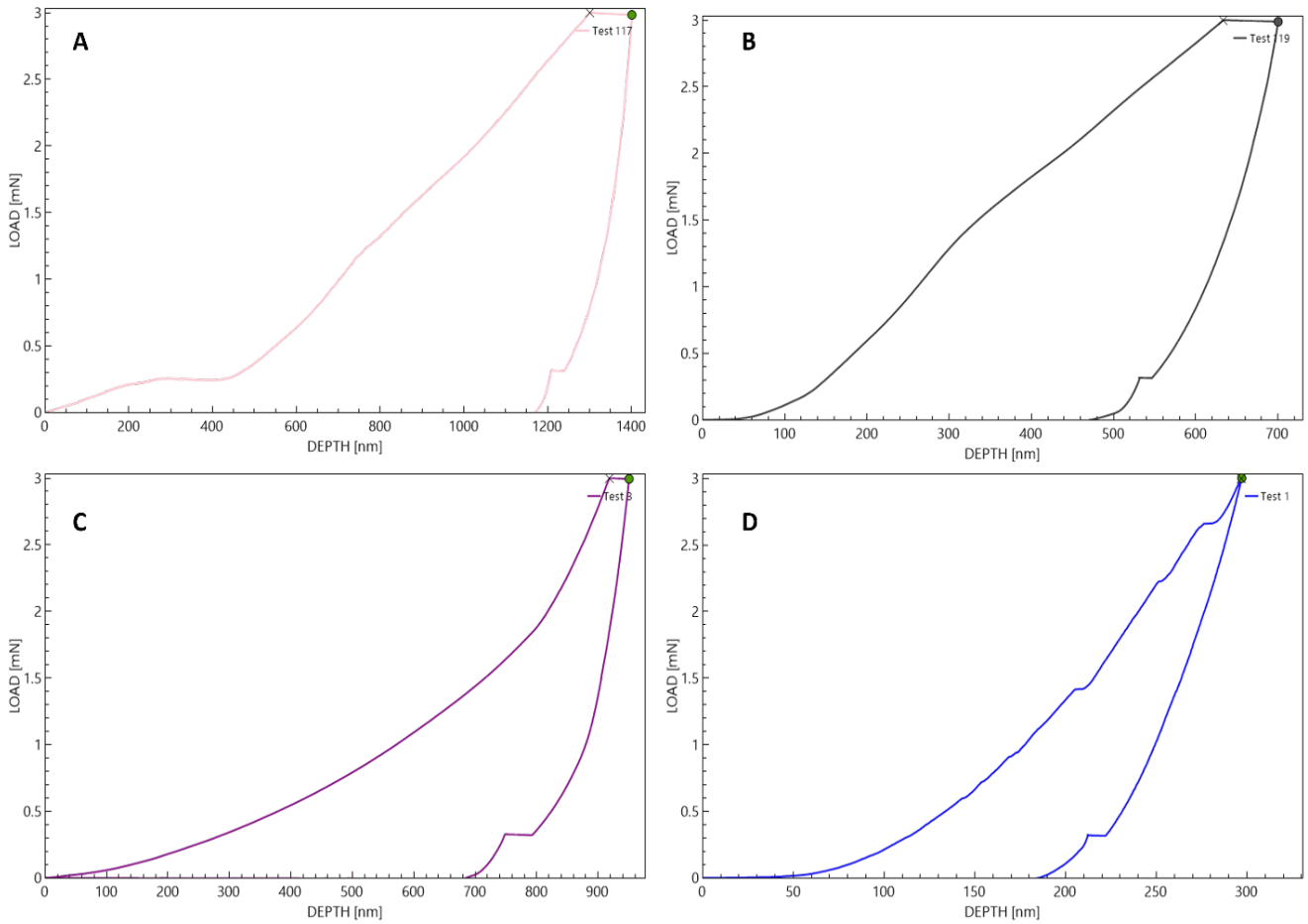

Figure 5.S1: Sample curves with representative effects of (A, B) strain hardening, (C) strain softening, and (D) porosity on the load depth profiles. (B) Stiffening in only the loading part of the curve indicates strain-hardening effects. (C) The load depth profile with a relatively long plateau in the early parts of the loading curve shows potential strain-softening effects. (D) The displacement bursts on the load depth profile indicative of pores in the mineral samples.

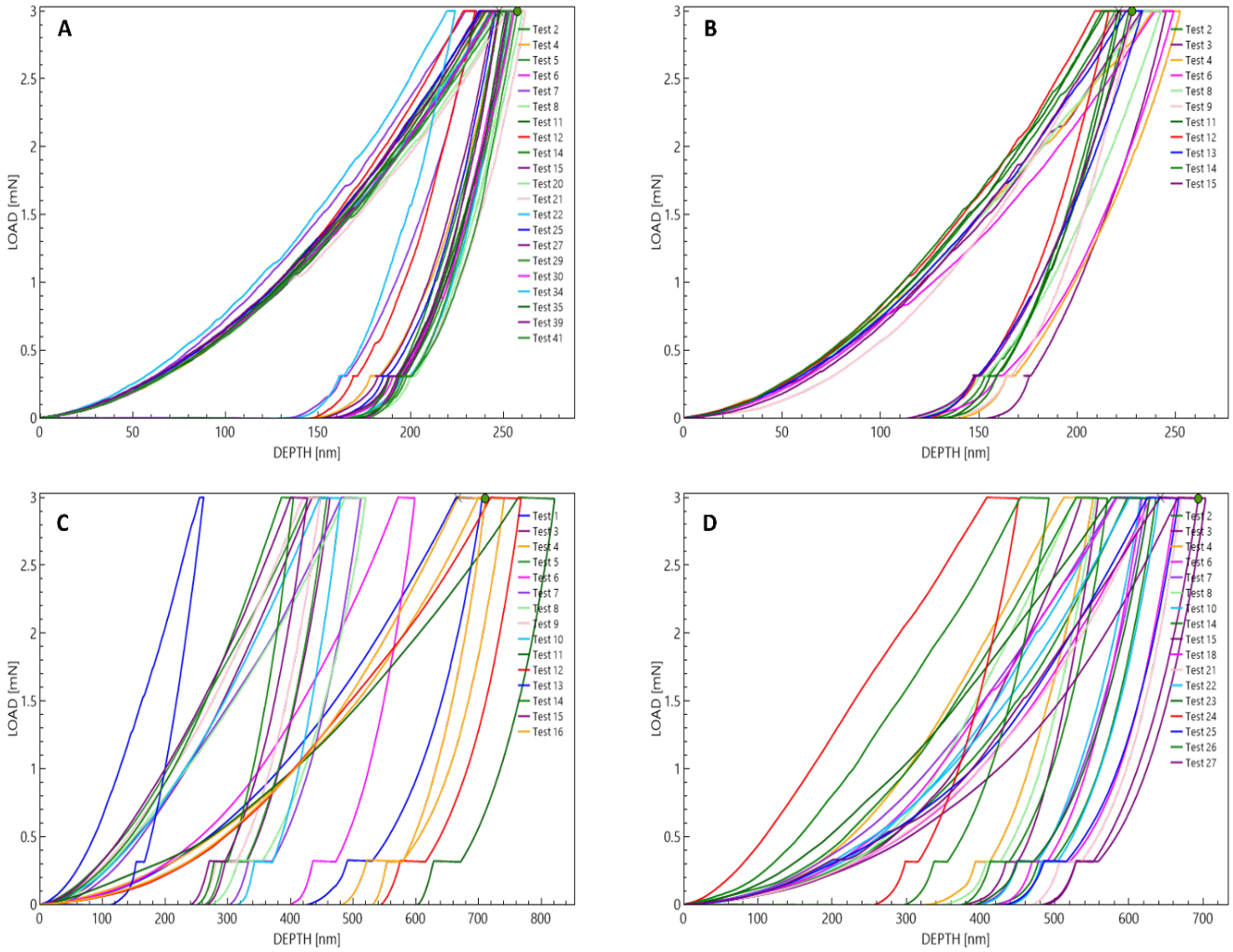

Figure 5.S 2: Example subsets of load depth profiles for (A) abiotically induced calcium carbonate precipitates (AICP), (B) enzymatically induced calcium carbonate precipitates (EICP), (C) AICP in BSA (AICP-BSA), and (D) EICP in BSA (EICP-BSA).

Table 5.S1: A two-factor ANOVA tested the effect of reaction type and BSA on the nanoindentation modulus (Ei) of the minerals. The nanoindentation modulus data was log-transformed to improve the normality and homoscedasticity of data.

Source	DF	Adj SS	Adj MS	F-Value	P-Value
Reaction	1	0.530	0.5300	0.49	0.491
Biopolymer	1	94.006	94.0059	86.19	0.000
Reaction*Biopolymer	1	1.973	1.9725	1.81	0.189
Error	29	31.628	1.0906		
Total	32	126.320			

Table 5.S2: A two-factor ANOVA tested the effect of reaction type and BSA on the nanoindentation hardness (H_i) in minerals. The nanoindentation hardness data was log-transformed to improve the normality and homoscedasticity of data.

Source	DF	Adj SS	Adj MS	F-Value	P-Value
Reaction	1	0.0391	0.0391	0.66	0.424
Biopolymer	1	21.3328	21.3328	358.79	0.000
Reaction*Biopolymer	1	0.7556	0.7556	12.71	0.001
Error	29	1.7243	0.0595		
Total	32	23.3676			

Table 5.S3: Tukey simultaneous tests for differences in interactions between the effect of reaction type and the presence of BSA on the H_i of the minerals.

Difference of Reaction *Biopolymer Levels	Difference of Means	SE of Difference	Simultaneous 95% CI	T-Value	Adjusted P Value
(AICP) -(AICP-BSA)	1.539	0.136	(1.168, 1.910)	11.29	0.000
(EICP-BSA) - (AICP-BSA)	-0.276	0.172	(-0.745, 0.194)	-1.60	0.395
(EICP) - (AICP)	0.438	0.102	(0.161, 0.714)	4.31	0.001
(EICP) - (EICP-BSA)	2.252	0.147	(1.853, 2.651)	15.37	0.000

Individual confidence level = 98.91%

Table 5.S4: A two factor ANOVA tested the effect of reaction type and BSA on the resistance to deformation (H_i /Ei) in minerals.

Source	DF	Adj SS	Adj MS	F-Value	P-Value
Reaction	1	112	112	0.01	0.936
Biopolymer	1	650723	650723	38.38	0.000
Reaction*Biopolymer	1	157653	157653	9.30	0.005
Error	29	491681	16955		
Total	32	1270565			

Table 5.S5: Tukey simultaneous tests for differences in interactions between the effect of reaction type and presence of BSA on the resistance to deformation (H_i /E_i) in minerals.

Difference of Reaction * Biopolymer Levels	Difference of Means	SE of Difference	Simultaneous 95% CI	T-Value	Adjusted P-Value
(AICP) - (AICP-BSA)	168.1	72.8	(-30.1,366.3)	2.31	0.119
(EICP-BSA) - (AICP-BSA)	-167.3	92.1	(-417.9, 83.4)	-1.82	0.286
(EICP) (AICP)	158.6	54.3	(10.9, 306.3)	2.92	0.032
(EICP) - (EICP-BSA)	494.0	78.2	(281.0, 707.0)	6.31	0.000

Table 5.S6: A two factor ANOVA tested the effect of reaction type and BSA on the log transformed AFM moduli of minerals.

Source	DF	Adj SS	Adj MS	F-Value	P-Value
Sample	1	0.1146	0.1146	1.73	0.214
BSA	1	10.2692	10.2692	154.60	0.000
Sample*BSA	1	0.0314	0.0314	0.47	0.505
Error	12	0.7971	0.0664		
Total	15	11.2123			

Table 5.S7: Tukey simultaneous tests for differences in interactions between the effect of reaction type and presence of BSA on the AFM moduli of minerals.

Difference of Sample*BSA Levels	Difference of Means	SE of Difference	Simultaneous 95% CI	T-Value	Adjusted P-Value
(AICP) - (AICP-BSA)	1.514	0.182	(0.972, 2.055)	8.31	0.000
(EICP-BSA) - (AICP-BSA)	0.081	0.182	(-0.461, 0.622)	0.44	0.970
(EICP) - (AICP)	0.258	0.182	(-0.283, 0.799)	1.42	0.514
(EICP) - (EICP-BSA)	1.691	0.182	(1.150, 2.232)	9.28	0.000

CHAPTER SIX

FUTURE CONSIDERATIONS FOR THE USE OF BIOMINERALIZATION IN THE DEVELOPMENT OF SUSTAINABLE ADHESIVES

Replacing hazardous chemicals and manufacturing processes with safer chemicals and greener technologies is a key investment toward sustainability and the health and safety of the environment, workers and consumers. While regulatory compliance limits the use of hazardous commercial adhesives, the use of hazardous reagents (e.g., isocyanates), which can have short- and long-term detrimental health effects, remains common in the production of adhesives (Marques et al., 2020). Petro-based adhesives with highly volatile organic compounds also remain persistent in the market (Kozicki & Guzik, 2021; Li et al., 2021; Tolls et al., 2016; Wilke et al., 2004). The demand for safer alternatives remains high, but the availability of alternatives is limited by their mechanical and adhesive performance (Bennett, 2012). The mechanical properties and adhesive performance of conventional petrochemical-derived adhesives have been well-established over several decades of research and advancement (Banea & Da Silva, 2009; Budhe et al., 2017; da Silva et al., 2018).

Biobased adhesives made by biopolymer and bioderived polymers are less established and remain limited to non-structural applications (Packham, 2009; Steven Abbott, 2019). Strategies such as the incorporation of nanoparticles or the microencapsulation of nanoparticles with hazardous but efficient cross-linkers have been some of the potential solutions to enable eco-friendly biobased structural adhesives (Helanto et al., 2021, 2022; Podlena et al., 2021; Qi et al., 2016; Sun et al., 2021). The use of nanoparticles as polymer fillers is not unique to biopolymers. These nanoparticle-based modifications and crosslinking reactions have been

common for synthetic and petrol-based polymers as well (Oliveira et al., 2018; Thorvaldsen et al., 2015; Tjong, 2006). Yet in the development of biopolymers, the goal is to minimize the use of hazardous or toxic reagents. The use of several bioinspired crosslinking strategies has been developed for biobased adhesives (Bukartyk et al., 2022; Cui et al., 2023; Ghahri et al., 2021), but these methods are biopolymer specific and may not be scalable.

An alternative method proposed in this work is the use of biomineralization in the development of biopolymer mineral composites and adhesives. Biomineralization in nature involves the formation of mineral precipitates by highly controlled cellular processes and their byproducts or passively due to interactions between microbial activities and organic contents and inorganics (Harris et al., 2017; Weiner, 2008). Biomineralization induced by ureolytic bacteria *Sporosarcina pasteurii* isolated from soil has been central to the advancements in the use of biominerals for engineering applications (Phillips et al., 2013; Zhu & Dittrich, 2016). The ureolytic reaction is a robust method for the formation of biominerals, which has been shown to be effective in surface and subsurface applications (Krajewska, 2018). Ureolytic biomineralization generally uses low-cost material and exhibits high rates of ureolysis, and therefore mineral precipitation, compared to other methods of biomineralization (Hammes & Verstraete, 2002; Ma et al., 2020). Ureolytically induced biomineralization does not involve any processing of minerals to bind with biopolymers or crosslinking reactions.

In nature, the ureolytic reaction occurs in the presence of a large variety of organic components, the most common sources are the local flora and fauna (Decho, 2010; Dhami et al., 2018). It is therefore reasonable to hypothesize that biomineralization can be compatible with a large range of biopolymers. In this work, the ureolytic reaction by *Sporosarcina pasteurii* and jack bean urease was carried out with two common biopolymers: soy- and gum-based products

for adhesives and food packaging films. Soy protein has been extensively researched for applications as a wood adhesive, whereas guar gum is common in the food packaging industry due to its high safety index. It is proposed here that biomineralization carried out in the presence of organics may offer a non-specific and transferrable method for the formation of biobased mineral composites.

For the development of viable options for sustainable adhesives, it is essential that the relevant process parameters are optimized. The ureolytically induced calcium carbonate precipitation (UICP) was carried out by *Sporosarcina pasteurii* and a jack bean meal-based cell-free urease source. The concentrations of the urease source were optimized for each biopolymer type, soy protein, and guar gum. It was found that the calcium concentrations in the formulations can be increased up to an optimal concentration for the highest adhesive strength of the composites, but beyond the optimal concentration, the adhesive strength of the composite suffers. Both *S. pasteurii* and jack bean urease-induced calcium carbonate precipitation (MICP and EICP respectively) in soy protein biopolymer delivered similar adhesive performance and reached up to 1.5 MPa adhesive strength on glass surfaces. The MICP-reinforced adhesives were also tested on stainless steel surfaces and showed adhesive strength of up to 1.9 MPa. In MICP and EICP-reinforced guar gum adhesives had 2.5x higher adhesive strength than the guar gum itself. The adhesive strength of the MICP and EICP-reinforced adhesives was more than 6x higher than for soy protein itself. Further research directed towards development of biomineral biopolymer adhesives needs to target adhesive-surface interactions and durability of the adhesives.

One of the key characteristics of the adhesive performance needed for product and process specification of biobased adhesives is the reporting of failure characteristics of the

adhesives (Banea & Da Silva, 2009). This implies the relationship between adhesion and/or cohesive strength must be substantiated by testing the performance of an adhesive in lap shear tests. The failure characteristics of MICP-reinforced adhesives were evaluated by image analysis of the bonded regions of a lapjoint after failure. The residual amount of composite on either side of the bonded region was used to determine the fraction of adhesive vs. cohesive failure. A significant fraction of failure in the composites was found to be of adhesive nature. Ideally, the preferred failure mode for composites is a cohesive failure to achieve the highest possible adhesive strength, where all the failure occurs within the composite and none at the interface of the bonded surfaces (da Silva et al., 2018; Frihart, 2010). Conventionally, surface pretreatments ensure the highest cohesive failure in adhesively bonded lapjoints (Marques et al., 2020). Optimization of surface pretreatments are needed to define pre-treatment parameters for bonding adhesives. In this work, only the characteristics of the composite itself were optimized.

Surface pretreatment studies should be carried out to support the next steps in the optimization of the UICP adhesives. By making evaluations based on cost, time and effectiveness of each treatment, there is a large range of surface preparation methods that can be selected based on the application needs and resource availability. One of the easiest surface preparation methods is mechanical roughening of surfaces, such as by manual roughening, sandblasting or similar; on the other hand, the most effective method for surface preparation for commercial adhesives is the use of plasma treatments (da Silva et al., 2018).

The optimization of adhesive development needs to be technically and environmentally competitive. This includes the determination of adhesive performance after application (Banea & Da Silva, 2009; Marques et al., 2020). The durability testing of the UICP-reinforced adhesives was carried out by testing the adhesively bonded lap joints after 24-hour immersion in deionized

water. In a 24-hour immersion test, it was determined that MICP-reinforced adhesives retained 81% of their adhesive strength after 24-hour immersion, while soy protein alone was solubilized within a few hours, and the bonded lapjoints deteriorated. It was also noticed here that while the adhesive strength of MICP and EICP-reinforced adhesives were similar in previous experiments, the EICP-reinforced adhesives exhibited a significantly lower water resistance and had no adhesive strength post 24-hour immersion.

Further durability testing of MICP-reinforced adhesives was carried out at 7-day immersion, relative humidity, and temperature exposures. It was found that the performance of the composites was reliable at room and below-freezing (-20˚C) temperatures but not at high temperatures (≥100˚C). Hence, the performance of the MICCs was maintained at low to moderate humidity of up to 50% for 7 days, but the lapjoint performance was severely compromised after 7-day exposures to 80% RH or full immersion in water. The XRD and TGA analyses showed that the low molecular weight organics and ammonium chloride salt in the composites disappeared from the adhesive during immersion. Furthermore, at high-temperature exposures (300˚C), lower organics and ammonium chloride were volatilized. The thermal and physical stability of the MICP-reinforced adhesives was potentially limited by the organics and highly soluble salts, like ammonium chloride. The biodegradability of the biobased composites can be valuable for some applications where biodegradability is desirable. e.g., in food packaging. One future consideration in improving the water resistance of MICP adhesives for longer exposure periods (greater than 24 hours) might be to lower the concentrations of soluble ammonium chloride. While 7-day exposures of MICP adhesives to 100˚C in this work lowered the adhesive strength of the composites, shorter high temperature exposures (>100˚C but ≤180˚C for 1 hour) have been shown to improve both the adhesive strength and water resistance of soy-

based adhesives (Frihart et al., 2016; Koshy et al., 2015; Vnučec et al., 2016). It would therefore be valuable to add a heat cure step for a few minutes to improve the adhesive strength and the water resistance of MICP-reinforced adhesives. Heat shock can cause damage in *S. pasteurii* cell integrity, which can release the intracellular urease enzyme and increase the efficiency of ureolysis (Akyel, 2022) The heat treatment of lapjoints as a curing step may have the additional benefit of lowering the curing time by evaporating water at high temperatures.

An important design consideration for a biomimetic synthesis of biominerals using biomineralization is the influence of organics on the structure and material properties of the resulting biominerals (Cranford et al., 2013; Deng & Li, 2021; Weiner, 2008). The interactions between organics and minerals during the biomineralization process are governed by a complex set of kinetic parameters that influence the crystallization of precipitates (Harris et al., 2017; Weiner & Dove, 2003; Williams, 1984). The microscale structure of the biominerals is central to the performance of biomineral composites in nature and for the synthesis of materials for engineering applications (Deng & Li, 2021; Labonte et al., 2017). Overall, the role of organics in ureolytic biomineralization is unexplored and unexploited. Very few studies have evaluated the use of organics as control parameters in UICP (Heveran et al., 2019; Xu et al., 2019), and structure-material property relationships in UICP have yet to be established. For the application of UICP-reinforced adhesives, it is very important to identify the control parameters to deliver reproducible structure and material properties in the biominerals.

For higher complexity systems with an abundance of organics, for example in microbially induced biomineralization which have organic-inorganic interfaces on the bacterial cell walls and produce extracellular polymeric substances, the cause-effect relationships for organic-mineral interactions are harder to pinpoint (Decho, 2010). For simplified organic-

mineral interaction dynamic, we tested the influence of the bovine serum albumin (BSA) biomacromolecule on the structure and material properties of calcium carbonate precipitates formed by cell-free enzyme suspension of jack bean urease. The enzymatically induced calcium carbonate precipitation was carried out independently and in the presence of BSA. In comparison, abiotic calcium carbonate precipitation was induced by mixing a solution of sodium bicarbonate and calcium chloride. The abiotic calcium carbonate precipitation was also carried out in the presence of BSA.

A unique feature of the mineral precipitates formed in the presence of BSA was their growth patterns that resembled those of geologic and biogenic biominerals. Since the organics from local flora and fauna have been a part of the co-evolution of mineralization in microbes and higher phyla of organisms (Dong et al., 2022), it is a reasonable outcome that an animal-based protein, BSA, induced structural features in biominerals that are similar to geologic calcite. The presence of BSA modified the structure as well as the material properties of the minerals. The nanoindentation moduli and hardness of AICP and EICP in the presence of BSA were lower than for AICP and EICP formed in the absence of BSA. The decrease in hardness and elastic moduli of the biominerals formed in the presence of BSA was non-linear, and the BSA based biominerals showed high resistance to inelastic deformation. The structural variations in the AICP-BSA and EICP-BSA precipitates also translated to submicron scale decrease in their moduli. It is known that microscale gradation in structure and moduli in biominerals is influenced by organics has been proposed to be responsible for toughening of biominerals from micro- to macro scales (Barthelat et al., 2016; Harris et al., 2017; Tjong, 2006). To develop outcome-focused advancements in the use of organics, the structure-material property

relationships at the microscale need to be further tested against their performance in engineered applications.

The outcomes of this study support the development of biomineral-based composite adhesives with a relatively simple process design. The design parameters optimized for UICP adhesives in this study include the urease source and mineral content of the composites. The microbially induced calcium carbonate composites had significantly higher water resistance than biopolymers alone and enzymatically induced calcium carbonate composites. Additionally, we identified factors associated with the durability of the UICP adhesives, which can support further research into the advancement of biomineralization-based adhesives. The presence of biomacromolecules such as soy protein and BSA during calcium carbonate precipitation have a demonstrated influence on the material properties of resulting composite adhesives and biominerals themselves. The effect of soy protein on the strength of the adhesive and the effect of BSA on the micro- and nano-scale structure of biominerals demonstrates that protein biomolecules can be used to alter the nanoscale structure and therefore, potentially the macroscale properties of the composites, too.

While many parameters can be further tested and optimized for biopolymer-biomineral adhesives, it is important to determine the application niche for these adhesives beyond this stage. The application of the composites determines appropriate testing methods beyond lap shear tests. Overall, biomineralization is a potentially highly adaptable method for the production of mineral based adhesives, and with the availability of organics as a control parameter toolbox, the possibilities are potentially unlimited.

REFERENCES CITED

Abramowitch, S., & Easley, D. (2016). Introduction to Classical Mechanics. *Biomechanics of the Female Pelvic Floor*, 89–107. https://doi.org/10.1016/B978-0-12-803228-2.00004-0

Adgate, J. L., Church, T. R., Ryan, A. D., Ramachandran, G., Fredrickson, A. L., Stock, T. H., Morandi, M. T., & Sexton, K. (2004). Outdoor, indoor, and personal exposure to VOCs in children. *Environmental Health Perspectives*, *112*(14), 1386–1392. https://doi.org/10.1289/EHP.7107

Adhesive and sealant demand worldwide 2019 | Statista. (n.d.). Retrieved September 28, 2022, from https://www.statista.com/statistics/533413/adhesive-and-sealant-demand-by-world-region/

Akyel, A. (2022). *Improving ph and temperature stability of urease for ureolysis-induced calcium carbonate precipitation by*.

Amenorfe, L. P., Agorku, E. S., Sarpong, F., & Voegborlo, R. B. (2022). Innovative exploration of additive incorporated biopolymer-based composites. In *Scientific African* (Vol. 17). Elsevier B.V. https://doi.org/10.1016/j.sciaf.2022.e01359

Arab, M. G., Alsodi, R., Almajed, A., Yasuhara, H., Zeiada, W., & Shahin, M. A. (2021). State-of-the-art review of enzyme-induced calcite precipitation (Eicp) for ground improvement: Applications and prospects. In *Geosciences (Switzerland)* (Vol. 11, Issue 12). MDPI. https://doi.org/10.3390/geosciences11120492

Arias, J. L., & Fernández, M. S. (2008). Polysaccharides and proteoglycans in calcium carbonate-based Biomineralization. *Chemical Reviews*, *108*(11), 4475–4482. https://doi.org/10.1021/cr078269p

Azeredo, H. M. C., & Waldron, K. W. (2016). Crosslinking in polysaccharide and protein films and coatings for food contact – A review. *Trends in Food Science & Technology*, *52*, 109–122. https://doi.org/10.1016/J.TIFS.2016.04.008

Azulay, D., Abbasi, R., Ktorza, I., Rememnnik, S., Reddy, A., & Chai, L. (2018). Biopolymers from a Bacterial Extracellular Matrix Affect the Morphology and Structure of Calcium Carbonate Crystals _ Enhanced Reader. *Crystal Growth and Design*, *18*, 5582–5591.

Bahrig, L., Hickey, S. G., & Eychmüller, A. (2014). Mesocrystalline materials and the involvement of oriented attachment-a review. In *CrystEngComm* (Vol. 16, Issue 40, pp. 9408–9424). Royal Society of Chemistry. https://doi.org/10.1039/c4ce00882k

Banea, M. D., & Da Silva, L. F. M. (2009). Adhesively bonded joints in composite materials: An overview. In *Proceedings of the Institution of Mechanical Engineers, Part L: Journal of Materials: Design and Applications* (Vol. 223, Issue 1, pp. 1–18). https://doi.org/10.1243/14644207jmda219

Baranwal, J., Barse, B., Fais, A., Delogu, G. L., & Kumar, A. (2022). Biopolymer: A Sustainable Material for Food and Medical Applications. *Polymers 2022, Vol. 14, Page 983*, *14*(5), 983. https://doi.org/10.3390/POLYM14050983

Bar-Cohen, Y. (2012). *Biomimetics: Nature-Based Innovation* (1st ed.). CRC Press.

Barthelat, F., Yin, Z., & Buehler, M. J. (2016). Structure and mechanics of interfaces in biological materials. In *Nature Reviews Materials* (Vol. 1). Nature Publishing Group. https://doi.org/10.1038/natrevmats.2016.7

Bennett, S. J. (2012). Implications of climate change for the petrochemical industry: Mitigation measures and feedstock transitions. In *Handbook of Climate Change Mitigation* (Vol. 1, pp. 319–357). Springer US. https://doi.org/10.1007/978-1-4419-7991-9_10

Benning, L. G., & Waychunas, G. A. (2008). *Nucleation, Growth, and Aggregation of Mineral Phases: Mechanisms and Kinetic Controls*. https://escholarship.org/uc/item/3r85p9qq

Bovone, G. ;, Dudaryeva, O. Y. ;, Marco-Dufort, B. ;, Tibbitt, M., Bovone, G., Dudaryeva, O. Y., Marco-Dufort, B., & Tibbitt, M. W. (2021). Engineering Hydrogel Adhesion for Biomedical Applications. *Cite This: ACS Biomater. Sci. Eng*, *7*, 4048–4076. https://doi.org/10.3929/ethz-b-000508687

Budhe, S., Banea, M. D., de Barros, S., & da Silva, L. F. M. (2017). An updated review of adhesively bonded joints in composite materials. *International Journal of Adhesion and Adhesives*, *72*, 30–42. https://doi.org/10.1016/j.ijadhadh.2016.10.010

Bukartyk, M., Zholobko, O., & Wu, X. F. (2022). Green Synthesis of Soy Protein Nanocomposites: Effects of Cross-Linking and Clay Nanoparticles on the Mechanical Performance. *ACS Omega*, *7*(7), 5883–5893. https://doi.org/10.1021/acsomega.1C06002

Çalık, A. (2016). Effect Of Adherend Shape On Stress Concentration Reduction Of Adhesively Bonded Single Lap Joint. In *Engineering Review* (Vol. 36).

Cao, J., Jin, S., Li, C., & Li, J. (2021). Bioinspired mineral–organic hybridization strategy to produce a green high performance soybean meal based adhesive. *Journal of Cleaner Production*, *299*, 126939. https://doi.org/10.1016/j.jclerpro2021.126939

Cheng, Y. T., & Cheng, C. M. (1998). Relationships between hardness, elastic modulus, and the work of indentation. *Applied Physics Letters*, *73*(5), 614–616. https://doi.org/10.1063/1.121873

Chen, L., Gu, Z., Li, L., Lei, W., Rong, Q., Zhao, C., Wu, Q., Gu, Z., Jin, X., Jiang, L., & Liu, M. (2018). Integration of hydrogels with functional nanoparticles using hydrophobic comb-like polymers as an adhesive layer. *Journal of Materials Chemistry A*, *6*(31), 15147–15153. https://doi.org/10.1039/c8ta02970a

Chen, S., Shi, S. Q., Zhou, W., & Li, J. (2022). Developments in Bio-Based Soy Protein Adhesives: A Review. *Macromolecular Materials and Engineering*, *307*(10), 2200277. https://doi.org/10.1002/mame.202200277

Cho, K. R., Kulshreshtha, P., Wu, K. J., Seto, J., Qiu, S. R., & De Yoreo, J. J. (2019). *The effects of different types of additives on growth of biomineral phases investigated by in situ atomic force microscopy*.

Chow, W. S., Ishak, Z. A. M., Ishiaku, U. S., Karger-Kocsis, J., & Apostolov, A. A. (2004). The effect of organoclay on the mechanical properties and morphology of injection-molded polyamide 6/polypropylene nanocomposites. *Journal of Applied Polymer Science*, *91*(1), 175–189. https://doi.org/10.1002/app.13244

Côté, A. S., Darkins, R., & Duffy, D. M. (2015). Deformation twinning and the role of amino acids and magnesium in calcite hardness from molecular simulation. *Physical Chemistry Chemical Physics*, *17*(31), 20178–20184. https://doi.org/10.1039/c5cp03370e

Cranford, S. W., De Boer, J., Van Blitterswijk, C., & Buehler, M. J. (2013). Materiomics: An -omics approach to biomaterials research. In *Advanced Materials* (Vol. 25, Issue 6, pp. 802–824). https://doi.org/10.1002/adma.201202553

Cui, Z., Xu, Y., Sun, G., Peng, L., Li, J., Luo, J., & Gao, Q. (2023). Improving Bond Performance and Reducing Cross-Linker Dosage of Soy Protein Adhesive via Hyper-Branched and Organic–Inorganic Hybrid Structures. *Nanomaterials*, *13*(1). https://doi.org/10.3390/nano13010203

Da Silva, L. F. M., Öchsner, A., & Adams, R. D. (n.d.). *Handbook of Adhesion Technology*.

da Silva, L. F. M., Öchsner, A., & Adams, R. D. (Eds.). (2018). *Handbook of Adhesion Technology*. Springer International Publishing. https://doi.org/10.1007/978-3-319-55411-2

Decho, A. W. (2010). Overview of biopolymer-induced mineralization: What goes on in biofilms? *Ecological Engineering*, *36*(2), 137–144. https://doi.org/10.1016/j.ecoleng.2009.01.003

Deng, Z., Chen, H., Yang, T., Jia, Z., Weaver, J. C., Shevchenko, P. D., De Carlo, F., Mirzaeifar, R., & Li, L. (2020). Strategies for simultaneous strengthening and toughening via nanoscopic intracrystalline defects in a biogenic ceramic. *Nature Communications*, *11*(1). https://doi.org/10.1038/s41467-020-19416-2

Deng, Z., Jia, Z., & Li, L. (2022). Biomineralized Materials as Model Systems for Structural Composites: Intracrystalline Structural Features and Their Strengthening and Toughening Mechanisms. In *Advanced Science* (Vol. 9, Issue 14). John Wiley and Sons Inc. https://doi.org/10.1002/advs.202103524

Deng, Z., & Li, L. (2021). Intrinsic Mechanical Properties of Individual Biogenic Mineral Units in Biomineralized Skeletons. *ACS Biomaterials Science and Engineering*. https://doi.org/10.1021/acsbiomaterials.0c01587

De Yoreo, J. (2020). A perspective on multistep pathways of nucleation. In *ACS Symposium Series* (Vol. 1358, pp. 1–17). American Chemical Society. https://doi.org/10.1021/bk-2020-1358.ch001

De Yoreo, J. J. (2003). Principles of Crystal Nucleation and Growth. *Reviews in Mineralogy and Geochemistry*, *54*(1), 57–93. https://doi.org/10.2113/0540057

Dhami, N. K., Mukherjee, A., & Watkin, E. L. J. (2018). Microbial diversity and mineralogical-mechanical properties of calcitic cave speleothems in natural and in vitro biomineralization conditions. *Frontiers in Microbiology*, *9*(FEB). https://doi.org/10.3389/fmicb.2018.00040

Díez-Pascual, A. M. (2022). Biopolymer Composites: Synthesis, Properties, and Applications. In *International Journal of Molecular Sciences* (Vol. 23, Issue 4). MDPI. https://doi.org/10.3390/ijms23042257

Dinte, E., & Sylvester, B. (2018). Adhesives: Applications and Recent Advances. In *Applied Adhesive Bonding in Science and Technology*. InTech. https://doi.org/10.5772/intechopen.71854

Dong, H., Huang, L., Zhao, L., Zeng, Q., Liu, X., Sheng, Y., Shi, L., Wu, G., Jiang, H., Li, F., Zhang, L., Guo, D., Li, G., Hou, W., & Chen, H. (2022). A critical review of mineral-microbe interaction and co-evolution: mechanisms and applications. In *National Science Review* (Vol. 9, Issue 10). Oxford University Press. https://doi.org/10.1093/nsr/nwac128

Du, Z., Mo, J., Zhang, Y., & Xu, Q. (2014). Benzene, toluene and xylenes in newly renovated homes and associated health risk in Guangzhou, China. *Building and Environment*, *72*, 75–81. https://doi.org/10.1016/j.buildenv.2013.10.013

Ebnesajjad, S. (2010). Introduction and Adhesion Theories. In *Handbook of Adhesives and Surface Preparation: Technology, Applications and Manufacturing* (pp. 3–13). Elsevier. https://doi.org/10.1016/B978-1-4377-4461-3.10001-X

Epa, U., & Environments Division, I. (1991). *Indoor Air Facts No. 4 Sick Building Syndrome*.

Evans, E., & Ritchie, K. (1997). Dynamic strength of molecular adhesion bonds. *Biophys. J.*, *72*(4), 1541–1555. https://doi.org/10.1016/s0006-3495(97)78802-7

Evans, J. (2017). Polymorphs, Proteins, and Nucleation Theory: A Critical Analysis. *Minerals*, *7*(4), 62. https://doi.org/10.3390/min7040062

Evans, J. S. (2017). Polymorphs, proteins, and nucleation theory: A critical analysis. *Minerals*, *7*(4). https://doi.org/10.3390/min7040062

Falini, G., & Fermani, S. (2013). The strategic role of adsorption phenomena in biomineralization. *Crystal Research and Technology*, *48*(10), 864–876. https://doi.org/10.1002/crat.201200711

Feder, M. J., Akyel, A., Morasko, V. J., Gerlach, R., & Phillips, A. J. (2021). Temperature-dependent inactivation and catalysis rates of plant-based ureases for engineered biomineralization. *Engineering Reports*, *3*(2). https://doi.org/10.1002/eng2.12299

Finney, A. R., Innocenti Malini, R., Freeman, C. L., & Harding, J. H. (2020). Amino Acid and Oligopeptide Effects on Calcium Carbonate Solutions. *Crystal Growth and Design*, *20*(5), 3077–3092. https://doi.org/10.1021/acs.cgd.9b01693

Frey, S. E., Destaillats, H., Cohn, S., Ahrentzen, S., & Fraser, M. P. (2014). Characterization of indoor air quality and resident health in an Arizona senior housing apartment building. *J. Air Waste Manag. Assoc.*, *64*(11), 1251–1259. https://doi.org/10.1080/10962247.2014.937513

Frihart, C. (2010). Part 2 Biobased Adhesives and Non-conventional Bonding.

Frihart, C. R. (2015). Introduction to Special Issue: Wood Adhesives: Past, Present, and Future. *Forest Products Journal*, *65*(1–2), 4–8. https://doi.org/10.13073/65.1-2.4

Frihart, C. R., Coolidge, T., Mock, C., & Valle, E. (2016). High bonding temperatures greatly improve soy adhesivewet strength. *Polymers*, *8*(11). https://doi.org/10.3390/polym8110394

F. Song, H. Koo, & D. Ren. (2015). Effects of material properties on bacterial adhesion and biofilm formation. *Journal of Dental Research*, *94*(8), 1027–1034. https://doi.org/10.1177/0022034515587690

Fukuzaki, S., Urano, H., & Nagata, K. (1995). Adsorption of Protein onto Stainless-Steel Surfaces. In *Journal Of Fermentation And Bioengineering* (Vol. 80, Issue 1).

Fu, S. Y., Feng, X. Q., Lauke, B., & Mai, Y. W. (2008). Effects of particle size, particle/matrix interface adhesion and particle loading on mechanical properties of particulate-polymer composites. *Composites Part B: Engineering*, *39*(6), 933–961. https://doi.org/10.1016/j.compositesb.2008.01.002

Gale, J. D., & Achuthan, A. (2014). The effect of work-hardening and pile-up on nanoindentation measurements. *Journal of Materials Science*, *49*(14), 5066–5075. https://doi.org/10.1007/s10853-014-8213-4

Gao, H. (2007). Application of fracture mechanics concepts to hierarchical biomechanics of bone and bone-like materials. In *Advances in Fracture Research* (pp. 101–137). Springer Netherlands. https://doi.org/10.1007/978-1-4020-5423-5_8

George, R. P., Muraleedharan, P., Sreekumari, K. R., & Khatak, H. S. (2003). Influence of surface characteristics and microstructure on adhesion of bacterial cells onto a type 304 stainless steel. *Biofouling*, *19*(1), 1–8. https://doi.org/10.1080/08927010290031017

Ghahri, S., Chen, X., Pizzi, A., Hajihassani, R., Papadopoulos, A. N., & Magalhães, D. (2021). *Natural Tannins as New Cross-Linking Materials for Soy-Based Adhesives*. https://doi.org/10.3390/polym13040595

Giuffre, A. J., Hamm, L. M., Han, N., De Yoreo, J. J., & Dove, P. M. (2013). Polysaccharide chemistry regulates kinetics of calcite nucleation through competition of interfacial energies. *Proceedings of the National Academy of Sciences of the United States of America*, *110*(23), 9261–9266. https://doi.org/10.1073/pnas.1222162110

Görgen, S., Benzerara, K., Skouri-Panet, F., Gugger, M., Chauvat, F., & Cassier-Chauvat, C. (2021). The diversity of molecular mechanisms of carbonate biomineralization by bacteria. *Discover Materials*, *1*(1). https://doi.org/10.1007/s43939-020-00001-9

Green Buildings at EPA | US EPA. (1991) Retrieved November 7, 2022, from https://www.epa.gov/greeningepa/green-buildings-epa

Guangyan, Q. N. L. D. W. X. S. S. (2016). Development of High-Strength Soy Protein Adhesives Modified with Sodium Montmorillonite Clay. *Journal of Oil Chemists' Society*, *93*(11), 1509–1517.

Guchait, A., Saxena, A., Chattopadhyay, S., & Mondal, T. (2022). Influence of Nanofillers on Adhesion Properties of Polymeric Composites. In *ACS Omega* (Vol. 7, Issue 5, pp. 3844–3859). American Chemical Society. https://doi.org/10.1021/acsomega.1c05448

Guessasma, S., Benseddiq, N., & Lourdin, D. (2010). Effective Young's modulus of biopolymer composites with imperfect interface. *International Journal of Solids and Structures*, *47*(18–19), 2436–2444. https://doi.org/10.1016/j.ijsolstr.2010.05.002

Guhra, T., Ritschel, T., & Totsche, K. U. (2019). Formation of mineral–mineral and organo–mineral composite building units from microaggregate-forming materials including microbially produced extracellular polymeric substances. *European Journal of Soil Science*, *70*(3), 604–615. https://doi.org/10.1111/ejss.12774

Hammes, F., & Verstraete, W. (2002). Key roles of pH and calcium metabolism in microbial carbonate precipitation. *Reviews in Environmental Science and Biotechnology 2002 1:1*, *1*(1), 3–7. https://doi.org/10.1023/A:1015135629155

Harris, J., Böhm, C. F., & Wolf, S. E. (2017). Universal structure motifs in biominerals: A lesson from nature for the efficient design of bioinspired functional materials. In *Interface Focus* (Vol. 7, Issue 4). Royal Society. https://doi.org/10.1098/rsfs.2016.0120

Hazrati, S., Rostami, R., Farjaminezhad, M., & Fazlzadeh, M. (2016). Preliminary assessment of BTEX concentrations in indoor air of residential buildings and atmospheric ambient

air in Ardabil, Iran. *Atmospheric Environment*, *132*, 91–97. https://doi.org/10.1016/J.ATMOSENV.2016.02.042

Heinrich, L. A. (2019). Future opportunities for bio-based adhesives-advantages beyond renewability. In *Green Chemistry* (Vol. 21, Issue 8, pp. 1866–1888). Royal Society of Chemistry. https://doi.org/10.1039/c8gc03746a

Helanto, K., Talja, R., & Rojas, O. J. (2021). Effects of talc, kaolin and calcium carbonate as fillers in biopolymer packaging materials. *Journal of Polymer Engineering*, *41*(9), 746–758. https://doi.org/10.1515/POLYENG-2021-0076

Helanto, K., Talja, R., & Rojas, O. J. (2022). Mineral-filled biopolyester coatings for paperboard packaging materials: Barrier, sealability, convertability and biodegradability properties. *Nordic Pulp and Paper Research Journal*, *37*(1), 212–221. https://doi.org/10.1515/NPPRJ-2021-0076

Hettiarachchy, N. S., Kalapathy, U., & Myers, D. J. (1995). Alkali-modified soy protein with improved adhesive and hydrophobic properties. *Journal of the American Oil Chemists' Society*, *72*(12), 1461–1464. https://doi.org/10.1007/BF02577838

Heveran, C. M., Liang, L., Nagarajan, A., Hubler, M. H., Gill, R., Cameron, J. C., Cook, S. M., & Srubar, W. V. (2019). Engineered Ureolytic Microorganisms Can Tailor the Morphology and Nanomechanical Properties of Microbial-Precipitated Calcium Carbonate. *Scientific Reports*, *9*(1). https://doi.org/10.1038/s41598-019-51133-9

Higham, T. E., Russell, A. P., Niewiarowski, P. H., Wright, A., & Speck, T. (2019). The Ecomechanics of Gecko Adhesion: Natural Surface Topography, Evolution, and Biomimetics. *Integrative and Comparative Biology*, *59*(1), 148–167. https://doi.org/10.1093/icb/icz013

Ho~evar, M., Jenko, M., Godec, M., & Drobne, D. (2014). An overview of the influence of stainless-steel surface properties on bacterial adhesion. *Materials and Technology*, *48*(5), 609–617

Höfer, R., Avtar S, M., & Zhanrong, Z. (2019). Green Chemistry for Surface Coatings, Inks and Adhesives. *Green Chemistry Book Series*, P001-430. https://doi.org/10.1039/9781788012997%0Ahttp://ebook.rsc.org/?DOI=10.1039/9781788012997

Hoffmann, T. D., Reeksting, B. J., & Gebhard, S. (2021). Bacteria-induced mineral precipitation: A mechanistic review. *Microbiology (United Kingdom)*, *167*(4). https://doi.org/10.1099/mic.0.001049

Hun, D. E., Siegel, J. A., Morandi, M. T., Stock, T. H., & Corsi, R. L. (2009). Cancer risk disparities between hispanic and non-hispanic white populations: The role of exposure to indoor air pollution. *Environmental Health Perspectives*, *117*(12), 1925–1931. https://doi.org/10.1289/EHP.0900925

Imam, S. H., Bilbao-Sainz, C., Chiou, B. Sen, Glenn, G. M., & Orts, W. J. (2013). Biobased adhesives, gums, emulsions, and binders: Current trends and future prospects. *Journal of Adhesion Science and Technology*, *27*(18–19), 1972–1997. https://doi.org/10.1080/01694243.2012.696892

Jensen, A., Lim, L. T., Barbut, S., & Marcone, M. (2015). Development and characterization of soy protein films incorporated with cellulose fibers using a hot surface casting technique. *LWT*, *60*(1), 162–170. https://doi.org/10.1016/j.lwt.2014.09.027

Kang, H., Song, X., Wang, Z., Zhang, W., Zhang, S., & Li, J. (2016). High-Performance and Fully Renewable Soy Protein Isolate-Based Film from Microcrystalline Cellulose via Bio-Inspired Poly(dopamine) Surface Modification. *ACS Sustainable Chemistry and Engineering*, *4*(8), 4354–4360. https://doi.org/10.1021/acsuschemeng.6b00917

Kim, S., Regitsky, A. U., Song, J., Ilavsky, J., McKinley, G. H., & Holten-Andersen, N. (2021). In situ mechanical reinforcement of polymer hydrogels via metal-coordinated crosslink mineralization. *Nature Communications 2021 12:1*, *12*(1), 1–10. https://doi.org/10.1038/s41467-021-20953-7

Kim, Y. Y., Carloni, J. D., Demarchi, B., Sparks, D., Reid, D. G., Kunitake, M. E., Tang, C. C., Duer, M. J., Freeman, C. L., Pokroy, B., Penkman, K., Harding, J. H., Estroff, L. A., Baker, S. P., & Meldrum, F. C. (2016). Tuning hardness in calcite by incorporation of amino acids. *Nature Materials*, *15*(8), 903–910. https://doi.org/10.1038/nmat4631

Kleber, M., Bourg, I. C., Coward, E. K., Hansel, C. M., Myneni, S. B., & Nunan, N. (2021). Dynamic interactions at the mineral-organic matter interface. *Nature Reviews Earth & Environment*, *2*, 402–421. https://doi.org/10.1038/s43017-021-00162-yï

Kleber, M., Mikutta, R., Torn, M. S., & Jahn, R. (2005). Poorly crystalline mineral phases protect organic matter in acid subsoil horizons. *European Journal of Soil Science*, *56*(6), 717–725. https://doi.org/10.1111/j.1365-2389.2005.00706.x

Koshy, R. R., Mary, S. K., Thomas, S., & Pothan, L. A. (2015). Environment friendly green composites based on soy protein isolate - A review. *Food Hydrocolloids*, *50*, 174–192. https://doi.org/10.1016/j.foodhyd.2015.04.023

Kozicki, M., & Guzik, K. (2021). Comparison of VOC Emissions Produced by Different Types of Adhesives Based on Test Chambers. *Materials*, *14*(8). https://doi.org/10.3390/ma14081924

Krajewska, B. (2018). Urease-aided calcium carbonate mineralization for engineering applications: A review. In *Journal of Advanced Research* (Vol. 13, pp. 59–67). Elsevier B.V. https://doi.org/10.1016/j.jare.2017.10.009

Kunitake, M. E., Mangano, L. M., Peloquin, J. M., Baker, S. P., & Estroff, L. A. (2013). Evaluation of strengthening mechanisms in calcite single crystals from mollusk shells. *Acta Biomaterialia*, *9*(2), 5353–5359. https://doi.org/10.1016/j.actbio.2012.09.030

Labonte, D., Lenz, A. K., & Oyen, M. L. (2017). On the relationship between indentation hardness and modulus, and the damage resistance of biological materials. *Acta Biomaterialia*, *57*, 373–383. https://doi.org/10.1016/j.actbio.2017.05.034

Lamaming, S. Z., Lamaming, J., Rawi, N. F. M., Hashim, R., Kassim, M. H. M., Hussin, M. H., Bustami, Y., Sulaiman, O., Amini, M. H. M., & Hiziroglu, S. (2021). Improvements and limitation of soy protein-based adhesive: A review, *61*(10), 2393–2405. https://doi.org/10.1002/PEN.25782

Lauchnor, E. G., Topp, D. M., Parker, A. E., & Gerlach, R. (2015). Whole cell kinetics of ureolysis by Sporosarcina pasteurii. *Journal of Applied Microbiology*, *118*(6), 1321–1332. https://doi.org/10.1111/jam.12804

Lee, Y. S., & Park, W. (2018). Current challenges and future directions for bacterial self-healing concrete. In *Applied Microbiology and Biotechnology* (Vol. 102, Issue 7, pp. 3059–3070). Springer Verlag. https://doi.org/10.1007/s00253-018-8830-y

Leong, Y. W., Abu Bakar, M. B., Ishak, Z. A. M., Ariffin, A., & Pukanszky, B. (2004). *Comparison of the Mechanical Properties and Interfacial Interactions Between Talc, Kaolin, and Calcium Carbonate Filled Polypropylene Composites*. https://doi.org/10.1002/app.13542

Li, A., Jia, Y., Sun, S., Xu, Y., Minsky, B. B., Stuart, M. A. C., Cölfen, H., Von Klitzing, R., & Guo, X. (2018). Mineral-Enhanced Polyacrylic Acid Hydrogel as an Oyster-Inspired Organic-Inorganic Hybrid Adhesive. *ACS Applied Materials and Interfaces*, *10*(12), 10471–10479. https://doi.org/10.1021/acsami.8b01082

Li, A. J., Pal, V. K., & Kannan, K. (2021). A review of environmental occurrence, toxicity, biotransformation and biomonitoring of volatile organic compounds. *Environmental Chemistry and Ecotoxicology*, *3*, 91–116. https://doi.org/10.1016/J.ENCECO.2021.01.001

Li, H., Wang, Y., Xie, W., Tang, Y., Yang, F., Gong, C., Wang, C., Li, X., & Li, C. (2023). Preparation and Characterization of Soybean Protein Adhesives Modified with an Environmental-Friendly Tannin-Based Resin. *Polymers*, *15*(10). https://doi.org/10.3390/polym15102289

Li, K., Jin, S., Li, X., Li, J., Shi, S. Q., & Li, J. (2021). Bioinspired interface engineering of soybean meal-based adhesive incorporated with biomineralized cellulose nanofibrils and a functional aminoclay. *Chemical Engineering Journal*, *421*. https://doi.org/10.1016/j.cej.2021.129820

Li, K., Jin, S., Zeng, G., Zhou, Y., Zhang, F., Li, J., Shi, S. Q., & Li, J. (2022). Biomimetic development of a strong, mildew-resistant soy protein adhesive via mineral–organic system and phenol-amine synergy. *Industrial Crops and Products*, *187*. https://doi.org/10.1016/j.indcrop.2022.115412

Liu, D., Chen, H., Chang, P. R., Wu, Q., Li, K., & Guan, L. (2010). Biomimetic soy protein nanocomposites with calcium carbonate crystalline arrays for use as wood adhesive. *Bioresource Technology*, *101*(15), 6235–6241. https://doi.org/10.1016/j.biortech.2010.02.107

Liu, K. K., & Oyen, M. L. (2014). Nanobiomechanics of living materials. In *Interface Focus* (Vol. 4, Issue 2). Royal Society. https://doi.org/10.1098/rsfs.2014.0001

Liu, X. yang, Xu, D. ping, Li, S. jun, Qiu, S. li, & Jiang, Q. (2023). An Insight into the Mechanical and Fracture Characterization of Minerals and Mineral Interfaces in Granite Using Nanoindentation and Micro X-Ray Computed Tomography. *Rock Mechanics and Rock Engineering*. https://doi.org/10.1007/s00603-023-03221-6

Lutz, T. M., Kimna, C., Casini, A., & Lieleg, O. (2022). Bio-based and bio-inspired adhesives from animals and plants for biomedical applications. *Materials Today Bio*, *13*, 100203. https://doi.org/10.1016/J.MTBIO.2022.100203

Ma, L., Pang, A. P., Luo, Y., Lu, X., & Lin, F. (2020). Beneficial factors for biomineralization by ureolytic bacterium Sporosarcina pasteurii. *Microbial Cell Factories*, *19*(1). https://doi.org/10.1186/s12934-020-1281-z

Marques, A. C., Mocanu, A., Tomić, N. Z., Balos, S., Stammen, E., Lundevall, A., Abrahami, S. T., Günther, R., de Kok, J. M. M., & de Freitas, S. T. (2020). Review on adhesives and surface treatments for structural applications: Recent developments on sustainability and implementation for metal and composite substrates. In *Materials* (Vol. 13, Issue 24, pp. 1–43). MDPI AG. https://doi.org/10.3390/ma13245590

Metzler, R. A., Rist, R., Alberts, E., Kenny, P., & Wilker, J. J. (2016). Composition and Structure of Oyster Adhesive Reveals Heterogeneous Materials Properties in a Biological Composite. *Advanced Functional Materials*, *26*(37), 6814–6821. https://doi.org/10.1002/adfm.201602348

Mitchell, A. C., Espinosa-Ortiz, E. J., Parks, S. L., Phillips, A. J., Cunningham, A. B., & Gerlach, R. (2019). Kinetics of calcite precipitation by ureolytic bacteria under aerobic and anaerobic conditions. *Biogeosciences*, *16*(10), 2147–2161. https://doi.org/10.5194/bg-16-2147-2019

Mitchell, A. C., & Grant Ferris, F. (2006). The influence of bacillus pasteurii on the nucleation and growth of calcium carbonate. *Geomicrobiology Journal*, *23*(3–4), 213–226. https://doi.org/10.1080/01490450600724233

Miyake, M., Kim, D., & Hata, T. (2022). Casein-assisted enhancement of the compressive strength of biocemented sand. *Scientific Reports*, *12*(1). https://doi.org/10.1038/s41598-022-16879-9

Morasko, V. J. (2018). Kinetics Of Thermally Inactiavted Ureases and Management Of Sand Production Through Ureolysis-Induced Mineral Precipitation.

Murugan, R., Suraishkumar, G. K., Mukherjee, A., & Dhami, N. K. (2021). Insights into the influence of cell concentration in design and development of microbially induced calcium carbonate precipitation (MICP) process. *PLoS ONE*, *16*(7). https://doi.org/10.1371/journal.pone.0254536

Nepal, D., Kang, S., Adstedt, K. M., Kanhaiya, K., Bockstaller, M. R., Brinson, L. C., Buehler, M. J., Coveney, P. V., Dayal, K., El-Awady, J. A., Henderson, L. C., Kaplan, D. L., Keten, S., Kotov, N. A., Schatz, G. C., Vignolini, S., Vollrath, F., Wang, Y., Yakobson, B. I., … Heinz, H. (2023). Hierarchically structured bioinspired nanocomposites. In *Nature Materials* (Vol. 22, Issue 1, pp. 18–35). Nature Research. https://doi.org/10.1038/s41563-022-01384-1

Newcomb, C. J., Qafoku, N. P., Grate, J. W., Bailey, V. L., & De Yoreo, J. J. (2017). Developing a molecular picture of soil organic matter–mineral interactions by quantifying organo–mineral binding. *Nature Communications*, *8*(1), 396. https://doi.org/10.1038/s41467-017-00407-9

North, L., Labonte, D., Oyen, M. L., Coleman, M. P., Caliskan, H. B., & Johnston, R. E. (2017). Interrelated chemical-microstructural-nanomechanical variations in the structural units of the cuttlebone of Sepia officinalis. *APL Materials*, *5*(11). https://doi.org/10.1063/1.4993202

Nudelman, F., & Sommerdijk, N. A. J. M. (2012). Biomineralization as an inspiration for materials chemistry. In *Angewandte Chemie - International Edition* (Vol. 51, Issue 27, pp. 6582–6596). https://doi.org/10.1002/anie.201106715

Oliveira, A. D. de, Beatrice, C. A. G., Oliveira, A. D. de, & Beatrice, C. A. G. (2018). Polymer Nanocomposites with Different Types of Nanofiller. *Nanocomposites - Recent Evolutions*. https://doi.org/10.5772/INTECHOPEN.81329

Oliver, W. C., & Pharr, G. M. (1992). An improved technique for determining hardness and elastic modulus using load and displacement sensing indentation experiments. *Journal of Materials Research*, *7*(6), 1564–1583. https://doi.org/10.1557/jmr.1992.1564

Oni, O. V., Lawrence, M. A., Zappi, M. E., & Chirdon, W. M. (2023). A Review of Strategies to Enhance the Water Resistance of Green Wood Adhesives Produced from Sustainable Protein Sources. *Sustainability*, *15*(20), 14779. https://doi.org/10.3390/su152014779

Otsu, N. (1979). A Threshold Selection Method from Gray Level Histograms. *IEEE Transactions on Systems, Man, and Cybernetics*, *9*(1), 62–66. https://doi.org/10.1109/TSMC.1979.4310076

Packham, D. E. (2009). Adhesive technology and sustainability. *International Journal of Adhesion and Adhesives*, *29*(3), 248–252. https://doi.org/10.1016/j.ijadhadh.2008.06.002

Pang, H., Ma, C., Shen, Y., Sun, Y., Li, J., Zhang, S., Cai, L., & Huang, Z. (2021). Novel Bionic Soy Protein-Based Adhesive with Excellent Prepressing Adhesion, Flame Retardancy, and Mildew Resistance. *ACS Applied Materials and Interfaces*, *13*(32), 38732–38744. https://doi.org/10.1021/acsami.1c11004

Parija, S., Misra, M., & Mohanty, A. K. (2001). Studies of natural gum adhesive extracts: An overview. In *Journal of Macromolecular Science - Reviews in Macromolecular Chemistry and Physics* (Vol. 41, Issue 3, pp. 175–197). Marcel Dekker Inc. https://doi.org/10.1081/mc-100107775

Parks, S. L. (2009).Kinetics of Calcite Precipitation By Ureolytic Bacteria Under Aerobic And Anaerobic Conditions.

Patel, A. K., Mathias, J. D., & Michaud, P. (2013). Polysaccharides as adhesives: A critical review. *Reviews of Adhesion and Adhesives*, *1*(3), 312–345. https://doi.org/10.7569/RAA.2013.097310

Peng, X., Zhang, B., Wang, Z., Su, W., Niu, S., Han, Z., & Ren, L. (2022). Bioinspired Strategies for Excellent Mechanical Properties of Composites. *Journal of Bionic Engineering 2022 19:5*, *19*(5), 1203–1228. https://doi.org/10.1007/S42235-022-00199-9

Phillips, A. J., Gerlach, R., Lauchnor, E., Mitchell, A. C., Cunningham, A. B., & Spangler, L. (2013). Engineered applications of ureolytic biomineralization: A review. In *Biofouling* (Vol. 29, Issue 6, pp. 715–733). https://doi.org/10.1080/08927014.2013.796550

Piekarska, K., Piorkowska, E., & Bojda, J. (2017). The influence of matrix crystallinity, filler grain size and modification on properties of PLA/calcium carbonate composites. *Polymer Testing*, *62*, 203–209. https://doi.org/10.1016/j.polymertesting.2017.06.025

Podlena, M., Böhm, M., Saloni, D., Velarde, G., & Salas, C. (2021). Tuning the adhesive properties of soy protein wood adhesives with different coadjutant polymers, nanocellulose and lignin. *Polymers*, *13*(12). https://doi.org/10.3390/polym13121972

Pokroy, B., Kapon, M., Marin, F., Adir, N., & Zolotoyabko, E. (2007). Protein-induced, previously unidentified twin form of calcite. *PNAS*, *104*(18).

Possinger, A. R., Zachman, M. J., Enders, A., Levin, B. D. A., Muller, D. A., Kourkoutis, L. F., & Lehmann, J. (2020). Organo–organic and organo–mineral interfaces in soil at the nanometer scale. *Nature Communications*, *11*(1). https://doi.org/10.1038/s41467-020-19792-9

Post, W., Kuijpers, L. J., Zijlstra, M., van der Zee, M., & Molenveld, K. (2021). Effect of mineral fillers on the mechanical properties of commercially available biodegradable polymers. *Polymers*, *13*(3), 1–14. https://doi.org/10.3390/polym13030394

Qi, G., Li, N., Wang, D., & Sun, X. S. (2016). Development of High-Strength Soy Protein Adhesives Modified with Sodium Montmorillonite Clay. *JAOCS, Journal of the*

American Oil Chemists' Society, *93*(11), 1509–1517. https://doi.org/10.1007/s11746-016-2890-x

Rabiei, M., Palevicius, A., Dashti, A., Nasiri, S., Monshi, A., Vilkauskas, A., & Janusas, G. (2020). Measurement modulus of elasticity related to the atomic density of planes in unit cell of crystal lattices. *Materials*, *13*(19), 1–17. https://doi.org/10.3390/ma13194380

Raydan, N. D. V., Leroyer, L., Charrier, B., & Robles, E. (2021). Recent Advances on the Development of Protein-Based Adhesives for Wood Composite Materials—A Review. *Molecules*, *26*(24), 7617. https://doi.org/10.3390/molecules26247617

Reddy, M. S. B., Ponnamma, D., Choudhary, R., & Sadasivuni, K. K. (2021). A Comparative Review of Natural and Synthetic Biopolymer Composite Scaffolds. *Polymers 2021, Vol. 13, Page 1105*, *13*(7), 1105. https://doi.org/10.3390/polym13071105

Risan, J., Jain, G., Pendola, M., & Evans, J. S. (2018). Intracrystalline incorporation of nacre protein hydrogels modifies the mechanical properties of calcite crystals: A microcompression study. *Journal of Materials Chemistry B*, *6*(25), 4191–4196. https://doi.org/10.1039/c8tb01156g

Rybicka-Jasińska, K., Derr, J. B., & Vullev, V. I. (2021). What defines biomimetic and bioinspired science and engineering? *Pure and Applied Chemistry*, *93*(11), 1275–1292. https://doi.org/10.1515/pac-2021-0323

Sadasivuni, K. K., Saha, P., Adhikari, J., Deshmukh, K., Ahamed, M. B., & Cabibihan, J. J. (2020). Recent advances in mechanical properties of biopolymer composites: a review. In *Polymer Composites* (Vol. 41, Issue 1, pp. 32–59). John Wiley and Sons Inc. https://doi.org/10.1002/pc.25356

Sand, K. K., Friddle, R. W., & Deyoreo, J. J. (2017). Quantifying the free energy landscape between polymers and minerals. *Scientific Reports 2017 7:1*, *7*(1), 1–5. https://doi.org/10.1038/s41598-017-09041-3

Segura González, E. A., Olmos, D., González-Gaitano, G., Orgaz, B., & González-Benito, J. (2015). Effect of kaolin nanofiller and processing conditions on the structure, morphology, and biofilm development of polylactic acid. *Journal of Applied Polymer Science*, *132*(42). https://doi.org/10.1002/app.42676

Shuai, J., Kim, S., Ryu, H., Park, J., Lee, C. K., Kim, G. B., Ultra, V. U., & Yang, W. (2018). Health risk assessment of volatile organic compounds exposure near Daegu dyeing industrial complex in South Korea. *BMC Public Health*, *18*(1). https://doi.org/10.1186/S12889-018-5454-1

Sierra-Romero, A., & Chen, B. (2018). Strategies for the preparation of polymer composites with complex alignment of the dispersed phase. In *Nanocomposites* (Vol. 4, Issue 4, pp. 137–155). Bellwether Publishing, Ltd. https://doi.org/10.1080/20550324.2018.1551830

Singh, Y., Kumar, J., Singh, I., & Rakesh, P. K. (2022). Joining behavior of natural fiber reinforced polymer composites. *Joining Processes for Dissimilar and Advanced Materials*, 33–63. https://doi.org/10.1016/B978-0-323-85399-6.00018-7

Steven Abbott, S. S. (2019). *Green Chemistry for Surface Coatings, Inks and Adhesives* (R. Höfer, A. S. Matharu, & Z. Zhang, Eds.; Vol. 60). Royal Society of Chemistry. https://doi.org/10.1039/9781788012997

Strange, D. G. T., & Oyen, M. L. (2011). Biomimetic bone-like composites fabricated through an automated alternate soaking process. *Acta Biomaterialia*, *7*(10), 3586–3594. https://doi.org/10.1016/j.actbio.2011.06.025

Sun, Z., Sun, B., Bai, Y., & Gao, Z. (2021). Economical improvement on the performances of a soybean flour-based adhesive for wood composites via montmorillonite hybridization. *Composites Part B: Engineering*, *217*. https://doi.org/10.1016/j.compositesb.2021.108920

Thorvaldsen, T., Johnsen, B. B., Olsen, T., & Hansen, F. K. (2015). *Investigation of Theoretical Models for the Elastic Stiffness of Nanoparticle-Modified Polymer Composites*. https://doi.org/10.1155/2015/281308

Tjong, S. C. (2006). Structural and mechanical properties of polymer nanocomposites. *Materials Science and Engineering R: Reports*, *53*(3–4), 73–197. https://doi.org/10.1016/J.MSER.2006.06.001

Tolls, J., Gómez, D., Guhl, W., Funk, T., Seger, E., & Wind, T. (2016). Estimating emissions from adhesives and sealants uses and manufacturing for environmental risk assessments. *Integrated Environmental Assessment and Management*, *12*(1), 185–194. https://doi.org/10.1002/IEAM.1662

Tripathi, J., Ambolikar, R., Gupta, S., Jain, D., Bahadur, J., & Variyar, P. S. (2019). Methylation of guar gum for improving mechanical and barrier properties of biodegradable packaging films. *Scientific Reports 2019 9:1*, *9*(1), 1–9. https://doi.org/10.1038/s41598-019-50991-7

U.S. Adhesives And Sealants Market Size Report, 2022-2030. (n.d.). Retrieved November 15, 2022, from https://www.grandviewresearch.com/industry-analysis/us-adhesives-sealants-market-report

Van De Locht, R. (2014). On The Nanostructure Of Biogenic And Bio-inspired Calcium Carbonate *As studied by electron microscopy techniques.*

van Wylick, A., Monclaro, A. V., Elsacker, E., Vandelook, S., Rahier, H., de Laet, L., Cannella, D., & Peeters, E. (2021). A review on the potential of filamentous fungi for microbial self-healing of concrete. *Fungal Biology and Biotechnology*, *8*(1), 1–12. https://doi.org/10.1186/S40694-021-00122-7/

Van Wylick, A., Monclaro, A. V., Elsacker, E., Vandelook, S., Rahier, H., De Laet, L., Cannella, D., & Peeters, E. (2021). A review on the potential of filamentous fungi for microbial self-healing of concrete. *Fungal Biology and Biotechnology*, *8*(1), 1–12. https://doi.org/10.1186/S40694-021-00122-7/

v. Knorre, H., & Krumbein, W. E. (2000). Bacterial Calcification. *Microbial Sediments*, 25–31. https://doi.org/10.1007/978-3-662-04036-2_4

Vnučec, D., Kutnar, A., & Goršek, A. (2016). Soy-based adhesives for wood-bonding – a review. *31*(8), 910–931. https://doi.org/10.1080/01694243.2016.1237278

Vodyashkin, A. A., Kezimana, P., Vetcher, A. A., & Stanishevskiy, Y. M. (2022). Biopolymeric Nanoparticles–Multifunctional Materials of the Future. In *Polymers* (Vol. 14, Issue 11). MDPI. https://doi.org/10.3390/polym14112287

Wallis, D., Harris, J., Böhm, C. F., Wang, D., Zavattieri, P., Feldner, P., Merle, B., Pipich, V., Hurle, K., Leupold, S., Hansen, L. N., Marin, F., & Wolf, S. E. (2022). Progressive changes in crystallographic textures of biominerals generate functionally graded ceramics. *Materials Advances*, *3*(3), 1527–1538. https://doi.org/10.1039/d1ma01031j

Wang, H., Alfredsson, V., Tropsch, J., Ettl, R., & Nylander, T. (2013). Formation of CaCO3 deposits on hard surfaces - Effect of bulk solution conditions and surface properties. *ACS Applied Materials and Interfaces*, *5*(10), 4035–4045. https://doi.org/10.1021/am401348v

Wang, R., Zheng, S., & Zheng, Y. (2011). *Polymer matrix composites and technology*. Woodhead Pub.

Wang, Y., Sun, X. S., & Wang, D. (2007). Effects of preheating treatment on thermal property and adhesion performance of soy protein isolates. *Journal of Adhesion Science and Technology*, *21*(15), 1469–1481. https://doi.org/10.1163/156856107782844756

Wang, Z., Chen, Y., Chen, S., Chu, F., Zhang, R., Wang, Y., & Fan, D. (2019). Preparation and characterization of a soy protein-based bio-adhesive crosslinked by waterborne epoxy resin and polyacrylamide. *RSC Advances*, *9*(60), 35273. https://doi.org/10.1039/C9RA05931H

Weiner, S. (2008). Biomineralization: A structural perspective. In *Journal of Structural Biology* (Vol. 163, Issue 3, pp. 229–234). https://doi.org/10.1016/j.jsb.2008.02.001

Weiner, S., & Dove, P. M. (2003). An Overview of Biomineralization Processes and the Problem of the Vital Effect. *Reviews in Mineralogy and Geochemistry*, *54*(1), 1–29. https://doi.org/10.2113/0540001

Wickliffe, J. K., Stock, T. H., Howard, J. L., Frahm, E., Simon-Friedt, B. R., Montgomery, K., Wilson, M. J., Lichtveld, M. Y., & Harville, E. (2020). Increased long-term health risks attributable to select volatile organic compounds in residential indoor air in southeast

Louisiana. *Scientific Reports 2020 10:1*, *10*(1), 1–12. https://doi.org/10.1038/s41598-020-78756-7

Wilke, O., Jann, O., & Brödner, D. (2004). VOC- and SVOC-emissions from adhesives, floor coverings and complete floor structures. *Indoor Air, Supplement*, *14*(8), 98–107. https://doi.org/10.1111/J.1600-0668.2004.00314.X

Williams, R. J. P. (1984). An Introduction to Biominerals and the Role of Organic Molecules in Their Formation (Vol. 304, Issue 1121).

Wolkoff, P. (1998). Impact of air velocity, temperature, humidity, and air on long-term VOC emissions from building products. *Atmospheric Environment*, *32*(14–15), 2659–2668. https://doi.org/10.1016/S1352-2310(97)00402-0

Wu, Y., Li, H., & Li, Y. (2021). Biomineralization induced by cells of sporosarcina pasteurii: Mechanisms, applications and challenges. In *Microorganisms* (Vol. 9, Issue 11). MDPI. https://doi.org/10.3390/microorganisms9112396

Xiong, R., Grant, A. M., Ma, R., Zhang, S., & Tsukruk, V. V. (2018). Naturally-derived biopolymer nanocomposites: Interfacial design, properties and emerging applications. In *Materials Science and Engineering R: Reports* (Vol. 125, pp. 1–41). Elsevier Ltd. https://doi.org/10.1016/j.mser.2018.01.002

Xu, W., Liu, H., Lou, Y., Jin, W., Xue, X., Liu, X., & Yang, N. (2019). Biomimetic mineralisation of calcium carbonate using xanthan gum as morphology control agent. *Micro and Nano Letters*, *14*(6), 642–644. https://doi.org/10.1049/mnl.2018.5235

Xu, X., Hu, W., Ke, Q., Liu, H., Li, J., & Zhao, Y. (2020). Bio-adhesives from unfolded soy protein reinforced by nano-chitosan for sustainable textile industry. *Textile Research Journal*, *90*(9–10), 1094–1101. https://doi.org/10.1177/0040517519886560

Yang, R., Zhang, T., Jiang, P., & Bai, Y. (2008). Experimental verification and theoretical analysis of the relationships between hardness, elastic modulus, and the work of indentation. *Applied Physics Letters*, *92*(23). https://doi.org/10.1063/1.2944138

Yu, X., & Jiang, J. (2018). Mineralization and cementing properties of bio-carbonate cement, bio-phosphate cement, and bio-carbonate/phosphate cement: a review. In *Environmental Science and Pollution Research* (Vol. 25, Issue 22, pp. 21483–21497). Springer Verlag. https://doi.org/10.1007/s11356-018-2143-7

Zhu, J., Wong, S. L., & Cakmak, S. (2013). Nationally representative levels of selected volatile organic compounds in Canadian residential indoor air: population-based survey. *Environ. Sci. Technol.*, *47*(23), 13276–13283. https://doi.org/10.1021/es403055e

Zhu, T., & Dittrich, M. (2016). Carbonate precipitation through microbial activities in natural environment, and their potential in biotechnology: A review. In *Frontiers in*

Bioengineering and Biotechnology (Vol. 4, Issue JAN). Frontiers Media S.A. https://doi.org/10.3389/fbioe.2016.00004

APPENDICES

APPENDIX A

SPATIO-TEMPORAL PROFILE OF CALCIUM CARBONATE MINERALS IN *SPOROSARCINA PASTEURII* BIOFILMS

The goal of this study was to determine the spatial distribution of calcium carbonate minerals in biofilms, and the effect of calcium carbonate minerals on biofilm formation.

Methods

Sporosarcina pasteurii biofilms were grown in drip flow reactors at a flow rate of 1ml/min, at 30˚C for 48 hours, the biofilm growth was promoted in two stages, batch phase of 6 hours and continuous flow for 42 hours.

To carry out fluorescence microscopy of biofilms were stained with SYTO9 and propidium iodide (Live/Dead stain). Green (SYTO9) indicates cells with intact cell membranes (‘Live’), while red (propidium iodide) indicates cells with compromised cell membranes or extracellular DNA (‘Dead’). Reflection (white) was used for minerals. The Images were acquired on a Leica TCS SP5 II confocal laser scanning microscope.

For critical point drying, biofilm samples were sequentially dehydrated in 25, 50, 75, 95 and 100% ethanol and critical point dried using a Tousimis Samdri-795 critical point drier. Topographical Images were acquired using a Zeiss SUPRA 55VP Field Emission Scanning Electron Microscope.

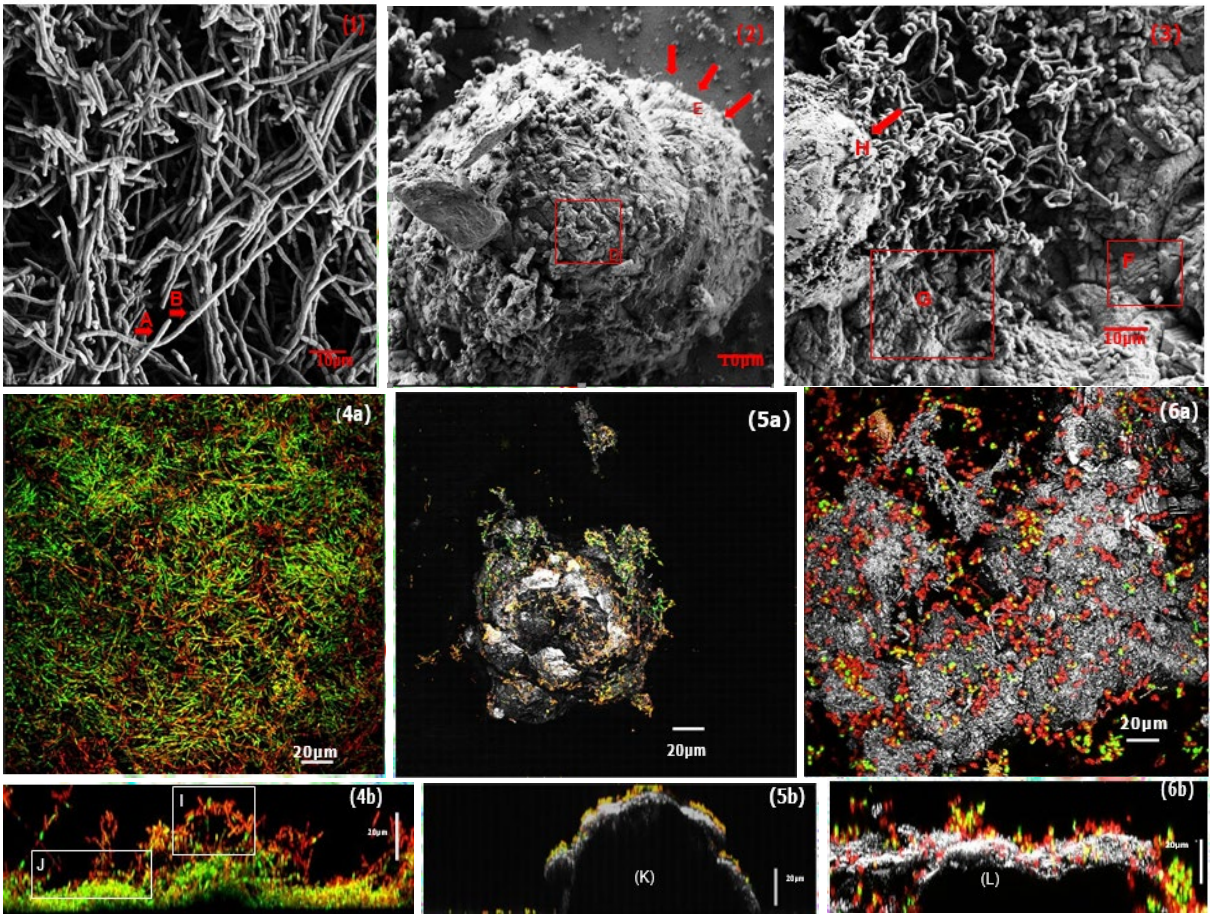

Figure A 1: Field Emission Scanning Electron Microscopy of biofilms. (1) Biofilms grown in the absence of calcium (and therefore minerals) consist of chains of bacteria. Elongated cells (A, B) can be seen actively dividing to form chains of cells. (2) Biofilms grown in the presence of calcium during continuous flow show cells associated with minerals. A few cells appear to have minerals associated with cell walls (D), indicating that these might have been sites for nucleation. (3) In biofilms formed in the presence of calcium in both batch and continuous flow, chains of bacterial cells as well as cells growing on the surface of minerals can be seen, while some cells are entombed in the mineral (F). Mineral morphology appears to be amorphous (G) and vaterite-like (H). Confocal Laser Scanning Microscopy shows 3D images of biofilms without minerals. (4a) Biofilms formed without mineral precipitates show the distribution of viable and non-viable cells. The cells are connected end to end forming chain like structures, shown in previous work in the lab as well (Schultz et al., 2011). (4b) The cross-section of the biofilm shows higher numbers of non-viable cells (I) on the surface while viable cells (J) appear to be more prominent at the bottom of the biofilm. (5a) 3D image of biofilm formed in the presence of calcium only in continuous flow shows cell attached to the surface of minerals which form a dome-like structure. (5b) In the cross section the dome structure appears to be hollow (K) due to the opacity of the mineral which limits the penetration of light into the sample. (6a) 3D image of biofilm formed in the presence of calcium throughout the batch and continuous phase. Image 6b shows a vertical cross-section of the biofilm. The bottom of the biofilm appears hollow due to limited penetration of light through the mineral (L).

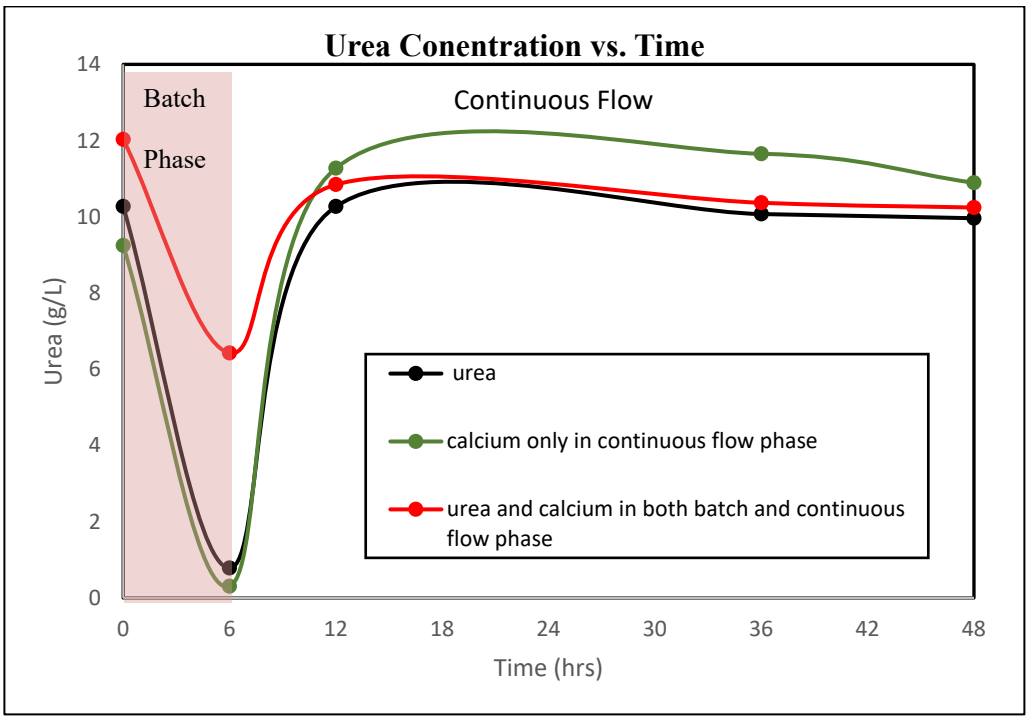

Figure A 2: The change in urea concentration in the drip flow reactors with *S.pasteurii* growth in continuous flow drip flow reactor over time. The data is shown for ureolysis in the presence of urea only (●) urea and calcium added to continuous growth phase (●), and urea and calcium added in both the batch and continuous growth phase (●).

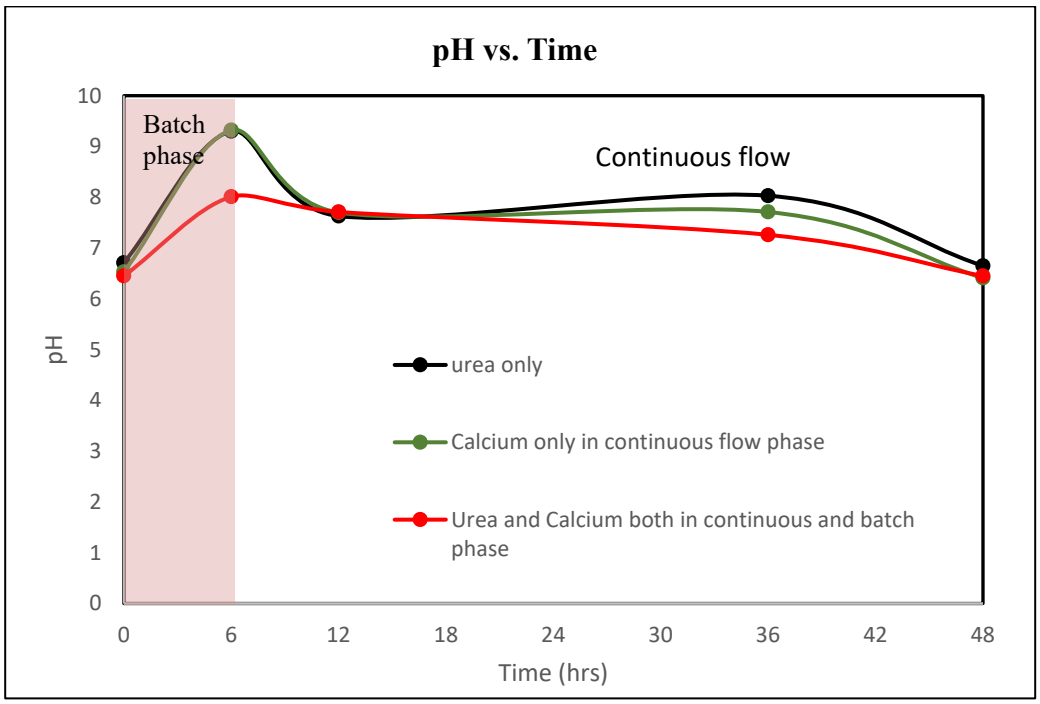

Figure A 3: The change in pH in the drip flow reactors with *S.pasteurii* growth in continuous flow drip flow reactor over time. The data is shown for ureolysis in the presence of urea only (●) urea and calcium added to continuous growth phase (●), and urea and calcium added in both the batch and continuous growth phase (●)

Concluding Remarks

The spatial organization of cells varies depending on the presence or absence of calcium the presence or absence of calcium in the batch phase affects mineral morphology under continuous flow. Future work will focus on the effect of these minerals on the mechanical properties of the biofilms.

APPENDIX B

BIOMINERALIZATION IN 3D PRINTED HYDROGELS

A PEGDA hydrogel containing *E.coli* cells was 3D printed using a Forman Lab2 3D printer. The 20mm x 2mm hydrogel was placed in a Drip Flow Reactor setup described in Appendix A. LB medium containing urea and calcium (0.33M in 1:1 ratios) was dripped into the drip flow channels to promote bacterial growth and induce mineral precipitation. The reactor was run for 24 hours and then the hydrogel was observed under the confocal microscope.

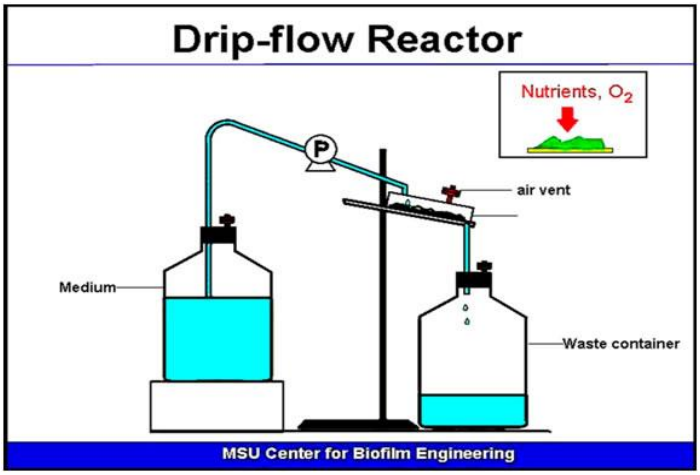

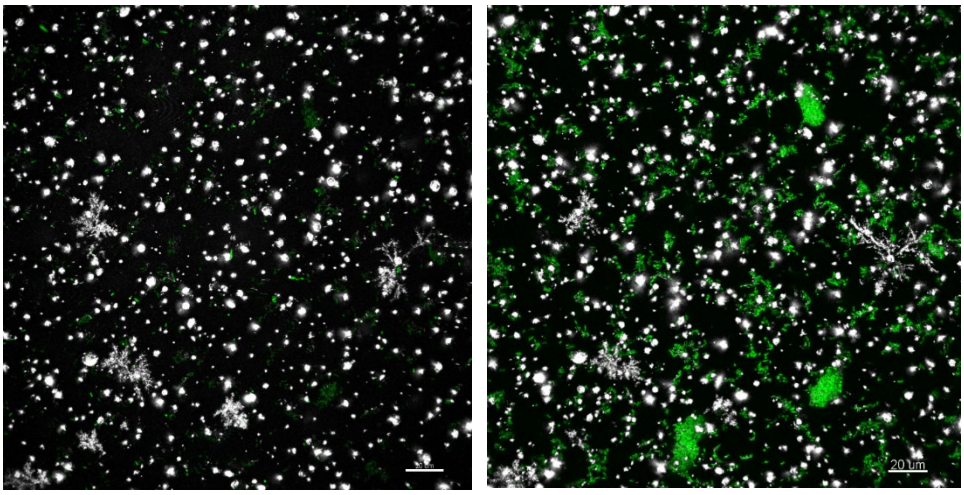

Figure B 1: A confocal laser scanning microscope was used to observe hydrogel in reflection mode where (white) mineral precipitates can be observed against the (black) hydrogel background. The *E.coli* bacterial cells carried the green fluorescent protein (gfp) gene. The scale bars represent 20µm length scale. It was noted that the cell clusters do not always align with areas of mineral precipitation, indicating that the carbonate ions may travel some distance from the cell before mineral precipitation occurs.

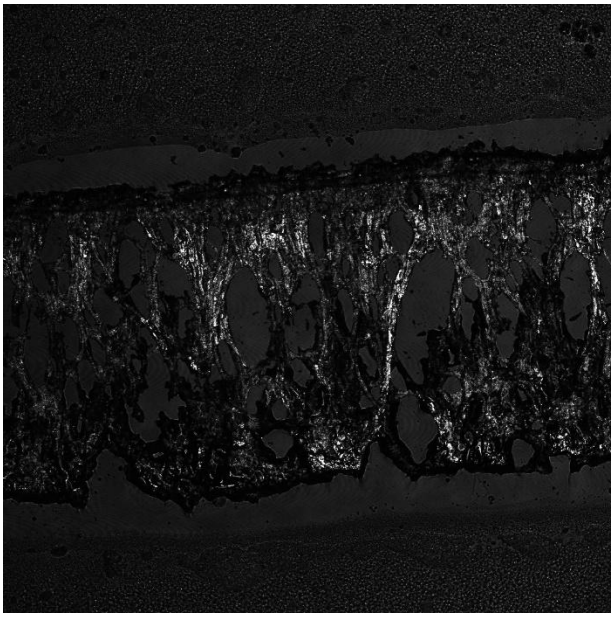

Figure B 2: Reflection and transmission overlay image of a vertical section of hydrogel. A 5-7µm thick cryosection of the hydrogel observed under the confocal laser scanning microscope. Reflection imaging was used to identify mineral-rich regions in the hydrogels. The string-like structures observed vertically indicate freezing and dehydration artifacts introduced in the samples. The height of the hydrogel was measured to be 800µm on average.

The mineral precipitates (Figure B2) appear to be spread throughout the hydrogel, and thus calcium is available throughout the hydrogel (because without calcium the mineral precipitates could not form). Also, ureolysis appears to be occurring throughout the hydrogel because ureolysis provides the second component (CO_3^{2-}) necessary for calcium carbonate precipitation. The top (oxic) and bottom (relatively anoxic regions) of hydrogels have similar mineral aggregate distribution. Experiments conducted by Tobler et al. show that the rates of ureolysis in *S.pasteurii* and therefore their calcite precipitation potential remains similar in oxic and anoxic growth media (Tobler, et al., 2023).

Further rheological analyses of the hydrogels did not show noticeable changes in the storage and loss moduli of the hydrogels before and after mineral precipitation. However, slipping the hydrogels during rheometry potentially limits the reliability of the outcomes.

Reference

D. Tobler *et al.*, “Comparison of rates of ureolysis between Sporosarcina pasteurii and indigenous groundwater community under conditions required to precipitates large volumes of calcite,” *Geochim Cosmochim Acta*, vol. 75, no. 11, pp. 3290–3301, 2011, Accessed: Nov. 26, 2023. [Online]. Available: https://doi.org/10.1016/j.gca.2011.03.023

APPENDIX C

EFFECT OF SURFACE ROUGHENING ON THE ADHESIVE STRENGTH OF BIOMINERAL-BIOPOLYMER ADHESIVES

Surface roughening of the stainless-steel slides was carried using sandpapers with grit size120 to achieve a surface roughness (S_a) value of 1.3. The stainless-steel coupon was roughened by placing a 150g (1.5N normal force) on the glass slide. The sanding was carried out for 1 minute at 30s intervals. The slides were then cleaned by sonication in 100% ethanol for 1 minute to remove all sanding residue.

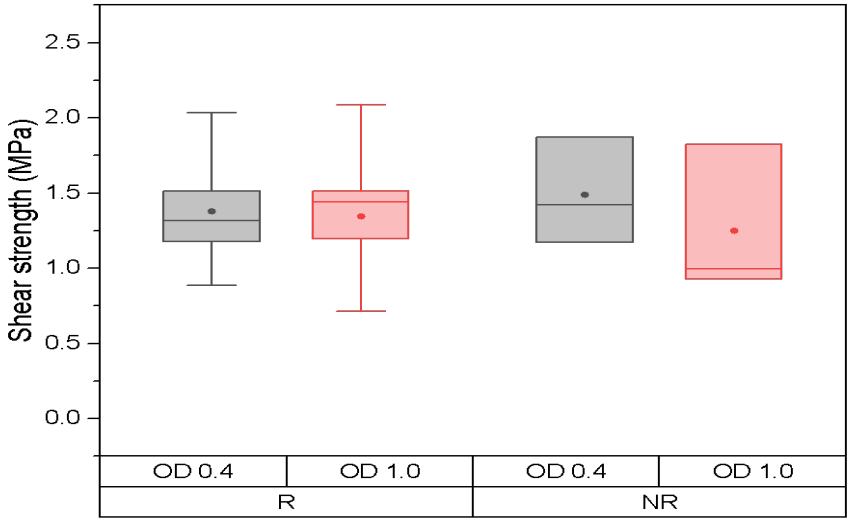

Figure C 1: Adhesive shear strength of soy protein-based microbially induced calcium carbonate (MICP) reinforced adhesives on stainless steel lapjoints. The bacterial cell densities (OD) were 0.4±0.3 and 1.0±0.3, and surface treatments were (R) roughened and (NR) untreated stainless-steel surfaces. The upper and lower bounds of the boxplot represent the 25th and 75th percentiles, and the whiskers indicate minimum and maximum values. The median is indicated by a horizontal straight line. There was no difference between the adhesive strengths observed with roughened and untreated stainless-steel surfaces for either low or high OD MICP-reinforced adhesives ($p>0.05$).

APPENDIX D

THE INFLUENCE OF SOY PROTIEN ISOLATE AND GUAR GUM ON UREOLYSIS BY *SPOROSARCINA PASTEURII*

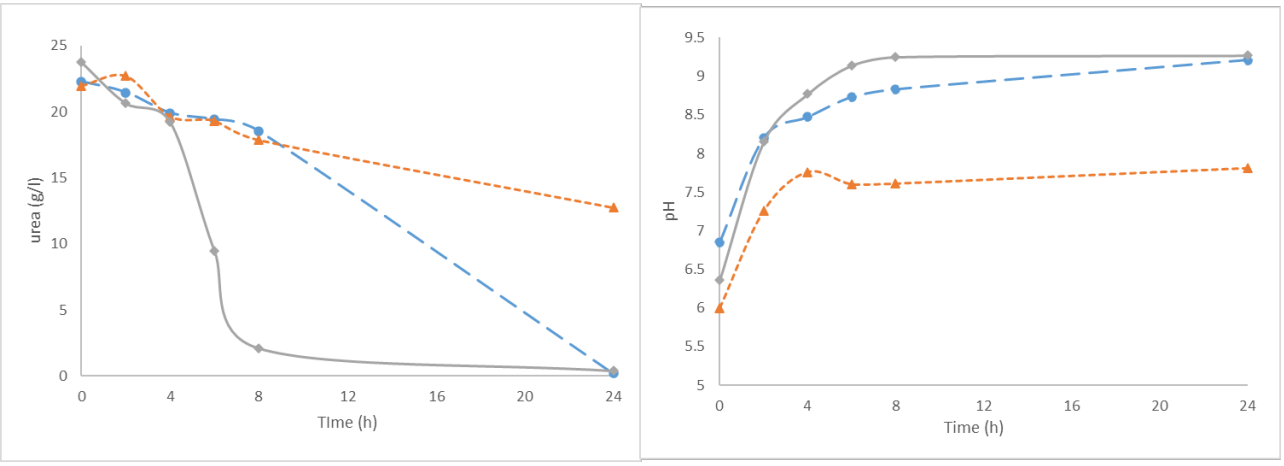

Figure D 1: (Left) Ureolysis by *Sporosarcina pasteurii* in the presence of (♦) urea at 0.33M concentration, (●) soy protein isolate and urea, (▲) soy protein isolate, urea and calcium at 1:1 M ratios, and (right) corresponding pH changes in the growth media during ureolysis.

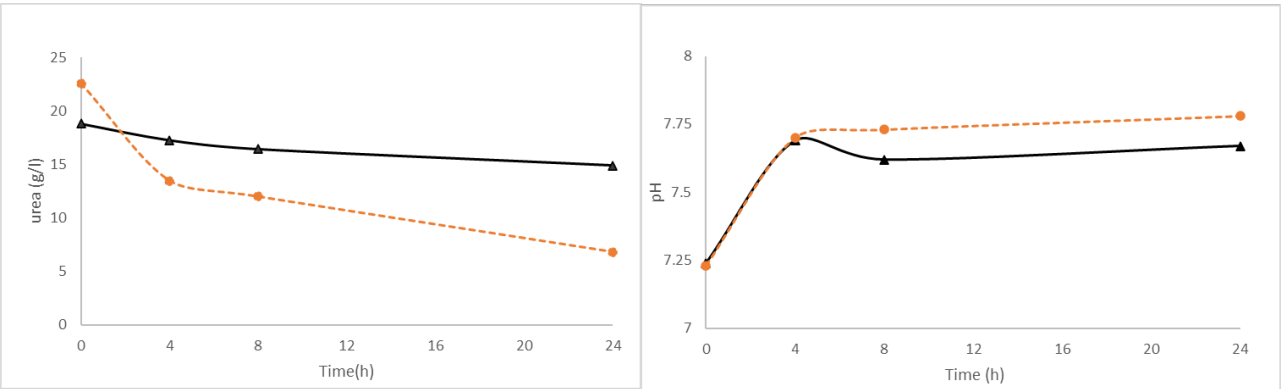

Figure D 2: (Left) Ureolysis in the presence of presence of (▲) urea and calcium at 0.33M concentrations (●) guar gum, urea and calcium, and (right) corresponding pH changes in growth media during ureolysis.

It was noted that the rates of ureolysis are influenced by the biopolymer type. Differences in ureolysis rates did not significantly influence the pH in the presence of calcium ions. Further analysis, such as quantitative TGA, can determine the effect of biopolymer type on the mineral content produced under altered ureolysis kinetics.